NAVAL POSTGRADUATE SCHOOL

MONTEREY, CALIFORNIA

THESIS

POLARIMETRIC THERMAL IMAGING

by

Fook Leong Loo

March 2007

Thesis Advisor:	Alfred W. Cooper
Second Reader:	Gamani Karunasiri

Approved for public release; distribution is unlimited

THIS PAGE INTENTIONALLY LEFT BLANK

REPORT DOCUMENTATION PAGE		*Form Approved OMB No. 0704-0188*
Public reporting burden for this collection of information is estimated to average 1 hour per response, including the time for reviewing instruction, searching existing data sources, gathering and maintaining the data needed, and completing and reviewing the collection of information. Send comments regarding this burden estimate or any other aspect of this collection of information, including suggestions for reducing this burden, to Washington headquarters Services, Directorate for Information Operations and Reports, 1215 Jefferson Davis Highway, Suite 1204, Arlington, VA 22202-4302, and to the Office of Management and Budget, Paperwork Reduction Project (0704-0188) Washington DC 20503.		
1. AGENCY USE ONLY *(Leave blank)*	**2. REPORT DATE** March 2007	**3. REPORT TYPE AND DATES COVERED** Master's Thesis
4. TITLE AND SUBTITLE: Polarimetric Thermal Imaging		**5. FUNDING NUMBERS**
6. AUTHOR(S) Fook Leong, Loo		
7. PERFORMING ORGANIZATION NAME(S) AND ADDRESS(ES) Naval Postgraduate School Monterey, CA 93943-5000		**8. PERFORMING ORGANIZATION REPORT NUMBER**
9. SPONSORING /MONITORING AGENCY NAME(S) AND ADDRESS(ES) N/A		**10. SPONSORING/MONITORING AGENCY REPORT NUMBER**
11. SUPPLEMENTARY NOTES The views expressed in this thesis are those of the author and do not reflect the official policy or position of the Department of Defense or the U.S. Government.		
12a. DISTRIBUTION / AVAILABILITY STATEMENT Approved for public release; distribution is unlimited		**12b. DISTRIBUTION CODE** A

13. ABSTRACT (maximum 200 words)

Passive infrared (IR) imagers, using intensity contrast for target detection, are often limited by low target-background contrast. Detecting stationary targets against cluttered backgrounds presents an even bigger challenge. Polarized signatures can be used as an additional discriminator, to improve target detection probability and reduce false alarm rate. In this research, a polarimetric thermal imager, operating in the mid wave infrared (3-5 μm), was set up using the Merlin InSb camera with three internal wire grid polarizers. Non uniformity correction and radiometric calibration were performed to compensate for differences in detector response and polarizer's transmittance. The scene consisted of a heated aluminum plate in front of a large area blackbody as background. The viewing angle, defined as the angle between surface normal and camera line of sight, was varied by rotating the plate about its vertical axis. Stokes parameters were computed from the irradiance images. Images of intensity, degree of polarization and polarization angle were derived from the Stokes parameters. The dependence of these polarization characteristics on viewing angle was investigated. While intensity increased slightly with viewing angle, degree of polarization increased rapidly when the viewing angle was increased from 20° to 80°. The polarization angle increased with viewing angle and became constant at 150° for viewing angle greater than 60°. Target to background contrast based on degree of polarization increased with viewing angle and was higher than intensity contrast for viewing angle greater than 20°. Image processing algorithms were developed to segment the target plate from its background. The target similarity metric used was the texture-based Fisher distance, which enabled the fusion of one or more data type. The performance of the fusion schemes was compared via their Receiver Operating Characteristic (ROC) curves, which were plots of segmentation accuracy against false alarm rate. Binary image of the target was obtained by applying a Constant False Alarm Rate (CFAR) threshold. Fusion of intensity and polarization data produced better segmentation accuracy and lower false alarm rate than intensity-only data, for plate at viewing angle greater than 60°.

14. SUBJECT TERMS Passive infrared, polarized signatures, target detection probability, false alarms rate, wire grid polarizer, Stokes parameters, degree of polarization, polarization angle, Fisher distance, Receiver Operating Characteristic, Constant False Alarm Rate		**15. NUMBER OF PAGES** 121
		16. PRICE CODE
17. SECURITY CLASSIFICATION OF REPORT Unclassified	**18. SECURITY CLASSIFICATION OF THIS PAGE** Unclassified	**19. SECURITY CLASSIFICATION OF ABSTRACT** Unclassified	**20. LIMITATION OF ABSTRACT** UL

NSN 7540-01-280-5500

Standard Form 298 (Rev. 2-89)
Prescribed by ANSI Std. 239-18

THIS PAGE INTENTIONALLY LEFT BLANK

POLARIMETRIC THERMAL IMAGING

Fook Leong Loo
Civilian, DSO National Laboratories, Singapore
B.Eng., National University of Singapore, 1995
M.Eng., National University of Singapore, 1997

Submitted in partial fulfillment of the
requirements for the degree of

**MASTER OF SCIENCE IN ELECTRONIC WARFARE SYSTEMS
ENGINEERING**

from the

**NAVAL POSTGRADUATE SCHOOL
March 2007**

Author: Fook Leong Loo

Approved by: Alfred W. Cooper
                     Thesis Advisor

                     Gamani Karunasiri
                     Second Reader

                     Dan C. Boger
                     Chairman, Department of Information Sciences

THIS PAGE INTENTIONALLY LEFT BLANK

ABSTRACT

Passive infrared (IR) imagers, using intensity contrast for target detection, are often limited by low target-background contrast. Detecting stationary targets against cluttered backgrounds presents an even bigger challenge. Polarized signatures can be used as an additional discriminator, to improve target detection probability and reduce false alarm rate. In this research, a polarimetric thermal imager, operating in the mid wave infrared (3-5 μm), was set up using the Merlin InSb camera with three internal wire grid polarizers. Non uniformity correction and radiometric calibration were performed to compensate for differences in detector response and polarizer's transmittance. The scene consisted of a heated aluminum plate in front of a large area blackbody as background. The viewing angle, defined as the angle between surface normal and camera line of sight, was varied by rotating the plate about its vertical axis. Stokes parameters were computed from the irradiance images. Images of intensity, degree of polarization and polarization angle were derived from the Stokes parameters. The dependence of these polarization characteristics on viewing angle was investigated. While intensity increased slightly with viewing angle, degree of polarization increased rapidly when the viewing angle was increased from 20° to 80°. The polarization angle increased with viewing angle and became constant at 150° for viewing angle greater than 60°. Target to background contrast based on degree of polarization increased with viewing angle and was higher than intensity contrast for viewing angle greater than 20°. Image processing algorithms were developed to segment the target plate from its background. The target similarity metric used was the texture-based Fisher distance, which enabled the fusion of one or more data type. The performance of the fusion schemes was compared via their Receiver Operating Characteristic (ROC) curves, which were plots of segmentation accuracy against false alarm rate. Binary image of the target was obtained by applying a Constant False Alarm Rate (CFAR) threshold. Fusion of intensity and polarization data produced better segmentation accuracy and lower false alarm rate than intensity-only data, for plate at viewing angle greater than 60°.

THIS PAGE INTENTIONALLY LEFT BLANK

TABLE OF CONTENTS

LIST OF FIGURES

x

THIS PAGE INTENTIONALLY LEFT BLANK

LIST OF TABLES

THIS PAGE INTENTIONALLY LEFT BLANK

ACKNOWLEDGMENTS

THIS PAGE INTENTIONALLY LEFT BLANK

I.   INTRODUCTION

Passive infrared (IR) imagers are widely used in the military for target detection and recognition. Most of these IR imagers use intensity contrast for target discrimination. Target detection is often limited by low target-background contrast and relies on target motion for cuing. Detection of a stationary target against cluttered background is especially challenging. To overcome these limitations, additional discriminators, such as polarization signatures, can be used to improve detection probability and reduce false alarms.

The objective of this research is to study the characteristics of polarized thermal emission and their potential applications in target detection and recognition. A polarimetric thermal imager, operating in the mid wave infrared (3-5 μm), was set up using the Merlin InSb camera with three internal wire grid polarizers. Non uniformity correction and radiometric calibration were performed to compensate for differences in detector response and polarizer's transmittance. Stokes parameters [11] were computed from the irradiance images. Images of intensity, degree of polarization and polarization angle were derived from the Stokes parameters. The dependence of these polarization characteristics on viewing angle was investigated. Statistical mean and variances of the signatures were computed.

Image processing algorithms were developed to segment the target plate from its background. The target similarity metric used was the texture-based Fisher distance [20]. The metrics allowed fusion of one or more polarization parameter: intensity, degree of polarization and polarization angle. The performance of the fusion schemes was compared via their Receiver Operating Characteristic (ROC) curves, which were plots of segmentation accuracy against false alarm rate. Binary image of the target was obtained by applying a Constant False Alarm Rate (CFAR) threshold to the data.

The camera was fixed in position and the target scene consisted of a heated aluminum plate in front of a large area blackbody as background. The plate's surface was positioned vertically with its normal along the plane of emission, i.e., horizontal plane. The viewing angle was defined as the angle between the surface normal and the camera

1

line of sight. The plate was rotated to vary the viewing angle. Emission from the target aluminum plate was found to be partially polarized for viewing angle greater than 20°. The horizontal component was higher than the vertical component and the 135° component was higher than the 45° component. The higher horizontal component can be attributed to absorption of the vertical component by the metal. When the viewing angle of the target plate was increased from 0 to 80°, the intensity increased slightly due to higher emissivity of the aluminum plate at wide emission angles. The degree of polarization (DOP) was less than 1% at 20° viewing angle. DOP increased rapidly from 1% to 8.5%, when the viewing angle was increased from 20° to 80°. The angle of polarization (AOP) increased with viewing angle, and became constant at 150° for viewing angle greater than 60°.

Target and background contrast was calculated as the ratio of the difference and sum of their signal intensities. The contrast based on intensity increased slightly from 5 to 10% with viewing angle. The contrast based on DOP increased with viewing angle from 0% at 20° to a maximum value of 90% at 70°. The higher target-background contrast provided by DOP at angle greater than 20° can potentially improve the probability of detection and reduce false alarms in the target detection process.

The intensity-only data produced good segmentation of the plate at 0° to 40° viewing angle. Fusion of intensity, degree of polarization and polarization angle produced better segmentation accuracy and lower false alarm for viewing angle greater than 60°. This was because both the degree of polarization and polarization angle data, produced better results than intensity-only data. At a constant false alarm rate of 20%, the enhancement in segmentation accuracy over the intensity-only data, improved from 3% to 41%, when the viewing angle was increased from 60° to 80°.

The polarized radiations from a scene comprise both reflected and emitted components. For infrared wavelengths, where cold sky is the main contributor to the reflective component, surface emission tends to dominate the signature and the state of polarization. However, the reflected components may be important in some cases. Thus, the combined effect of reflection and emission on polarized signature was proposed as a follow up study.

Chapter II provides a survey of the physics of infrared radiations and polarization phenomena, the quantification and measurement of polarized signatures, target detection using states of polarization as discriminator, and image segmentation algorithms. Chapter III describes the experimental setup, detector non-uniformity correction, radiometric calibration and data collection procedures. Chapter IV presents the analysis and results of polarized signatures and their dependence on viewing angles. Chapter V describes the image segmentation algorithms, the performance of data fusion, and the segmentation results.

THIS PAGE INTENTIONALLY LEFT BLANK

II.   REVIEWS OF POLARIMETRIC THERMAL IMAGING

This chapter reviews the theories of infrared radiation and polarization, the methods used in the quantification and measurements of polarized radiation, applications of infrared polarimetric imaging and image processing techniques.

A.   PHYSICS OF INFRARED RADIATION AND POLARIZATION

1.   Physics of Thermal Radiation

An object with temperature above absolute zero contains atoms and molecules in excited states. Energy is stored in these electronic, vibrational and rotational states. When these atoms and molecules return to their lower energy states, some of the energy is released in the form of photons, which have frequencies related to the energy difference between the energy states,

$$\Delta E = h \nu \qquad\qquad (2.1)$$

where, ΔE = energy difference between states

h = Planck's constant

ν = frequency of emitted radiation

Vibrational and rotational state transitions result in emission or absorption of photons having wavelengths in the infrared region. Thus, infrared emission in the 3-5 μm (MWIR) and 8-12 μm (LWIR) atmospheric windows can be attributed to the superposition of vibrational and rotational change in states.

2.   Laws of Thermal Radiation

A blackbody is an ideal emitter and absorber, with both absorptivity (α) and emissivity (ε) equal to unity. Its spectral radiant exitance is the maximum for any thermal

source at a particular temperature. Many sources in the real world have spectral characteristics close to those of a blackbody. [1]

The spectral radiant exitance of a blackbody as a function of temperature and wavelength is given by Planck's Radiation Law:

$$M_{bb}(\lambda,T) = \frac{c_1}{\lambda^5(e^{c_2/\lambda T}-1)} \quad (\text{W/cm}^2\text{-}\mu\text{m}) \qquad (2.2)$$

where, c_1= first radiation constant $(3.7415 \times 10^4 \text{ W}\mu\text{m}^4/\text{cm}^2)$

c_2= second radiation constant $(1.4388 \times 10^4 \text{ }\mu\text{K})$

T= absolute temperature (K)

λ = wavelength (m)

The spectral radiant exitance is related to the spectral radiance as follows:

$$M_{bb}(\lambda,T) = L_{bb}(\lambda,T)\Omega \qquad (2.3)$$

where Ω = solid angle subtended by detector at the emitter.

The radiant exitance is obtained by integrating the spectral radiant exitance over the waveband of interest. For the 3-5 μm band, the radiant excitance is given by:

$$M_{bb}(T) = \int_3^5 \frac{c_1}{\lambda^5(e^{c_2/\lambda T}-1)}d\lambda \qquad (2.4)$$

The spectral radiant exitance of a non-blackbody is defined as:

$$M(\lambda,T) = \varepsilon(\lambda,T)M_{bb}(\lambda,T) \qquad (2.5)$$

6

where $\varepsilon(\lambda,T)$ is the spectral emissivity, with a value less than unity. A gray body is a material, whose emissivity is independent of wavelength over the waveband of interest.

The wavelength where the maximum radiation occurs for a given body temperature becomes shorter with increasing temperature. The wavelength corresponding to the peak emission is obtained by differentiating the Planck equation and solving for the maximum. The peak wavelength is given by Wien Displacement Law:

$$\lambda_{max} = \frac{2898}{T} \ (\mu m) \tag{2.6}$$

where, T is the body temperature in Kelvin.

Total radiant exitance is obtained by integrating the Planck equation over the entire spectrum. The result is given by the Stefan-Boltzmann Law:

$$W_{bb} = \sigma T^4 \ (W/cm^2) \tag{2.7}$$

where, σ = Stefan Boltzmann constant (5.669×10^{-12} W/cm^2-K)

T= temperature (K)

For a non-blackbody, the total radiant exitance is modified as:

$$W = \varepsilon \sigma T^4 \ (W/cm^2) \tag{2.8}$$

where ε is the effective emissivity of the non-blackbody source.

3. Polarization Characteristics

Infrared radiation propagates through an isotropic medium in the form of Transverse Electromagnetic (TEM) waves, which contain orthogonal electric and

magnetic fields in a plane that is perpendicular to the direction of propagation. The time varying electric field vector, E(z,t), can be resolved into 2 orthogonal components:

$$E_x(z,t) = E_{ox}(t)\cos(kz - \omega t + \delta_x(t))$$
$$E_y(z,t) = E_{oy}(t)\cos(kz - \omega t + \delta_y(t)) \tag{2.9}$$

where, E_{ox} and E_{oy} are the electric field amplitudes and δ_x and δ_y are the phases of the electric field components. The locus traced out by the tip of the resultant electric field vector as it varies with time, is described by the Lissajous figure equation:

$$(\frac{E_x}{E_{ox}})^2 + (\frac{E_y}{E_{oy}})^2 - (\frac{2E_xE_y}{E_{ox}E_{oy}})\cos\delta = \sin^2\delta \tag{2.10}$$

where, $\delta = \delta_x - \delta_y$ is the phase difference between the two electric field components. Figure 2.1 shows the polarization ellipse traced out by the tips of the resultant electric field vector [2].
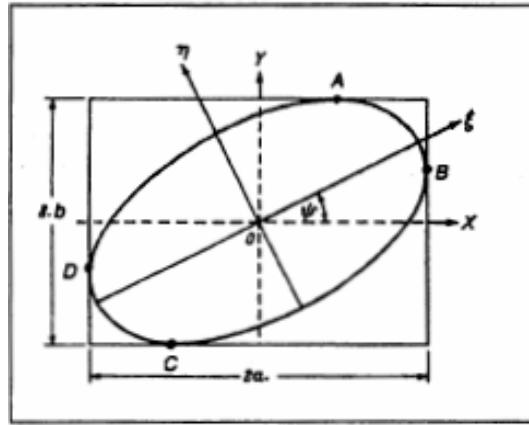
Figure 2.1:   Polarization ellipse described by a time varying electric field (From [2])

The angle of polarization ψ, is the angle between the ellipse's major axis and the horizontal. It is related to the electric field components by the following expression:

8

$$\tan 2\psi = \frac{2E_{ox}E_{oy}\cos\delta}{E_{ox}^{2} + E_{oy}^{2}}, \text{ where } 0 < \psi < \pi \qquad (2.11)$$

The ellipticity angle χ is given by the ratio of the minor and major axis lengths:

$$\tan\chi = \frac{\pm b}{a}, where -\frac{\pi}{2} < \chi < \frac{\pi}{2} \qquad (2.12)$$

In terms of the electric field components, the ellipticity angle can be expressed as:

$$\sin 2\chi = \frac{2E_{ox}E_{oy}\sin\delta}{E_{ox}^{2} + E_{oy}^{2}} \qquad (2.13)$$

Degenerate forms of the ellipse include the linear and circular polarization. Linear polarization occurs when the phase difference δ is 0° or 180°. Substituting $\delta=0^{\circ}$ into Equation (2.10) yields the locus of the time varying electric field as a straight line:

$$\frac{E_x}{E_{ox}} = \frac{E_y}{E_{oy}} \qquad (2.14)$$

Figure 2.2 shows the Lissajous figure for linearly polarized light. Similar substitution into Equation (2.11) shows that the angle of polarization ψ for linearly polarized light is the slope of the straight line:

$$\tan\psi = \frac{E_{oy}}{E_{ox}} \qquad (2.15)$$

The slope is positive if the phase difference δ is 0° and is negative if δ is 180°. For linearly polarized light, the ellipticity angle χ is zero.

9
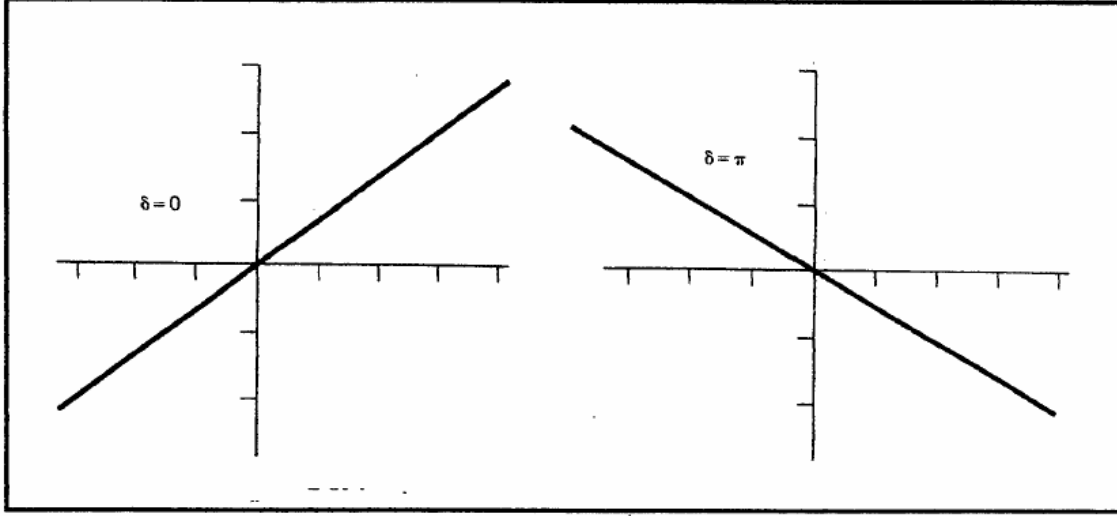
Figure 2.2:   Lissajous figure for linearly polarized light (From [3])

Circular polarization occurs when the phase difference δ is $\pm 90^{\circ}$ and the amplitudes of the electric field components are the same. Substituting $\delta = \pm 90^{\circ}$ and $E_{ox} = E_{oy} = E_o$ into Equation (2.10) yields the equation of a circle with radius E_o.

$$(\frac{E_x}{E_o})^2 - (\frac{E_y}{E_o})^2 = 1 \qquad (2\text{-}16)$$

Figure 2.3 shows the Lissajous figure for circularly polarized light. For $\delta = +90^{\circ}$, the resultant field vector rotates clockwise and the light is described as left-circularly polarized. If $\delta = -90^{\circ}$, the resultant field vector rotates counter-clockwise and the light is right-circularly polarized. The angle of polarization ψ is zero and the ellipticity angle χ is 45°.
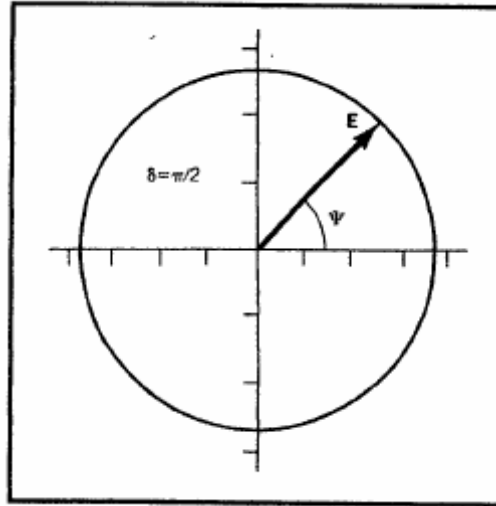
Figure 2.3:   Lissajous figure for circularly polarized light (From [3])

B.   POLARIZATION OF REFLECTED AND EMITTED RADIATION

The energy collected by a thermal camera from a scene comprises both reflected and emitted radiation. Both components are usually partially polarized. For infrared wavelengths, where cold sky is the main contributor to the reflective component, surface emission tends to dominate the signature and the state of polarization. Thus, polarization of emitted radiation is of greater (but not exclusive) interest to remote sensing.

1.   Reflection Polarization

Radiation incident on an air-metal interface is either reflected or transmitted into the material. Figure 2.4 shows the electric field components oriented parallel and perpendicular to the plane of incidence (horizontal x-y plane), for the incident (E_i), reflected (E_r) and transmitted (E_t) radiation. The sensor line of sight is parallel to the plane of incidence. The reflected radiation is partially polarized with greater electric field components oriented perpendicular to the incidence plane, i.e., vertically polarized.
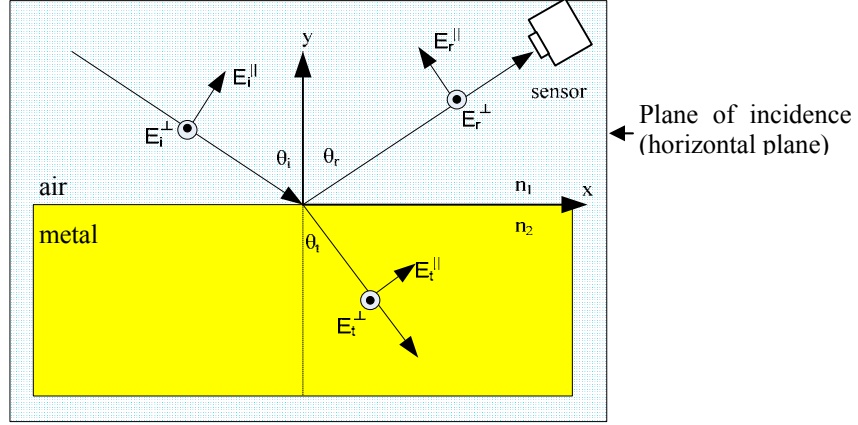
Figure 2.4: Reflection and transmission of light incident at oblique angle on an air-metal interface (Top view)

The reflectivity for parallel ($R_{\parallel}$) and perpendicular ($R\perp$) polarized radiations are given by the Fresnel equations [4]. From the sensor viewpoint shown in Figure 2.4, the parallel and perpendicular components correspond to horizontal and vertical polarizations, respectively.

$$R_{\parallel} =\mid \frac{E_r^{\parallel}}{E_i^{\parallel}}\mid^2=\mid \frac{n_2\cos\theta_i - n_1\cos\theta_t}{n_2\cos\theta_i + n_1\cos\theta_t}\mid^2 \qquad (2.17)$$

$$R_{\perp} =\mid \frac{E_r^{\perp}}{E_i^{\perp}}\mid^2=\mid \frac{n_1\cos\theta_i - n_2\cos\theta_t}{n_1\cos\theta_i + n_2\cos\theta_t}\mid^2 \qquad (2.18)$$

where n_1 = refractive index for air (n_1=1)

n_2 = complex refractive index for metal

θ_i = incident angle

θ_t = transmitted angle

Refraction of radiation at the interface also obeys Snell's law:

$$n_1\sin\theta_i = n_2\sin\theta_t \qquad (2.19)$$

12

The degree of reflection polarization DOP$_r$ is defined as:

$$DOP_r(\theta_r) = \left| \frac{R_{\parallel}(\theta_r) - R_{\perp}(\theta_r)}{R_{\parallel}(\theta_r) + R_{\perp}(\theta_r)} \right| \qquad (2.20)$$

The reflectivity and degree of polarization at an air-aluminum interface are plotted as a function of viewing or reflected angles in Figure 2.5. The complex refractive index for the aluminum plate was selected to be n_2=4.45-3.3i. The imaginary part was set lower than that of an ideal aluminum metal (4.45-31.5i @ 3 μm [5]), to account for surface roughness and oxidation state of the real aluminum plate.
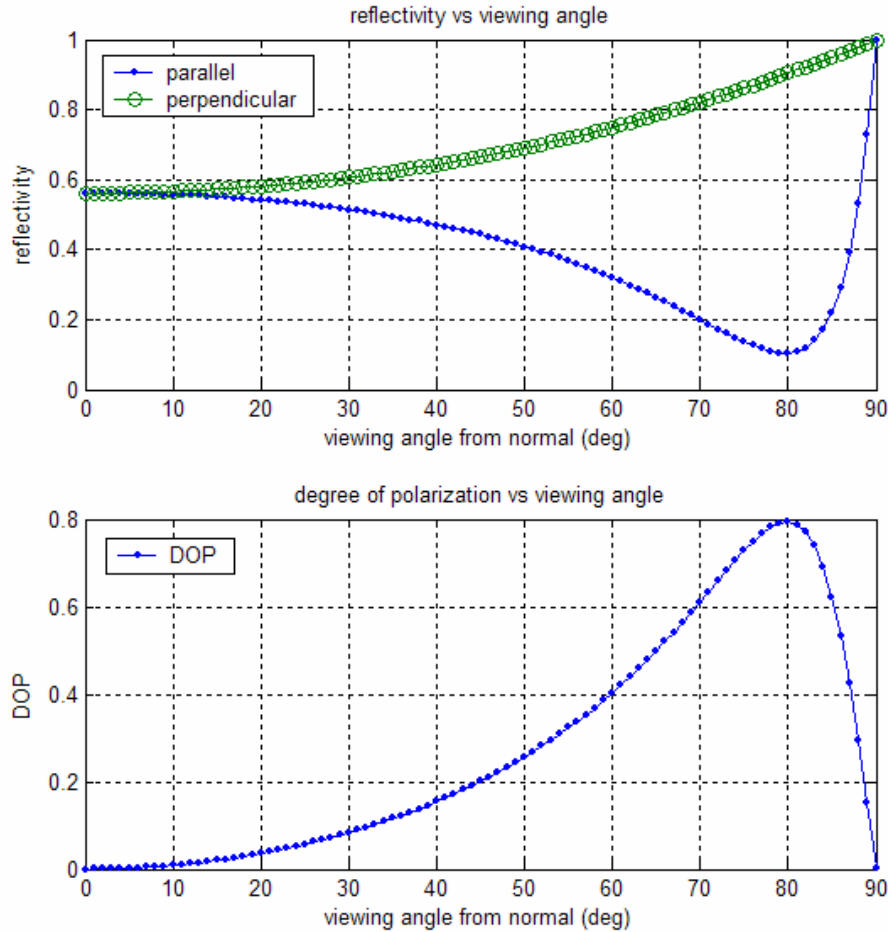
Figure 2.5:   Plots of reflectivity and degree of polarization as a function of viewing angles for an air-aluminum interface with n_2=4.45-3.3i

The reflectivity at normal viewing angle is about 60%. At oblique angles, the perpendicularly polarized component is higher than the parallel component. The parallel component has a minimum, but non-zero value, at around 80° (principal angle of incidence). Degree of polarization reaches a peak value of 80% at the principle angle. In contrast, for an air-dielectric interface, the reflectivity of the parallel component ($R_{\parallel}$) is zero at Brewster angle and the reflected radiation is 100% perpendicularly polarized.

2.   Emission Polarization

Polarization of emitted radiation from an incandescent body was first observed in 1824 by Arago [6]. In 1895, Millikan's qualitative experiments showed that a high degree of polarization was obtained with metals [7]. The highest degree of polarization was obtained from smooth surfaces and at large oblique angle from the normal. Non-metallic, transparent and opaque objects gave weak polarization. The explanation for the observed polarization involved refraction of radiation emitted from within the object at the interface. The theories and qualitative work on emission polarization were summarized in Sandus's paper [8].

According to Kirchoff's law, emissivity is proportional to absorptivity, $\alpha(\lambda)$, which is related to reflectivity, $R(\lambda)$, as:

$$\alpha(\lambda) = 1 - R(\lambda) \tag{2.21}$$

Thermal radiations emitted (E_t) from an air-metal interface (Figure 2.6) is also partially polarized, with stronger electric field components oriented parallel to the plane of emission (horizontal x-y plane), i.e., horizontally polarized. The sensor line of sight is parallel to the plane of emission.
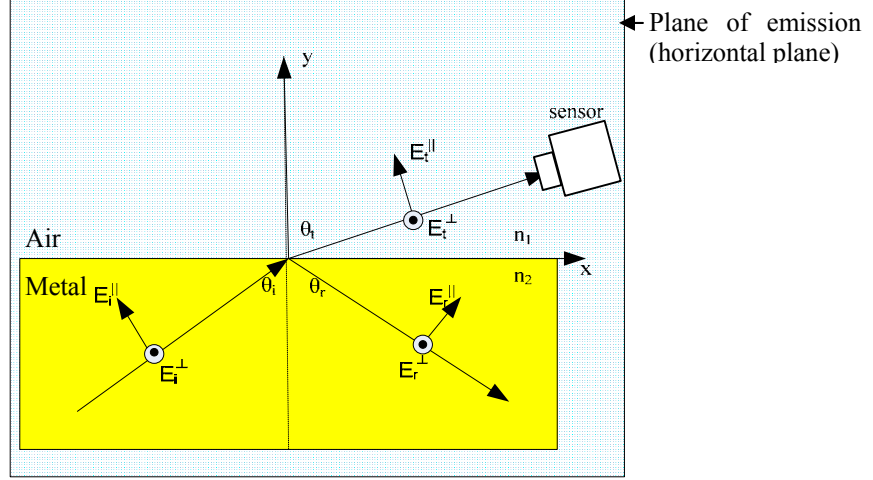
Figure 2.6:   Emission and reflection of light incident at oblique angle from within a
metal at the air-metal interface (Top view)

Applying Kirchoff's law and the Fresnel equations, the emissivities for radiation polarized parallel ($\varepsilon_\parallel$) and perpendicular ($\varepsilon\perp$) to the plane of emission are given by [9]. From the sensor viewpoint shown in Figure 2.6, the parallel and perpendicular components correspond to horizontal and vertical polarizations, respectively.

$$\varepsilon_\parallel = |\frac{E_t^\parallel}{E_i^\parallel}|^2 = \frac{4n_2\cos\theta_t}{\cos^2\theta_t + 2n_2\cos\theta_t + n_2^{\,2} + \kappa_2^{\,2}} \tag{2.22}$$

$$\varepsilon_\perp = |\frac{E_t^\perp}{E_i^\perp}|^2 = \frac{4n_2\cos\theta_t}{(n_2^{\,2} + \kappa_2^{\,2})\cos^2\theta_t + 2n_2\cos\theta_t + 1} \tag{2.23}$$

where, $n_c = n_2 - i\kappa_2$ is the complex refraction index of the metal

θ_t = emission angle or viewing angle

The total emissivity is the mean value of the parallel and perpendicular components.

$$\varepsilon = \frac{1}{2}(\varepsilon_\parallel + \varepsilon_\perp) \tag{2.24}$$

15

The degree of emission polarization (DOP$_e$) is defined as:

$$DOP_e(\theta_t) = \left| \frac{\varepsilon_\parallel(\theta_t) - \varepsilon_\perp(\theta_t)}{\varepsilon_\parallel(\theta_t) + \varepsilon_\perp(\theta_t)} \right| \qquad (2.25)$$

For the air-aluminum interface, the normalized emissivity ($\varepsilon(\theta_t)/\varepsilon(0)$) and degree of polarization are plotted in Figure 2.7 as a function of viewing angles (θ_t). For emitted radiations, the parallel polarized component is higher than the perpendicular component. The parallel component increases with viewing angle up to a maximum value at around 80° and then decreases at higher angles. The perpendicular component decreases monotonically with angle. The total emissivity increases slightly with viewing angle up to a maximum value at around 80° and then decreases at large angle. The degree of polarization increases with viewing angle up to a maximum value of about 90% at 90°. As in the reflectivity plot in Figure 2.5, the complex refractive index for the aluminum plate was selected to be $n_2=4.45-3.3i$, to account for surface roughness and oxidation states.

In contrast, for an air-dielectric interface, both the parallel and perpendicular polarized components decrease with viewing angle. The total emissivity decreases with angle roughly as a cosine function (Lambertian). The degree of polarization of the emitted radiation also increases with angle, but is at a much lower value compared to that of emission from metal.

16
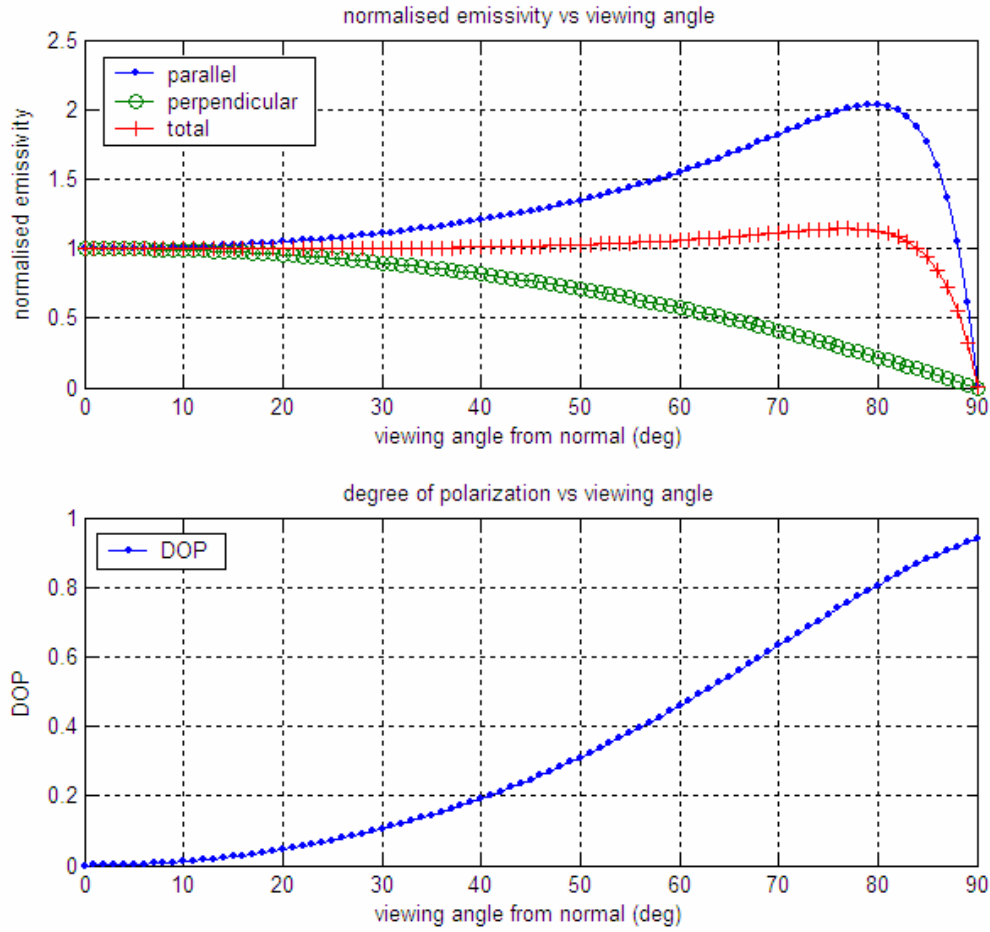
Figure 2.7:   Plots of emissivity components and degree of polarization as a function of viewing angles for an air-aluminum interface with n_2=4.45-3.3i

Wolff et. al. [10] has presented simulated and empirical results of degree of polarization for aluminum and dielectric plate polished to different roughness. Figure 2.8a) shows the degree of polarization, at different viewing angle, for an aluminum plate polished to roughness of 7 μm, 10 μm and 40 μm (peak-to-peak), respectively. The aluminum plate degree of polarization increases with viewing angle and decreases with surface roughness. Figure 2.8b) shows the degree of polarization, at different viewing angle, for a glass plate roughened to 10 μm, 20 μm and 40 μm (peak-to-peak), respectively. The glass plate degree of polarization also increases with viewing angle and decreases with surface roughness, but is lower than that of the aluminum plate.
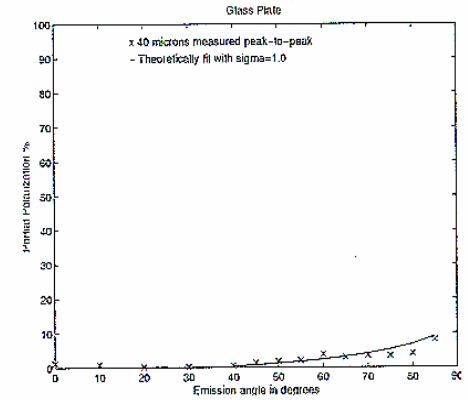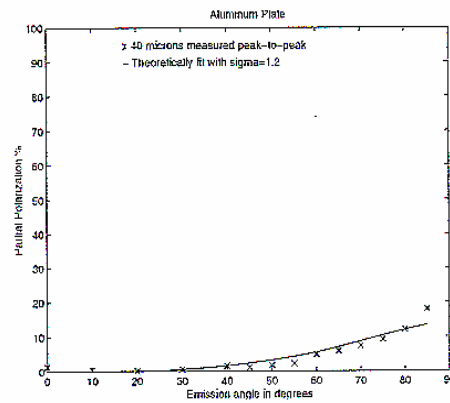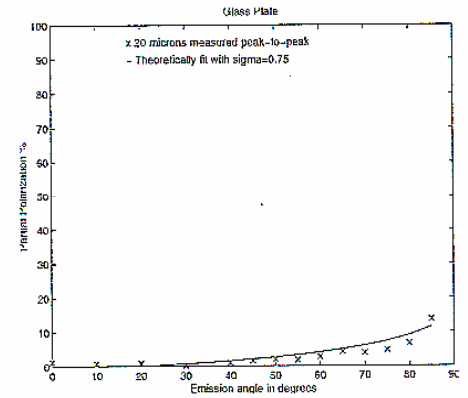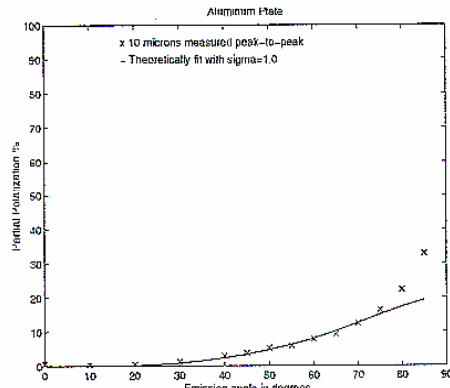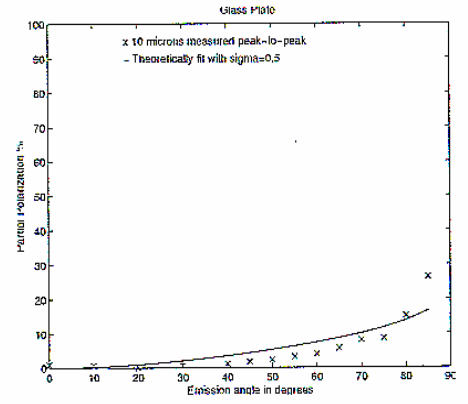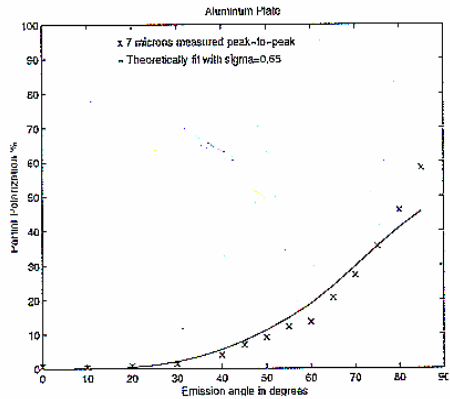
Figure 2.8: Plots of degree of polarization as a function of viewing angles for a) aluminum plate and b) glass plate polished to different roughness (From [10])

C.   QUANTIFICATION AND MEASUREMENT OF POLARIZATION

The polarization states of reflected or emitted infrared radiations can be described by the Stokes parameters $\{S_0, S_1, S_2, S_3\}$ [11]. The Stokes parameters are related to the mean squared values of the electric field amplitudes through the following equations:

$$S_0 = <E_{ox}^2> + <E_{oy}^2>$$

$$S_1 = <E_{ox}^2> - <E_{oy}^2>$$

$$S_2 = <2E_{ox}E_{oy}\cos\delta>$$

$$S_3 = <2E_{ox}E_{oy}\sin\delta> \tag{2.26}$$

where $\delta = \delta_x - \delta_y$ is the phase difference between the two orthogonal electric fields. The first parameter S_0 is a measure of the total intensity of radiation. The second parameter S_1 measures the intensity of linear polarization in the horizontal direction relative to that in the vertical direction. The third parameter S_2 measures the intensity of linear polarization in a plane rotated 45° to the horizontal relative to that in the 135° plane. The fourth parameter S_3 is associated with circular polarization. S_3 cannot be imaged by a linear polarizer and will not be of interest in this work. Radiation emitted from a heated object is partially polarized, so its total intensity is less than the sum of the polarized components.

$$S_0^2 \leq S_1^2 + S_2^2 + S_3^2 \tag{2.27}$$

The first three Stokes parameters can be determined from intensity of radiation polarized in the planes at 0°, 90° and 45° to the horizontal.

$$S_0 = I_0 + I_{90} \tag{2.28a}$$

$$S_1 = I_0 - I_{90} \tag{2.28b}$$

19

$$S_2 = 2I_{45} - I_0 - I_{90} \qquad\qquad (2.28c)$$

For polarimetric thermal imaging [11], the Stokes parameters are calculated for every pixel in the image. Images of intensity (I), degree of polarization (DOP) and angle of polarization (ψ) are obtained from the Stokes parameters using the following relations:

$$I = S_0 \qquad\qquad (2.29)$$

$$DOP = \frac{\sqrt{S_1^2 + S_2^2}}{S_0} \qquad\qquad (2.30)$$

$$\psi = \frac{1}{2}\tan^{-1}\left(\frac{S_2}{S_1}\right) \qquad\qquad (2.31)$$

Howe, J. D. [12] provides a review of different full Stokes imaging polarization cameras. These cameras operate either in the time sequential mode or simultaneous sensing mode. For sequential imaging, a rotating filter wheel containing a set of linear wire grid polarizers with transmission axes aligned at 0°, 90° and 45° to the camera's horizontal plane may be used. For this setup, the polarizers should ideally have the same transmission and extinction ratio. In practice, the differences between the polarizers would have to be calibrated in the same manner as in non-uniformity correction of focal plane arrays. Care has to be taken in the installation of the polarizer to minimize the Narcissus effect. Thermal emission generated inside the optical housing and reflecting off the wire grid polarizer may induce spurious signals that can easily mask the polarization components. Another design uses a rotating quarter wave plate and a fixed linear polarizer. This design eliminates problems associated with transmittance differences in the polarizers. The anti-reflection coated elements will not induce strong Narcissus effects as in the rotating polarizer design.

For simultaneous sensing, camera architectures can make use of division of amplitude or division of aperture. A division of amplitude camera uses polarizing beam splitters to separate orthogonal polarization components and direct them to different parts of a detector array. Since two images have to share the same detector array, the sensor

field of view is smaller and resolution is lower than for a radiometric camera using the whole array. Spatial registration is also a concern, since imperfection in the beam splitter and other optics can spatially distort the two images. In the division of aperture camera, the aperture can be subdivided in the optical train, or at the focal plane using a separate analyzer for each detector. The latter design was adopted by Chun et. al. [13], where repeating patterns of wire grids were deposited on a substrate placed on top of the detector. The pattern consists of four different orientations of a wire grid, with each covering one pixel. The optics has to be de-focused so that the blur spot covers all the four grids. This alleviates the registration problem, but results in lower sensitivity and resolution.

D. TARGET DETECTION APPLICATIONS

Polarization is one of the four physical quantities associated with optical fields, the other three being intensity, wavelength and coherence. Polarimetry measures the vector nature of the optical fields across a scene and provides valuable information on the object's surface orientation, shapes and roughness. Polarimetric signatures of man-made objects are distinct from those of natural background and are also largely uncorrelated with intensity and spectral information. Thus, polarimetric imaging is useful in enhancing target signal and suppressing background clutter.

Rogne et. al. [14] summarized the empirical and field test results of their work in using infrared polarized images for target detection. Figure 2.9 shows the measured polarized signature of different paint samples in the LWIR, 7.5-12 μm band, viewed at 45° from the normal, with clear sky specular reflection. The sample temperature was 270K. The samples ranged from very rough sand-paint mixtures to smooth but low gloss coatings. The reference plates are viewed at normal incidence and ideally should have no polarized signature component. Their polarization levels illustrate the degree of calibration and noise induced error in the measurement. The solid line shows the theoretical degree of polarization expected from an ideal surface. The average degree of

polarization measured was around 3%, which is about 30% of the theoretical values. A few samples registered polarization close to the theoretical value.
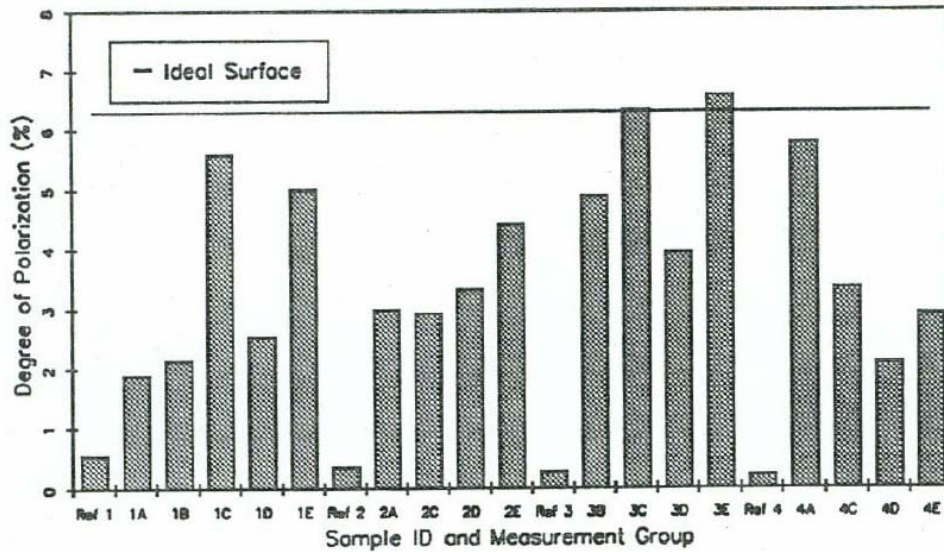
Figure 2.9: Measured polarized signature components in the 7.5-12 μm band for selected paint samples viewed at 45° from normal. (From [14])

The measurements showed that polarized signature was present in many targets and target materials. The magnitude of the signature depends on the surface properties, such as roughness, cleanliness and coating. Polarized signature of surfaces viewed at 60° from normal produces typical equivalent apparent temperature difference in the range of 2-6 K. Cloud cover was a dominant weather factor in polarimetric imaging. Low cloud is associated with reduced polarized signature. Background features consisting of grass, trees and clouds showed little or no polarized signature. An exception is a sea surface viewed at grazing angle. Cooper et. al. [15] has reported that in sun glint regions, infrared radiations reflected from sea surfaces are predominantly horizontally polarized. Outside the sun glint region, vertically polarized radiations dominate, which can be attributed to emission from the sea.

Later work by Rogne, et. al. [16] included target and background polarized data collected using a MWIR (4.6-4.9 μm) InSb focal plane camera and Brewster's angle beamsplitter. They concluded that polarimetric sensing could significantly enhance the detection of a target with low radiometric contrast against rural background clutter. Rural

clutter exhibited low mean degree of polarization below 0.2%. The vertical and horizontal polarized images for rural clutter were highly correlated, often exceeding 99% and thus could provide good clutter suppression. Water surfaces were found to be partially polarized with 1-3% mean degree of polarization and are potential sources of false alarms. Ground based measurements indicated that there is little or no polarization for sky and cloud clutter.

Emissive polarization can potentially be used for automatic target recognition and discrimination against decoy materials. The degree of polarization provides information on surface roughness, plane orientation and material types. Wolff et. al. [10] have shown that the degree of polarization of the MWIR emission from aluminum and dielectric plates decreases with surface roughness. Also, higher degree of polarization in thermal emission is indicative of metal, while a dielectric tends to emit radiation with lower partial polarization.

Spectrally varying polarization signatures of some materials exhibit unique features that could be used to distinguish between them. Matthew et. al. [17] measured the Stokes parameters (S_1, S_2 and S_3) of polarized images of 3 different materials: aluminum painted with black Krylon paint, rusted steel plate and smooth glass plate. Measurements were made at an angle of 56° from the surface normal using a LWIR polarimeter operating in the spectral band spanning 8-12 μm. The S_1 signature showed unique spectral features (Figure 2.10) while there was no significant polarization in the S_2 and S_3 signatures of all three materials.
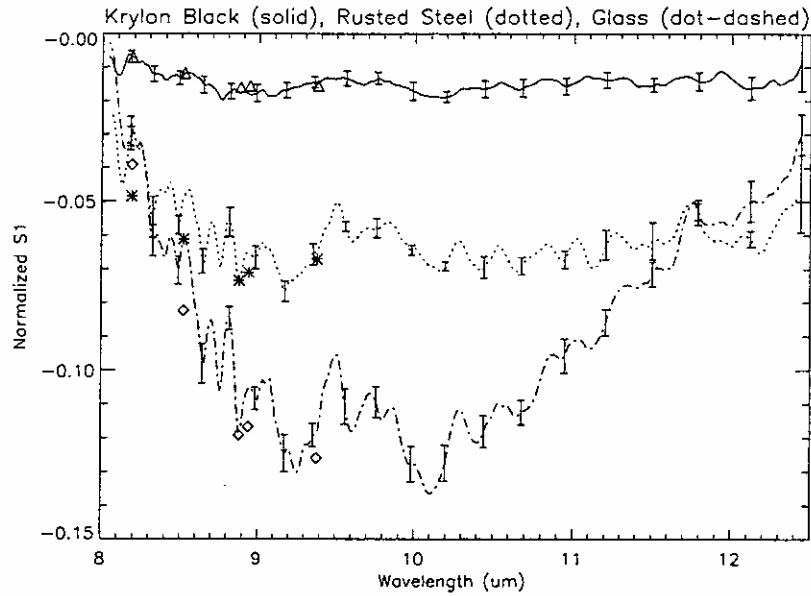
Figure 2.10:   Measured spectral varying polarized signature, S_1 in the 8-12 μm band for a) aluminum plate painted with Krylon paint, b) rusted steel plate and c) smooth glass plate. (From [17])

Howe et. al. [18] used a passive MWIR polarimetric camera as part of a multi-sensor suite for enhancing the detection of surface mines. In addition to thermal contrast, the Stokes images provide additional information on surface properties which were used in the detection and classification algorithms to improve detection performance. Diurnal variation in the polarized infrared (MWIR) signature of metal and plastic mines against cluttered background was measured. The irradiance contrasts for both metallic and plastic mines are shown in Figure 2.11. The irradiance contrast varies with time of the day, being positive in the day and becoming negative at night.

24
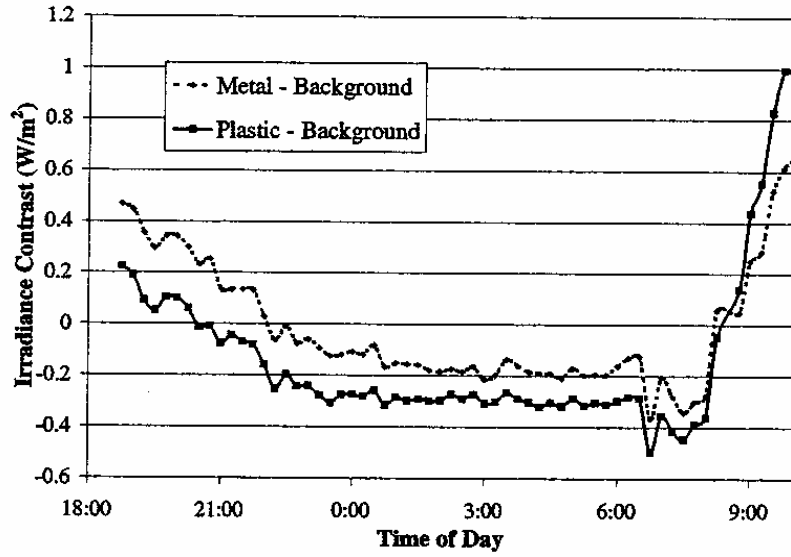
Figure 2.11:   Thermal intensity contrast of mine and background.(From [18])

In comparison, the degree of polarization contrast remained positive throughout the diurnal cycle (Figure 2.12). The mine objects also exhibited higher degree of polarization and hence can be distinguished from the background and clutter objects. Metal mines also produced higher degree of polarization than plastic mines.
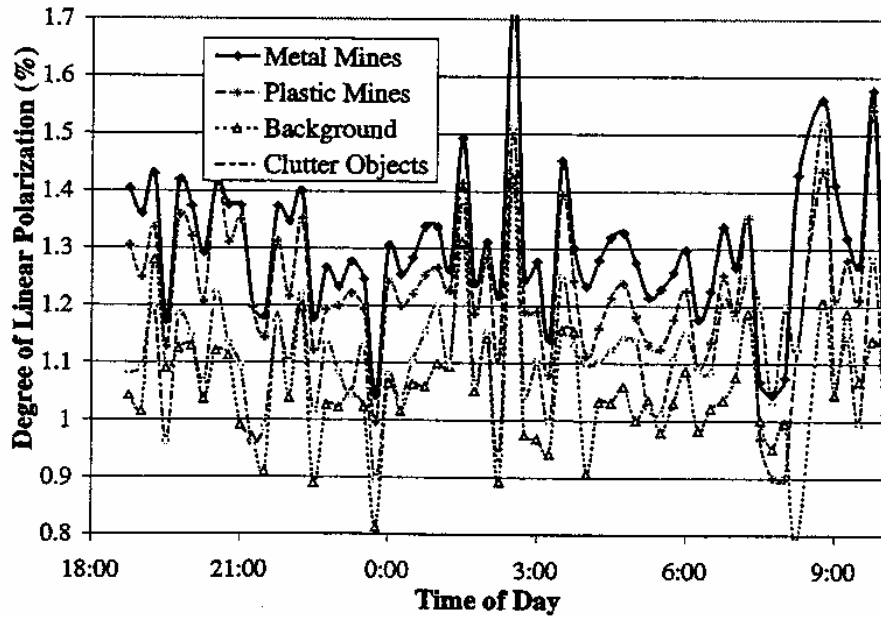
Figure 2.12:   Degree of linear polarization for metal and plastic mines, clutter objects and background. (From [18])

25

Polarimetric imaging systems have also been tested for automatic detection of non-cooperative small targets, occupying a few pixels among a cluttered background [19]. The Stoke parameters of the target scenes were measured and transformed into the target's polarization states of intensity, degree of polarization and angle of polarization. These polarization states were fused using statistical techniques to derive the probability measure for detection. Synthetic polarized infrared images were used to evaluate the performance of the detection algorithms in terms of their Receiver Operating Characteristic (ROC) curves. The results indicated good detection probability and low false alarm for target size as small as four pixels. The algorithm performance was shown to improve when the sensor to target range increased from 1 to 12 km.

E.   IMAGE PROCESSING TECHNIQUES

In the paper by Sadjadi and Chun [20], a target detection module was proposed for polarimetric thermal images. The module extracts both edges and regions of interest using texture based techniques. The data input were the set of three registered images corresponding to the scene's infrared intensity (I), degree of polarization (P) and angle of polarization (ψ).

The schematic of the texture based region segmentation algorithm is shown in Figure 2.13. The inputs to this module include the three intensity, degree of polarization and angle of polarization images, window size, threshold value and the statistical means (μ) and variances (σ^2) of the target of interest. The window size is approximated by the target size. The target statistics can be obtained offline from a model archive.
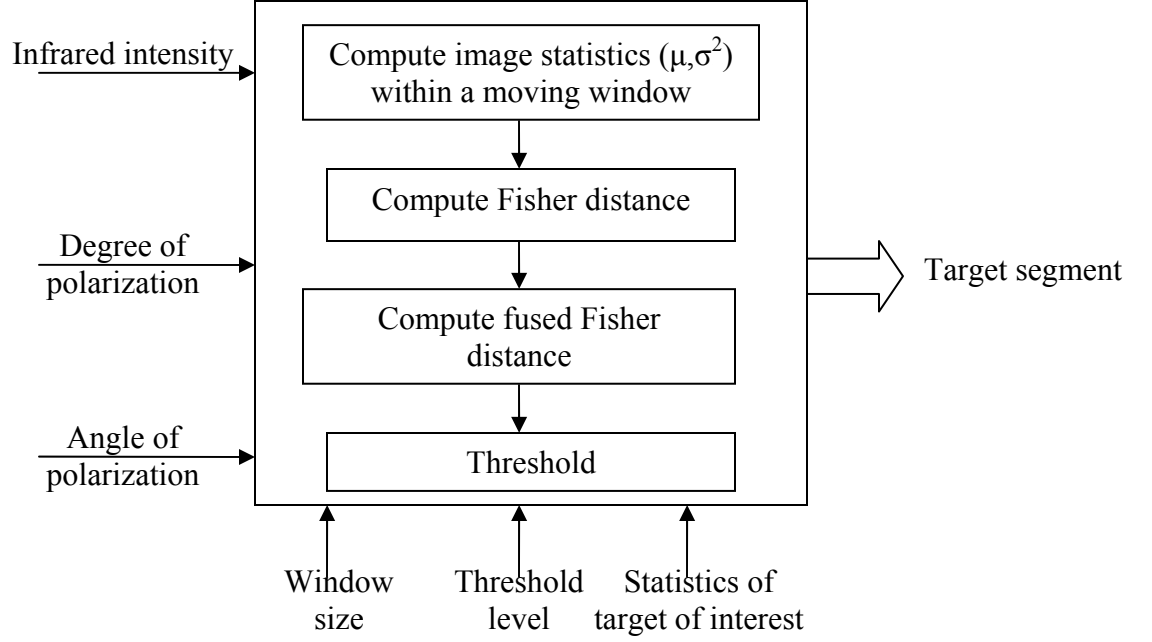
Figure 2.13:   Polarization-sensitive statistical segmentation (From [20])

First, the mean (μ) and variance (σ^2) of the image within the moving window are computed. Next, a measure of statistical similarity between the input image data and target of interest is computed. The measure used is the Fisher distance (F).

$$F = n_I \frac{(\mu_{I,m} - \mu_{I,r})^2}{(\sigma^2_{I,m} + \sigma^2_{I,r})} + n_P \frac{(\mu_{P,m} - \mu_{P,r})^2}{(\sigma^2_{P,m} + \sigma^2_{P,r})} + n_\Phi \frac{(\mu_{\psi,m} - \mu_{\psi,r})^2}{(\sigma^2_{\psi,m} + \sigma^2_{\psi,r})} \qquad (2.32)$$

where, n_i = weights for the data type i

$\mu_{i,m}$ = measured mean value

$\sigma^2_{i,m}$ = measured variance

$\mu_{i,r}$ = mean value for the reference target

$\sigma^2_{i,r}$ = variance for the reference target

i = data type I: intensity, P: degree of polarization and ψ: polarization angle

Regions that are statistically similar to that of the target of interest will generate a low F value. Thus, by applying an appropriate threshold, the region of interest can be

27

segmented from the background. The criteria can also be adjusted to enable classification of regions into different classes of interest.

The performance metric for the segmentation algorithm is the Receiver Operating Characteristic (ROC) curve, a plot of segmentation accuracy (SA) versus False Alarms Rate (FAR). SA is defined as the ratio of overlap between the reference target (G) area and the segmented area (T), and the union of G and T.

$$SA = \frac{T \cap G}{T \cup G} \qquad (2.33)$$

The FAR is defined as the ratio of the area outside the overlap of the reference target (G) area and the segmented area (T), and the area of the reference target area.

$$FAR = \frac{\overline{(T \cap G)}}{G} \qquad (2.34)$$

The data points on the ROC curves were obtained by plotting the SA and FAR, resulting from segmentation using increasing threshold values of the Fisher distance. The paper showed that segmentation using fused intensity, degree of polarization and polarization angle, resulted in improved segmentation accuracy of between 20-50% when compared to using intensity-only data.

III.   EXPERIMENTAL SETUP AND PROCEDURES

This chapter describes the experimental setup for measuring the polarized emission signature of a heated plate in the laboratory. The characteristics of the Merlin InSb camera and wire grid polarizers are reviewed. Radiometric and polarimetric calibration procedures are explained. Data collection procedures are outlined.

A.   EXPERIMENTAL SETUP

1.   Bench Top Setup

The setup in the laboratory is shown in Figure 3.1. The Merlin camera and target plate were set up at opposite ends of the work bench. The distance between them was such that the blackbody fills the entire field of view (FOV) of the camera. The target plate was positioned in front of the blackbody and centered in the camera FOV. During measurement, the entire setup was covered with a black curtain to shield off external heat sources and prevent reflected radiation from entering the camera's aperture.
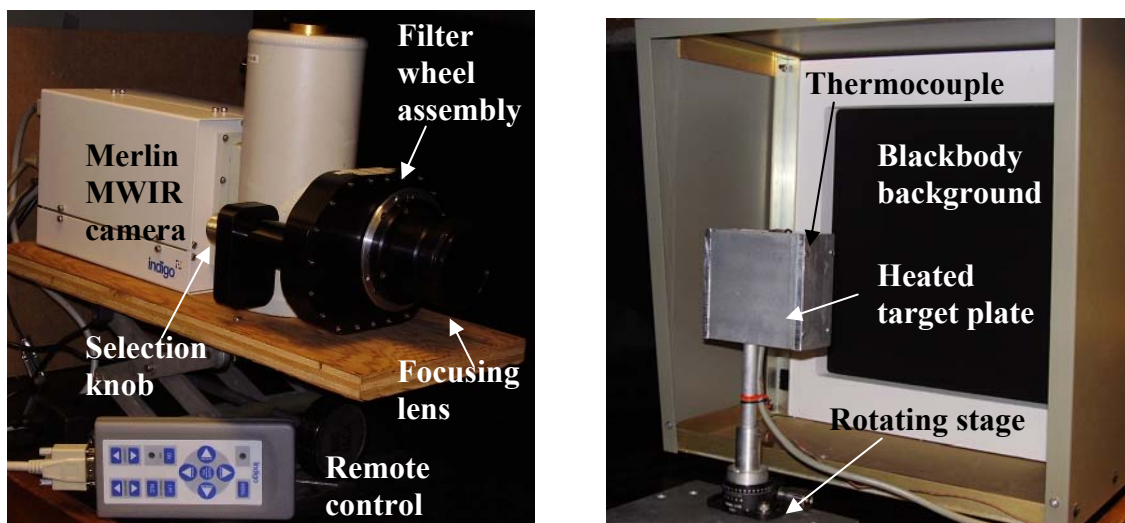
Figure 3.1:   Experimental setup for measuring polarized emission signature

The camera was mounted on a jack and its height adjusted to align the camera's line of sight to the plate. The camera has an internal filter wheel with 4 positions. Positions 1 to 3 were occupied by polarizers, with transmission axes orientated at 0°, 45° and 90° to the camera's horizontal plane, and position 4 was empty. A 3-5 μm band-pass filter was applied to all the 4 channels. Placing the polarizer between the focusing lens and the detector plane in the camera was a better configuration compared to using an external polarizer. An external polarizer introduces the narcissus effect, which has to be compensated by tilting the polarizer at a large angle.

The target plate has a heating element attached to its back and thermal paste was applied on the interfaces to improve thermal conductivity. The heating element was shielded from the camera view with 2 side plates and a rear plate. The heating current was controlled with a variable A.C. power supply to provide a temperature range from 20-70°C. A thermocouple attached to the top of the plate measured the temperature of the plate. The plate is mounted on a micro-rotating stage. At 0° aspect angle, the target plate's surface was normal to the camera line of sight. The stage was turned about the vertical axis to change the plate's aspect angle from 0 to 80° (with respect to camera line of sight). The blackbody was positioned with its surface normal to the camera line of sight. The blackbody surface provided a uniform background for the image scene. The blackbody temperature was adjusted to obtain different target-to-background thermal contrast.

2. Merlin MWIR Camera

The Merlin MWIR camera consists of a 320x256, InSb detector Focal Plane Array (FPA), which is cooled with liquid nitrogen during operation [21]. The detector spectral response is from 1.5-5 μm. The camera filter wheel assembly has 4 positions for mounting internal filters or polarizers. In the experiment, the operating band was limited to 3-5 μm by a band-pass filter. Three polarizers were installed in the filter wheel with their transmission axes at 0°, 45° and 90° to the camera's horizontal plane and the last slot was left blank. The polarizers were switched in front of the detector by rotating an external knob, thus allowing sequential imaging of the same scene at different polarization axes. The camera lens provides a fixed FOV of about 15° and allows

focusing on objects at different distances. The NETD of the detector was specified to be better than 25 mK. Detailed specifications of the camera are included in Appendix A.

The Merlin camera was operated with the IRVISTA image acquisition and analysis software [21]. Figure 3.2 shows the graphical interface of IRVISTA. The software provides friendly interfaces for viewing, capturing and saving image frames and sequences. The image frames are exported as 12 bits tif file format, which are then imported into Matlab for analysis and processing. Image processing tools allow on-line analysis of live images. Some of the features used in the experiment are intensity line profile, 3-D intensity map, histogram display and statistical analysis. Non-uniformity corrections were performed using the software's two point and one point calibration features. The bad pixel replacement option replaces bad pixels with values obtained from bi-linear interpolation of adjacent pixels' intensity.
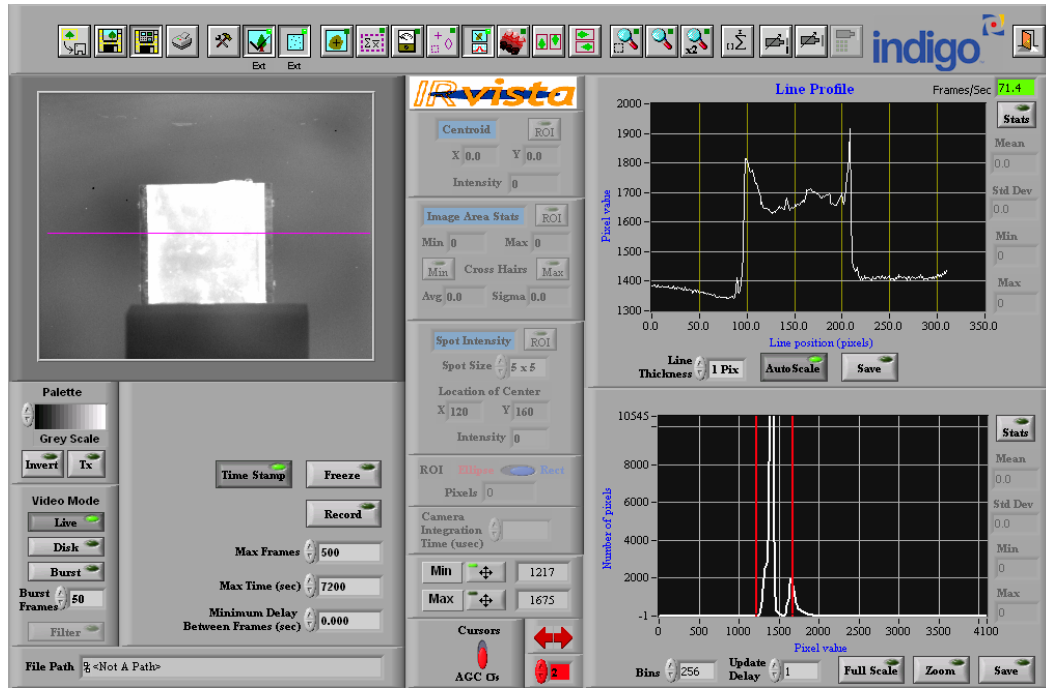
Figure 3.2:   IRVISTA Graphical User Interface

3.   Wire Grid Polarizer

The wire grid polarizer is made up of arrays of parallel aluminum coated lines deposited on a 25 mm diameter x 2 mm thick CaF_2 substrate. The grid period is 0.25μm.

The CaF$_2$ substrate is transparent in the spectral range from 1-10μm. Incident electric field vectors parallel to the grid lines are absorbed, while vectors perpendicular to the grid lines are transmitted. The spacing of the wire grids has to be shorter than the wavelength of the polarized light. Calculation of the polarizer parameters and the transmission plots provided by the supplier (SPECAC) are included in Appendix B. The important parameters of the polarizer are summarized in Table 3.1.

Parameters @ λ=5 μm	Specifications
Transmission efficiency, K1 (%)	90
Transmission of unwanted radiation, K2 (%)	0.4
Degree of polarization, (K1-K2)/(K1+K2) (%)	99.12
Extinction ratio, K1/K2	225

Table 3.1:   Specifications of wire grid polarizer

B.   CALIBRATION PROCEDURES

The Stokes parameters were calculated from the differences in the irradiance images, polarized along different axes. The difference being measured was often less than 10%. Thus, careful calibrations were needed to produce meaningful results. Radiometric calibrations included correction for non-uniformity of detectors' response, differences in polarizer's transmittance and narcissus effect. Polarimetric calibration involved quantifying the transmittance of the polarizer.

1.   Non-Uniformity Correction

The infrared camera's non uniformity refers to the differences in individual detector response to thermal or photon energy. These non uniformities have to be compensated by two-point and one-point non uniformity correction, which can be performed by the IRVISTA software [21]. Two-point correction involved measuring the output voltage of each detector when the camera was set up to look at two temperatures,

designated as cold and hot. The calibration process also accounted for non-uniformity introduced by other components in the camera setup, for example the effects of polarizer and lenses.

Prior to two-point correction, the camera was set up with the target plate in the center of the camera's FOV and the blackbody as the background. The IRVISTA software displayed the horizontal intensity profile across the middle of the image. The camera's integration time, video offset level and gain were adjusted to maximize the thermal contrast between the target and background. The cold and hot sources used were an extended blackbody at temperature $25^{o}C$ and $40^{o}C$, respectively. The temperatures coincided with the expected range of operating temperature. The blackbody source was placed close to the camera aperture, so that it filled the entire camera FOV with a uniform temperature source. The average detector response at the hot and cold temperatures was determined. The gain and offset values were calculated with respect to the average values and applied to each pixel so that its response fits the slope of the line connecting the cold and hot average points. The gain and offset coefficients were used to adjust the slope and DC level of each pixel's response as follows:

$$P_{ij}^{'} = G_{ij} * P_{ij} + O_{ij} \qquad (3.1)$$

where, $P_{ij}^{'}$ = corrected pixel's intensity

P_{ij} = uncorrected pixel's intensity

G_{ij} = gain coefficient

O_{ij} = offset coefficient.

During the two point correction process, pixels with gain values outside an acceptable range or whose intensities fluctuated too much during the frame averaging sequence were labeled as bad pixels. The 2-D gain and offset coefficients (NUC maps) and bad pixel maps derived for each camera setup were stored in memory and were selected and applied during measurement. The IRVISTA software computes the intensity

values using the gain and offset coefficients and replaces bad pixel intensities with values obtained from bi-linear interpolation of adjacent pixel intensities.

For a given camera setup, the same 2-D NUC and bad pixel maps were used over several months. One point correction was used to correct for drift in the detector response, which appeared as graininess in the image or black and white pixels. The one-point calibration involved measuring the detector response with the camera looking at a single temperature source. One point correction was performed before the start of each data collection sequence. A blackbody at temperature of 25°C was used. The offset coefficients in the NUC maps were updated to compensate for the drift in response.

2. Radiometric Calibration

Cremer et. al. [23] developed a two-point calibration procedure to convert the measured signals at the sensor from digital level to irradiance values (W/cm^2). The first step was to acquire digital images of a blackbody of temperature (T_l), at different polarization angles (ψ). The next step was to acquire the same image sequence of the blackbody of temperature (T_h). The irradiance on the sensors due to the blackbody radiation was computed by integrating Planck's law over the 3-5 μm spectral band. The calibrated irradiance, E(ψ,x,y), for pixel (x,y) and polarization angle (ψ) can be expressed as:

$$E(\psi, x, y) = E_{bb}(T_l) + \frac{[DL_{mea}(\psi, x, y) - DL_l(\psi, x, y)] * [E_{bb}(T_h) - E_{bb}(T_l)]}{DL_h(\psi, x, y) - DL_l(\psi, x, y)} \quad (3.2)$$

where, $E_{bb}(T_l)$ = irradiance due to blackbody at temperature T_l

$E_{bb}(T_h)$ = irradiance due to blackbody at temperature T_h

$DL_{mea}(\psi,x,y)$ = measured digital image of the target scene

$DL_l(\psi,x,y)$ = measured digital image of blackbody at temperature T_l

$DL_h(\psi,x,y)$ = measured digital image of blackbody at temperature T_h

For our measurements, T_l and T_h were set at 25°C and 40°C, respectively, to coincide with the apparent temperature range of the target scene. The measured signals

were linearly related to the irradiance in the temperature range. The calibration procedure reduced the effects of transmittance differences between the polarizers and spatial non-uniformity in the polarizer and detector response.

3. Polarizer Calibration

The important parameters of linear polarizers are their transmittance and extinction ratio. From the supplier's spectral transmittance data, transmission efficiency (K_1) and % transmission of unwanted radiation (K_2) in the 3-5 μm band were calculated using the following relations [1]:

$$K_1 = \frac{E_h + E_v}{E_0} \qquad (3.3)$$

$$K_2 = \frac{E_x}{E_h + E_v} \qquad (3.4)$$

where, E_v = optical power transmitted by the polarizer with its grid lines vertical

E_h = optical power transmitted by the polarizer with its grid lines horizontal

E_x = optical power transmitted by a pair of polarizers with grids crossed

E_0 = optical power received without polarizer.

The degree of polarization (DOP) and extinction ratio (μ) were computed as:

$$DOP = \frac{K_1 - K_2}{K_1 + K_2} \qquad (3.5)$$

$$\mu = \frac{K_1}{K_2} \qquad (3.6)$$

The polarizer parameters are tabulated in Table 3.1.

The transmission loss through the polarizer was obtained from the Signal Intensity Transfer Function (SITF) curves. Digital images of the blackbody at different temperatures were measured without polarizer and with polarizer at different

35

transmission angles (0, 45, 90 and 135°). The average digital values of the uniform scenes were computed and plotted against the blackbody temperatures. The transmission losses were calculated as a ratio of the intensity with polarizer and without polarizer.

C.   DATA COLLECTION PROCEDURES

The procedures were designed such that the polarized target scenes were recorded as close in time as possible to the calibration data. This is to reduce variation in the measured polarized signature, which may be caused by drift in detector response and fluctuation in ambient temperature.

1.   Setting Up procedure

a) Fill the dewar of the Merlin MWIR camera with liquid nitrogen and wait for the detector temperature to cool down to the temperature of the dewar.

b) Switch on the camera and load the NUC map that has been calibrated for the current camera parameters. Check for the correct integration time, video offset and gain.

c) Turn up the voltage output of the voltage regulator to heat the target plate to 50°C. The plate's temperature was monitored with a thermocouple attached to the top of the plate.

d) Turn on the blackbody's temperature controller to stabilize the blackbody's temperature at 25°C

e) Monitor the signal level of the blackbody. The signal should stabilize after about half an hour.

2.   Radiometric Calibration

a) Remove the target plate, leaving the 25°C blackbody to fill the entire FOV of the camera. Record 30 frames of the background.

b) Insert the polarizer in front of the camera with its transmission axis at 0° to the horizontal. Record 30 frames of the background.

36

c)   Repeat step b) with polarizer axis at 45° and 90° with respect to the horizontal.

d)   Raise the temperature of the blackbody to 30°C. Record 30 frames of the background without polarizer and with polarizer axis at 0°, 45° and 90°, respectively.

3.   High Contrast Image Collection

a)   Insert the 50°C target plate in the center of the camera's FOV with the 30°C blackbody as the background. The plate is oriented with its surface's normal aligned to the camera's line of sight (LOS).

b)   Record the image scene with polarizer axis at 0°, 45° and 90°, respectively.

c)   Rotate the target plate so that its surface normal is at 20° to the camera's LOS. Repeat data collection step b)

d)   Repeat step c) for different angles: 40°, 60°, 70° and 80°.

4.   Low Contrast Image Collection

a)   Raise the temperature of the blackbody to 35°C. Record 30 frames of the background without polarizer and with polarizer axis at 0°, 45° and 90°, respectively.

b)   Insert the 50°C target plate in the center of the camera's FOV and with the 35°C blackbody as the background. The plate is oriented with its surface's normal along the camera's LOS.

c)   Repeat steps 3b to 3d)

d)   Raise the temperature of the blackbody to 40°C. Record 30 frames of the background without polarizer and with polarizer axis at 0°, 45° and 90°, respectively.

THIS PAGE INTENTIONALLY LEFT BLANK

IV.   ANALYSIS OF POLARIMETRIC DATA

This chapter presents the results of processing and analyzing the raw polarized images. These include the signal-intensity transfer function, Stokes parameters, degree of polarization and angle of polarization. The images were analyzed to determine polarization characteristics as a function of viewing angle of the target plate. Statistical parameters such as the mean and variance of the target and background regions were computed.

A.   SIGNAL INTENSITY TRANSFER FUNCTION

The Signal Intensity Transfer Function (SITF) is a plot of the received signal digital level (ranges from $0\text{-}2^{12}$) against the equivalent blackbody irradiance (in W/cm^2). The digital levels were obtained by averaging pixel values over several frames of the blackbody image at a given temperature. The 4 data points were obtained by setting the blackbody temperatures at 25°, 30°, 35° and $40^o C$, respectively. The corresponding blackbody irradiance was calculated by integrating Planck's equation over the detector's bandwidth (3-5 μm). Figure 4.1 shows the SITF plots for the 3 polarized channels and the un-polarized channel.

The digital levels were linearly related to the blackbody irradiance within the temperature range from $25^o C$ to $40^o C$. Straight lines were fitted to the data points using linear regression. Using these linear relationships, the calibration formula described in Equation (3.2), was used to convert digital levels to irradiance values for the captured images.

$$E(\psi, x, y) = E_{bb}(T_l) + \frac{[DL_{mea}(\psi, x, y) - DL_l(\psi, x, y)] * [E_{bb}(T_h) - E_{bb}(T_l)]}{DL_h(\psi, x, y) - DL_l(\psi, x, y)} \quad (3.2)$$
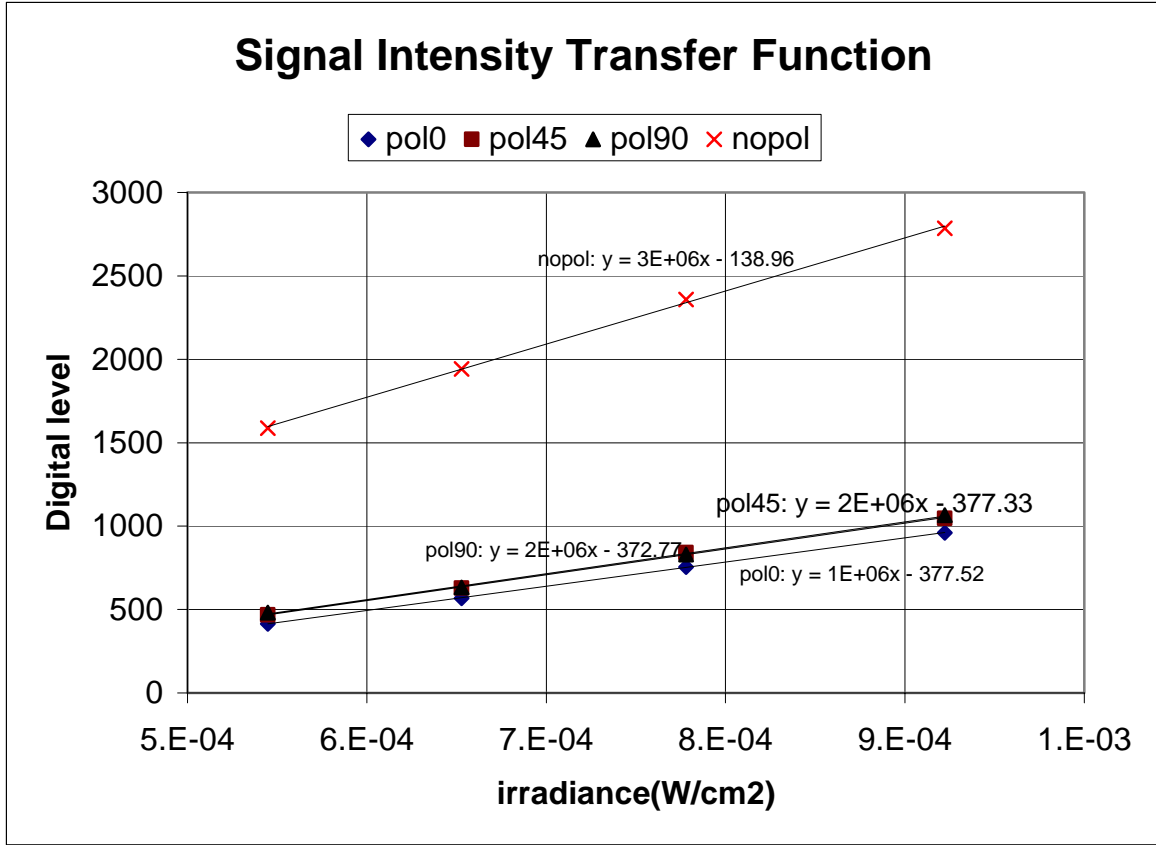
Figure 4.1:   Signal intensity transfer function

The transfer curves for polarizer oriented at 90° and 45° were similar. However, the horizontal polarizer has a lower transmittance. The transmittance difference was normalized using the calibration formula in Equation (3.2). The average transmittance of the polarizer was calculated as the ratio of the un-polarized and polarized signal levels. The transmittance of the polarizer at 90° and 45° was 34%, while that at 0° was 30%. The transmittance also improved slightly at higher irradiance level, which corresponds to a higher blackbody temperature. This is due to higher transmittance at shorter wavelengths in the 8-12 μm spectral bands (Appendix B, Figure B.1).

40

B.   POLARIZED EMISSION CHARACTERISTICS

The Stokes parameters were derived from the irradiance images captured with the polarizer oriented at 0°, 45° and 90° with respect to the camera's horizontal plane. Results for plate oriented at $\theta = 0^o$ and 70° viewing angles (θ: angle between surface normal and camera line of sight (LOS)) are presented below.

1.   Polarized Image Irradiance

The target plate was heated to a temperature of 50^oC, measured with the thermocouple mounted on the plate. The background was filled with a blackbody at 35^oC. Figure 4.2 a) shows the intensity image (256 grayscales) of the target plate oriented at 0°. The plate surface was not smooth and contained scratches and pits and traces of oxidation had formed over parts of the plate. The surface temperature was not uniform as evident from the different shades of grayscale and presence of "hot" spots over roughened areas. The "cold" vertical strips on the 2 sides were due to the side plates, which were not heated. "Hot" vertical strips developed next to the "cold" strips as a result of heat accumulation at the interface due to poor thermal conductivity.

a)   b)
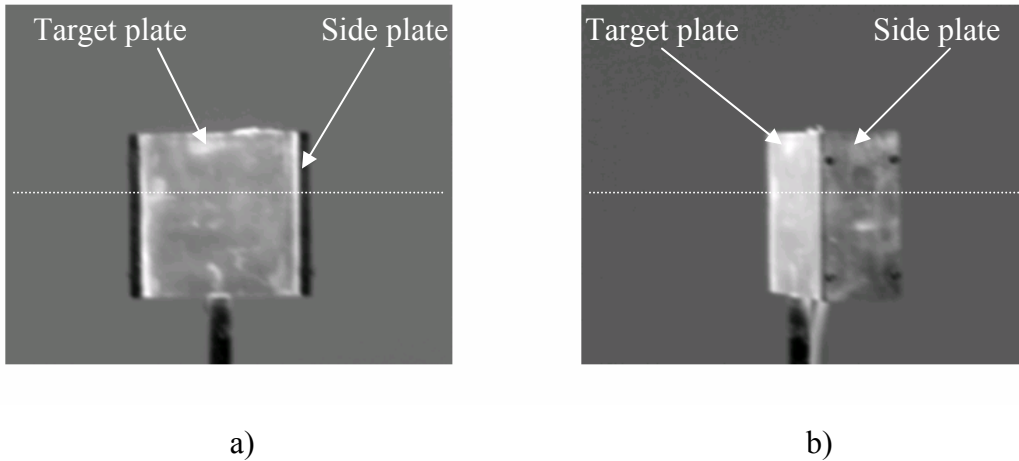
Figure 4.2:   Intensity image of target plate at a) 0° and b) 70° viewing angle

Figure 4.2 b) shows the same target plate oriented at 70°. The side plate was at 20° to the camera's LOS. Its surface temperature is lower than the front plate, but slightly higher than the background. Surface temperature distribution was not uniform.

41
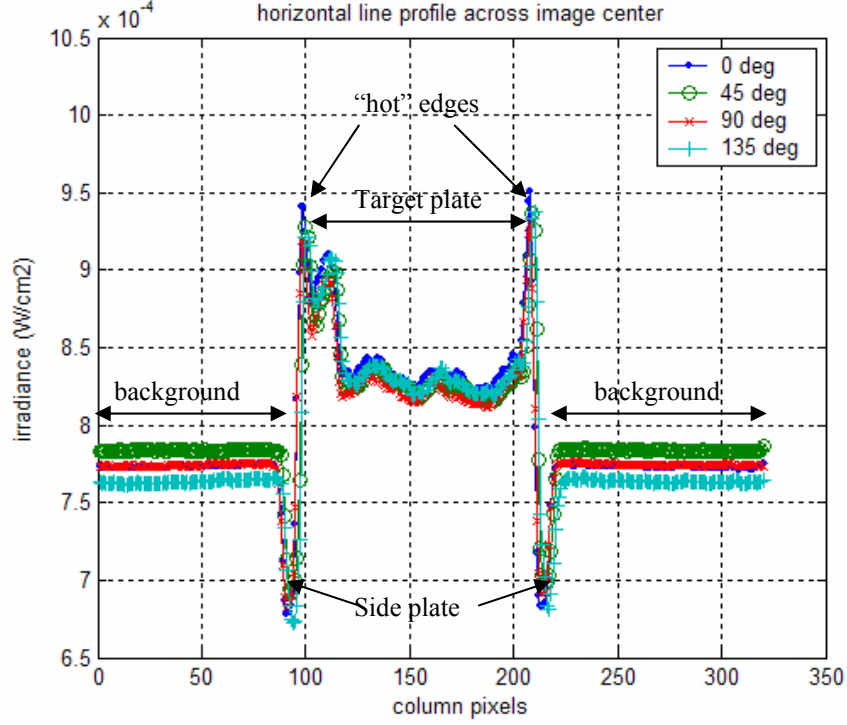
Figure 4.3:   Irradiance profile along a horizontal line across the center of the polarized images with target plate at 0° viewing angle

Figure 4.3 shows the irradiance values of pixels along a horizontal line across the center of images, polarized at 0°, 45°, 90° and 135°. The irradiance image for 135° polarization was derived from those of the other polarization angles using the relation:

$$I_{135} = I_0 + I_{90} - I_{45} \qquad (4.1)$$

This relation assumes that the total emitted energy is given by the sum of intensity in the two orthogonal components. The target plate was oriented normal to the camera. There were no significant differences in the irradiance levels between the 4 polarization angles for area within the target plate. Hence, thermal emission from a plate, at normal viewing angle, was not polarized. The irradiance contrast between the plate center and the background was low.

There was sharp transition in intensity level at the 2 vertical edges. The peaks were due to heat accumulation at the interfaces. The dips were due to the "cold" side

42

plates. The edges in the polarized images were not perfectly aligned. The slight displacement may be attributed to slight movement in the camera introduced during the switching of the polarizer.

Figure 4.4 shows similar irradiance plots for target plate at 70° viewing angle. The thermal emission from the target plate was linearly polarized with the horizontal component stronger than the vertical component and the 135° component stronger than the 45° component. Emission from the side plate and background showed no observable polarization. The irradiance contrast between the plate center and the background was higher as compared to a plate at normal viewing angle.
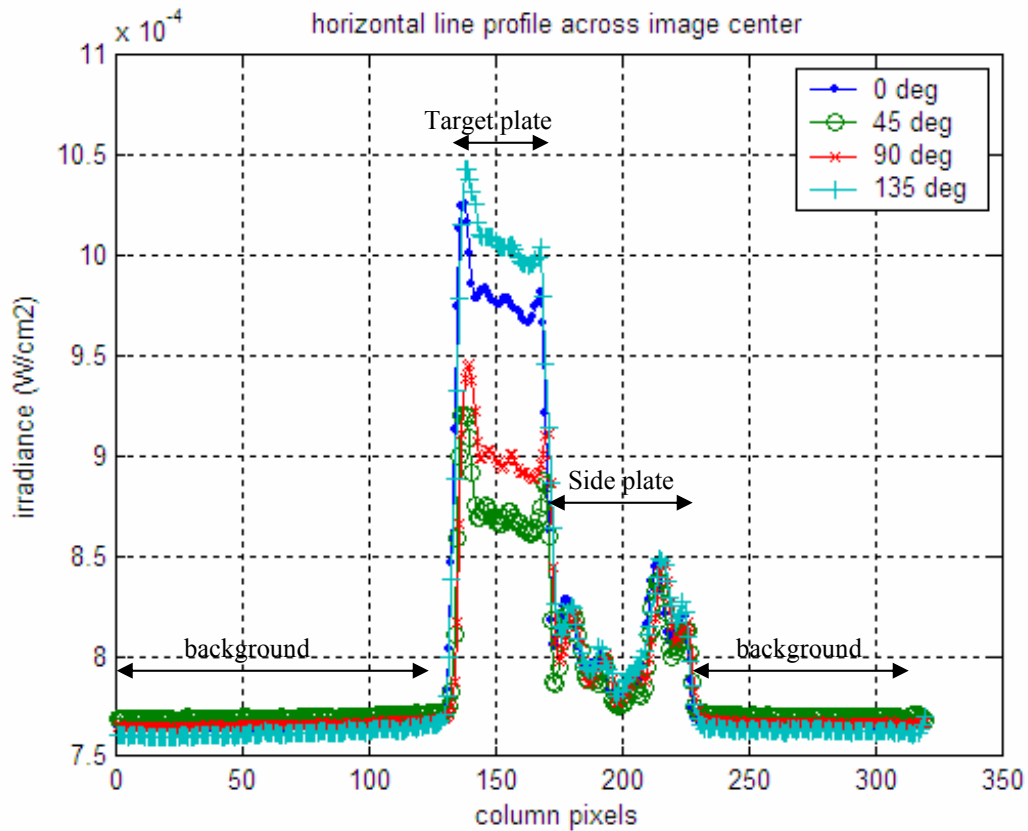
Figure 4.4:   Irradiance profile along a horizontal line across the center of the polarized images with target plate at 70° viewing angle

2. Stokes Parameters

The intensity image (Stokes parameter S_0) was computed as the sum of irradiance polarized at 0° and 90° described in Equation (2.28a)

$$S_0 = I_0 + I_{90} \tag{2.28a}$$

Figure 4.5 shows the 3-D plot of the S_0 image, with the target plate at 0° viewing angle. The intensity image showed the non-uniform heating of the plate with "hot" spots appearing in several areas. The plate intensity was close to that of the background (low contrast). Intensity peaks at the plate edges and the dips due to the "cold" side plates were evident. The cylindrical rod, which supports the target plate, was cooler than background.
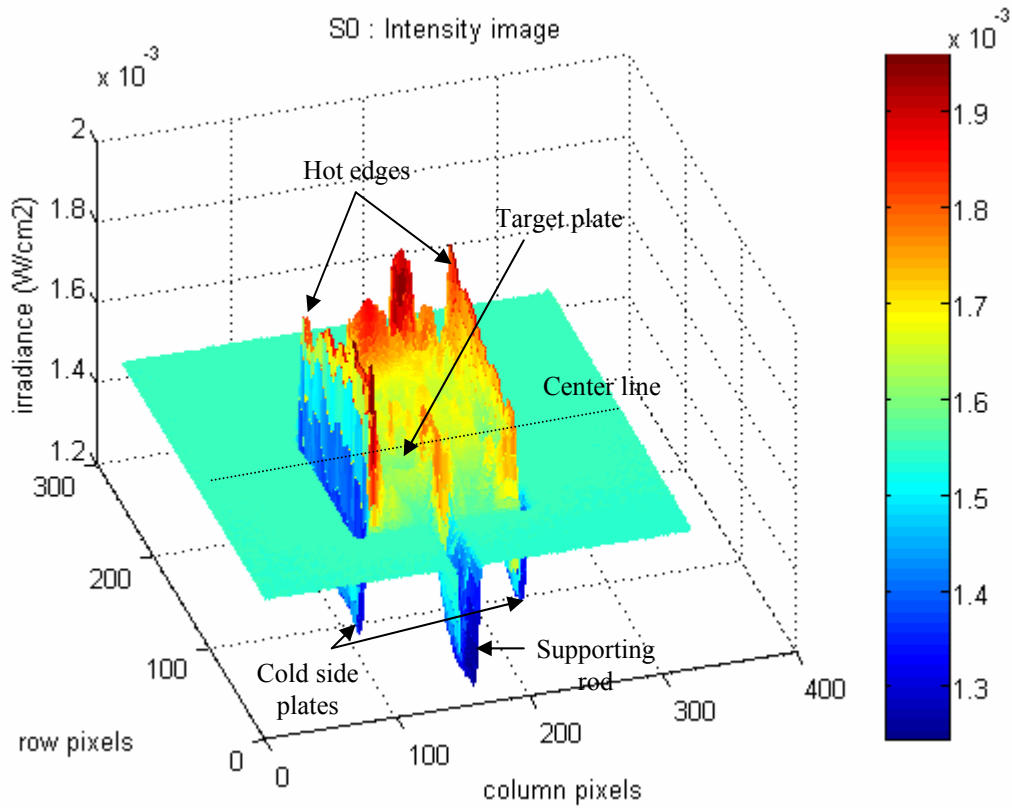
Figure 4.5:   Intensity (S_0) image of target plate at 0° viewing angle

Figure 4.6 is the S_0 profile along a horizontal line across the image center as indicated in Figure 4.5. The intensity contrast between the target plate and the background was defined as:

$$C_I = \frac{S_{0,t} - S_{0,b}}{S_{0,t} + S_{0,b}} \qquad (4.2)$$

where, $S_{0,t}$ = average intensity level of the plate

$S_{0,b}$ = average intensity level of the background

The intensity contrast was calculated to be 3%, which was low due to the small apparent temperature difference between the plate and the background.

Figure 4.6:   Intensity (S_0) profile along a horizontal line across the center of the image, with target plate at 0° viewing angle

45

Figure 4.7 and 4.8 are the 3-D plot and intensity profile plot for the target plate at 70° viewing angle. The intensity of the tilted target plate appeared more uniform. At this angle, the "cold" edges due to the side plate cannot be seen. The intensity level of the side plate is close to that of the background. The intensity of the tilted target plate was higher than when it was viewed at normal incidence. The increase in intensity with viewing angles can be attributed to a higher emissivity of metal at wide viewing angles. The intensity contrast between the target plate and background was calculated to be 10%, which is higher than that of the plate viewed at normal incidence.
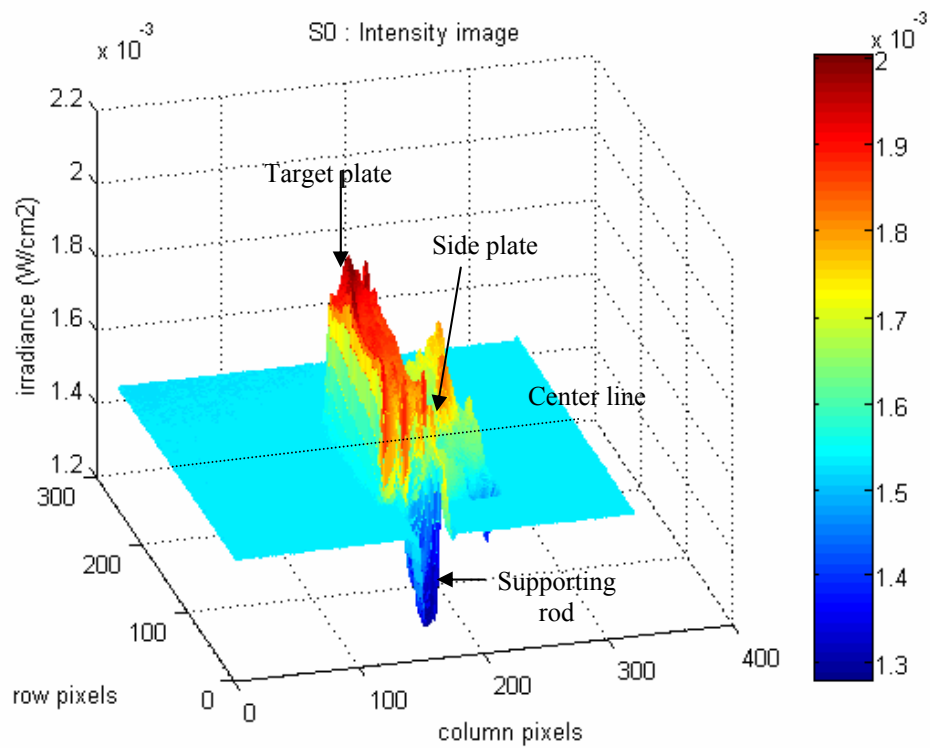
Figure 4.7:   Intensity (S_0) image of target plate at 70° viewing angle
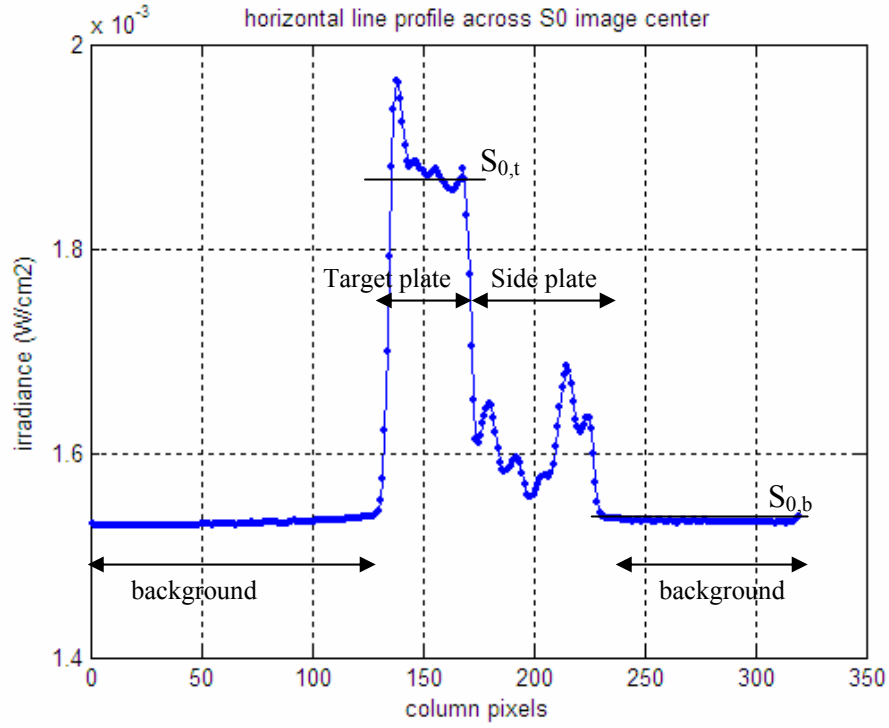
Figure 4.8:   Intensity (S_0) profile along a horizontal line across the center of the image, with target plate at 70° viewing angle

The horizontal linear polarization (Stokes parameter S_1) was computed as the difference of irradiance polarized at 0° and 90°, as defined in Equation (2.28b).

$$S_1 = I_0 - I_{90} \qquad\qquad (2.28b)$$

Figure 4.9 shows the 3-D plot of the S_1 image, with the target plate at 0° viewing angle. The target plate has low S_1 value, i.e. not polarized. The noise at the edge of the plate was introduced by misalignment of the edge pixels in the irradiance images (I_0 and I_{90}). The alignment error, coupled with the sharp transition in the irradiance level at the edges, resulted in a small but non zero S_1 value.
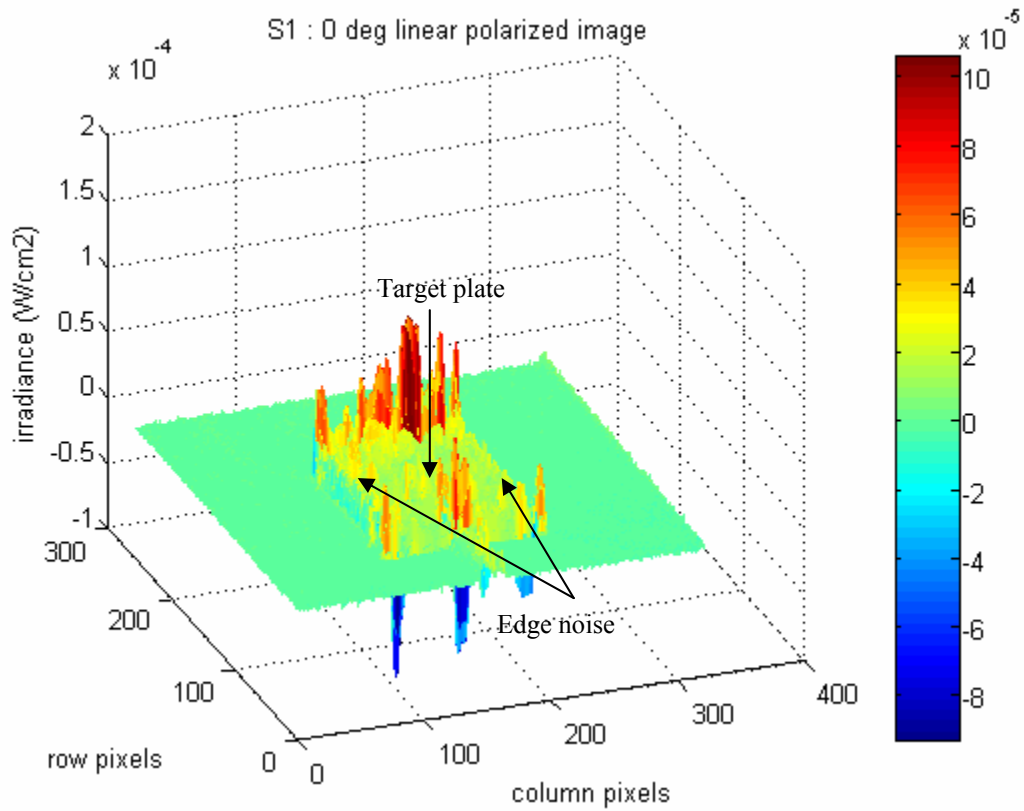
Figure 4.9:   Horizontal polarized (S_1) image of target plate at 0° viewing angle

Figure 4.10 shows the 3-D plot of the S_1 image, with the target plate at 70° viewing angle. The tilted target plate has high S_1 value, i.e. horizontally polarized. In contrast, the side plate and background were not polarized.
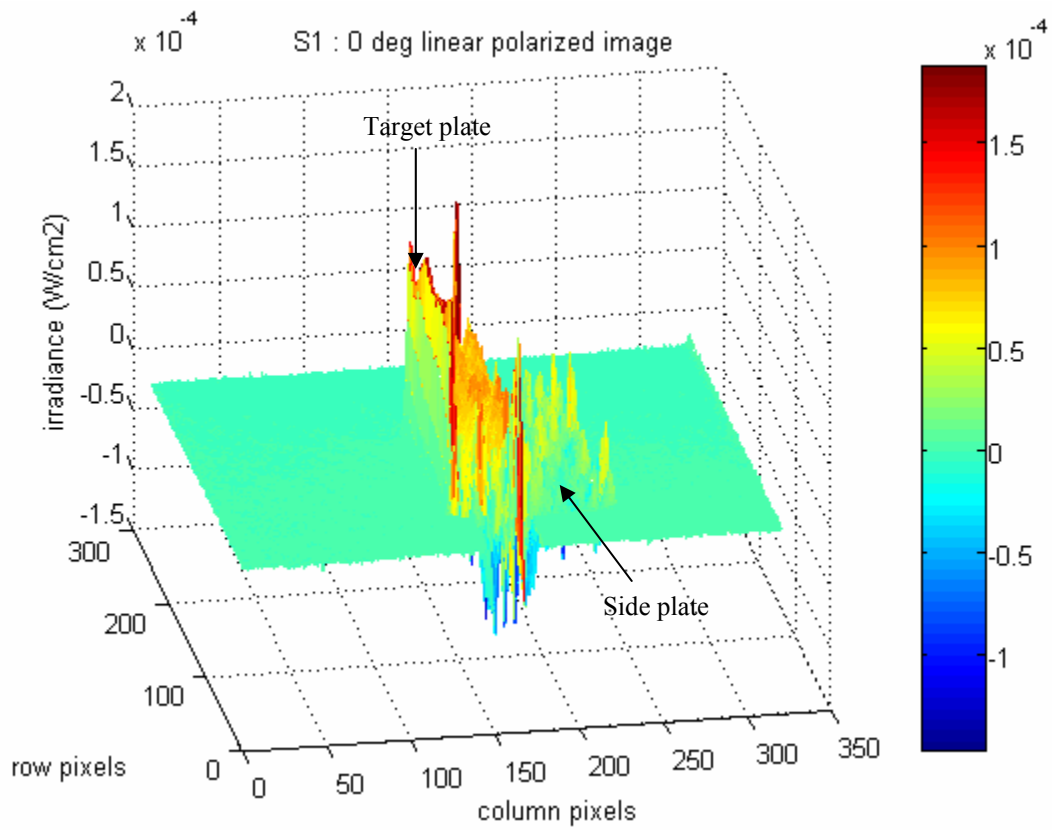
Figure 4.10:   Horizontal polarized (S_1) image of target plate at 70° viewing angle

The 45° linear polarization (Stokes parameter S_2) was computed as the difference of irradiance polarized at 45° and 135°, as defined in Equation (2.28c).

$$S_2 = I_{45} - I_{135} = 2I_{45} - I_0 - I_{90} \qquad (2.28c)$$

Figure 4.11 shows the 3-D plot of the S_2 image, with the target plate at 0° viewing angle. The target plate and background were not polarized. The noise at the edges was due to misaligned pixels in the 45° and 135° polarized irradiance images.
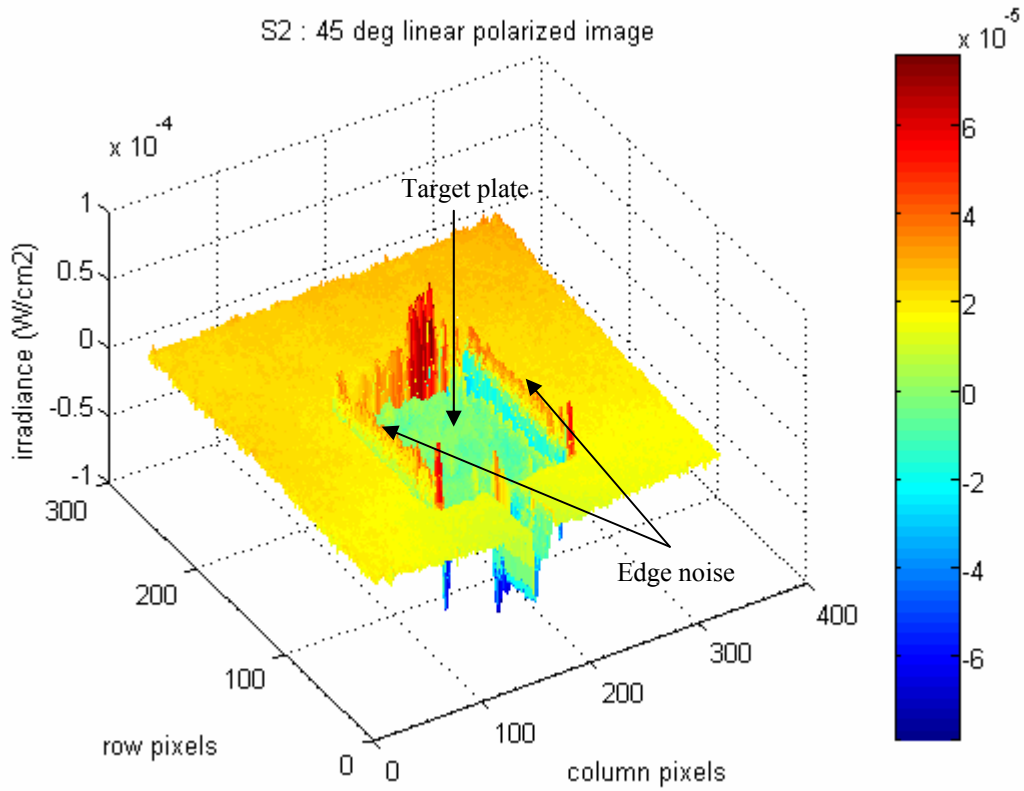
Figure 4.11:   45° polarized (S_2) image of target plate at 0° viewing angle

Figure 4.12 shows the 3-D plot of the S_2 image, with the target plate at 70° viewing angle. The tilted target plate has a negative S_2 value, indicating that the emission was linearly polarized, with 135° component stronger than the 45° component. The side plate and background were not polarized.
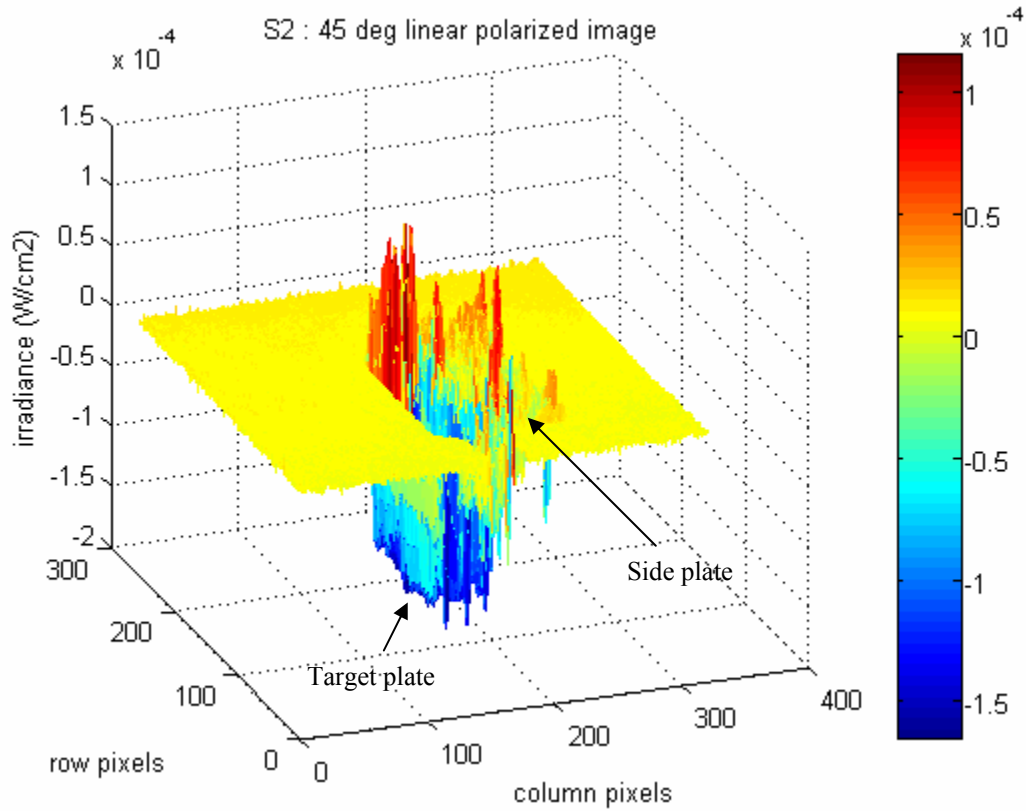
Figure 4.12: 45° polarized (S_2) image of target plate at 70° viewing angle

3. Degree of Polarization

The degree of polarization (DOP) was computed as the ratio of the total polarized signature and intensity, as defined in Equation (2.30).

$$DOP = \frac{\sqrt{S_1^2 + S_2^2}}{S_0} \tag{2.30}$$

Figure 4.13 shows the 3-D plot of the DOP image, with the target plate at 0° viewing angle. Figure 4.14 is the DOP profile along a horizontal line, across the image center. The DOP of the target plate and background was low. The noise at the edges (DOP of about 2%) was due to misalignment in the edge pixels of the irradiance images.
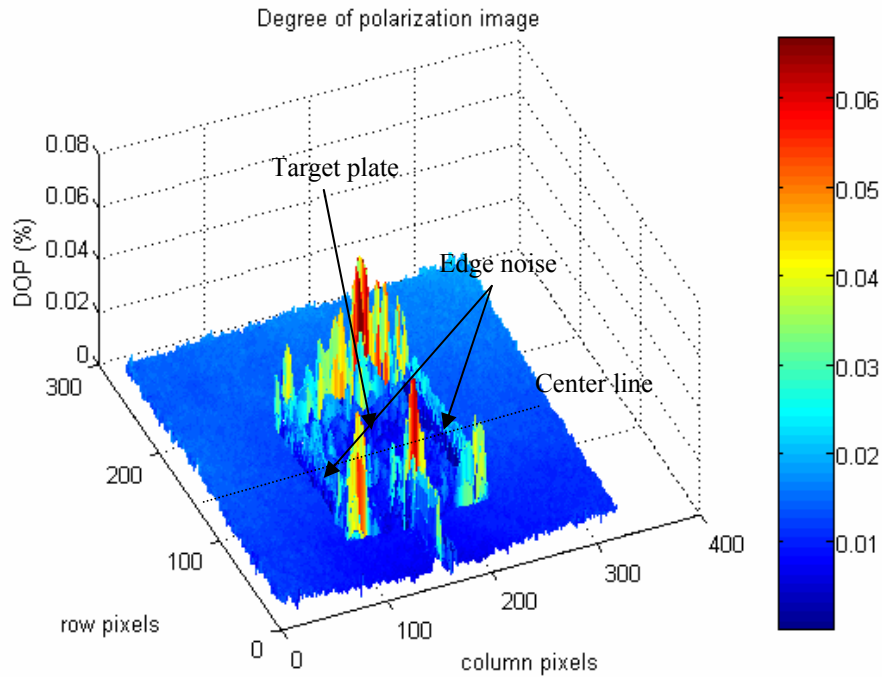
Figure 4.13:   Degree of polarization image of target plate at 0° viewing angle
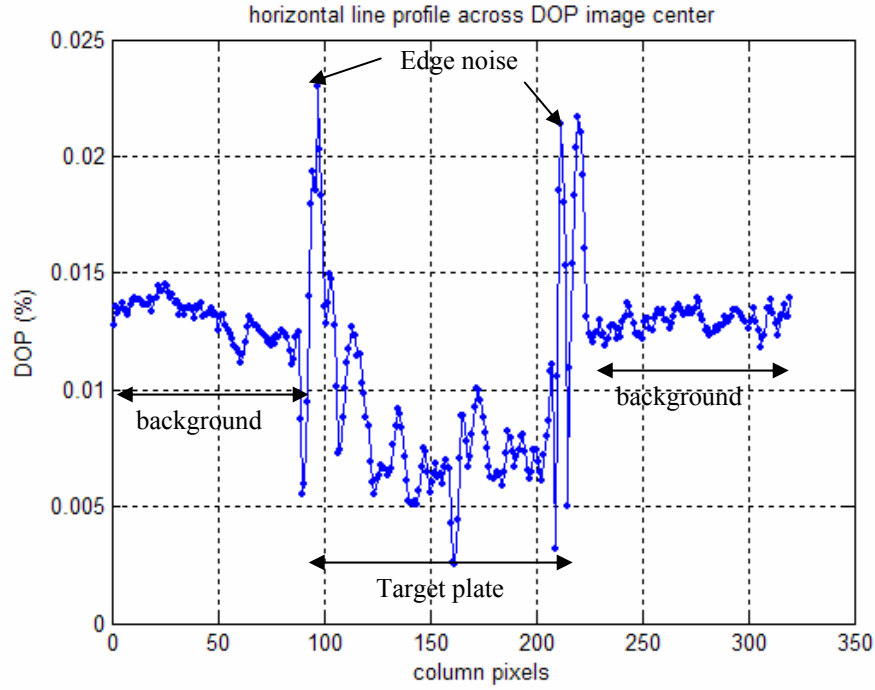
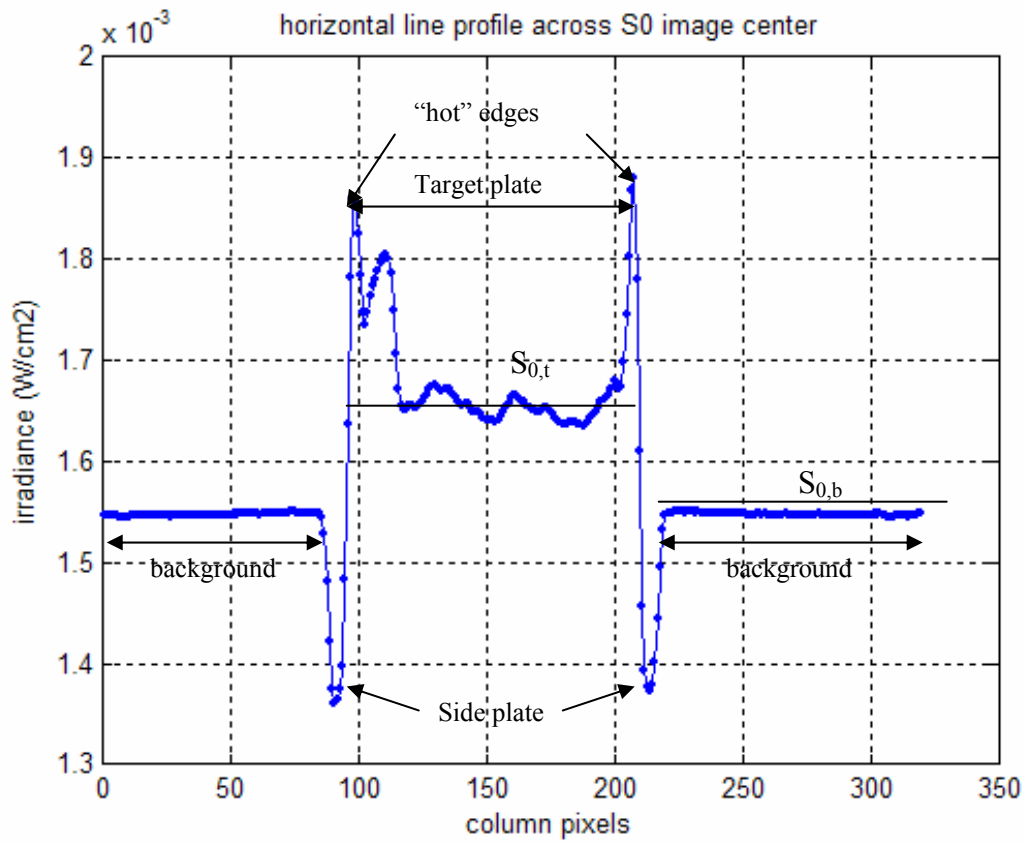Figure 4.14:   Degree of polarization profile along horizontal line across the center of the image, with target plate at 0° viewing angle

Figure 4.15 and 4.16 are the 3-D plot and line profile plot of the DOP, for target plate at 70° viewing angle. The tilted plate has a DOP of about 8.5%. In contrast, the side plate and background DOP was only 0.5%, and can be considered as not polarized. The edge effects were not as prominent as those observed for the plate at normal incidence.

The target-background contrast (C_{DOP}) was computed as:

$$C_{DOP} = \frac{DOP_t - DOP_b}{DOP_t + DOP_b}$$

(4.3)

where, DOP_t = average degree of polarization for target plate

DOP_b = average degree of polarization for background

The DOP contrast was 89%. This is higher than the intensity contrast (C_I) of 10% for the same plate at 70° viewing angle.

53
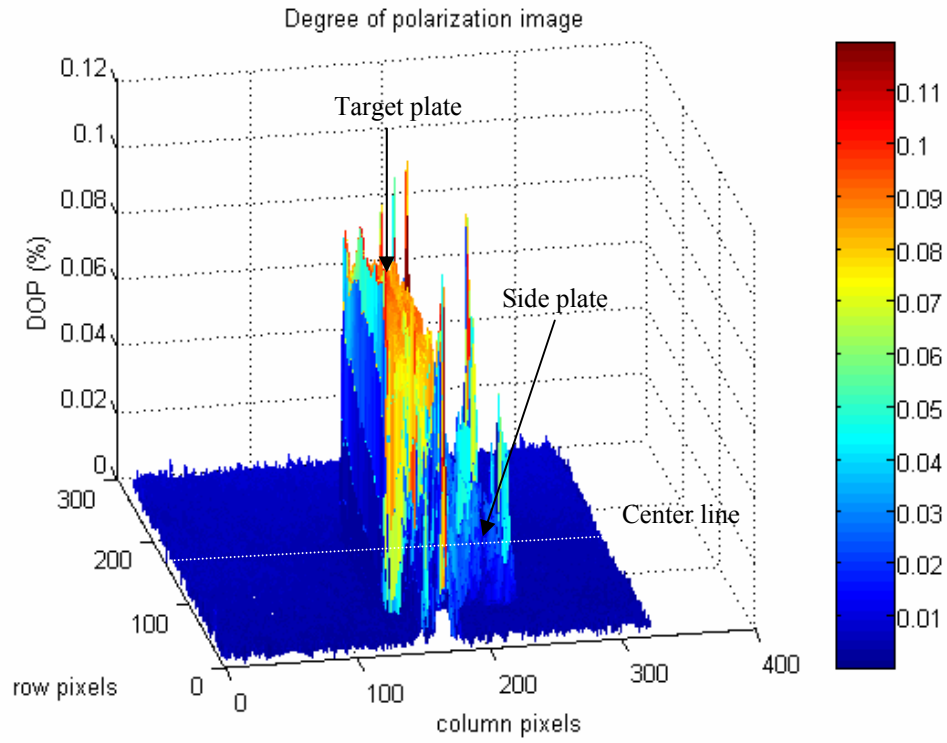
Figure 4.15: Degree of polarization image of target plate at 70° viewing angle
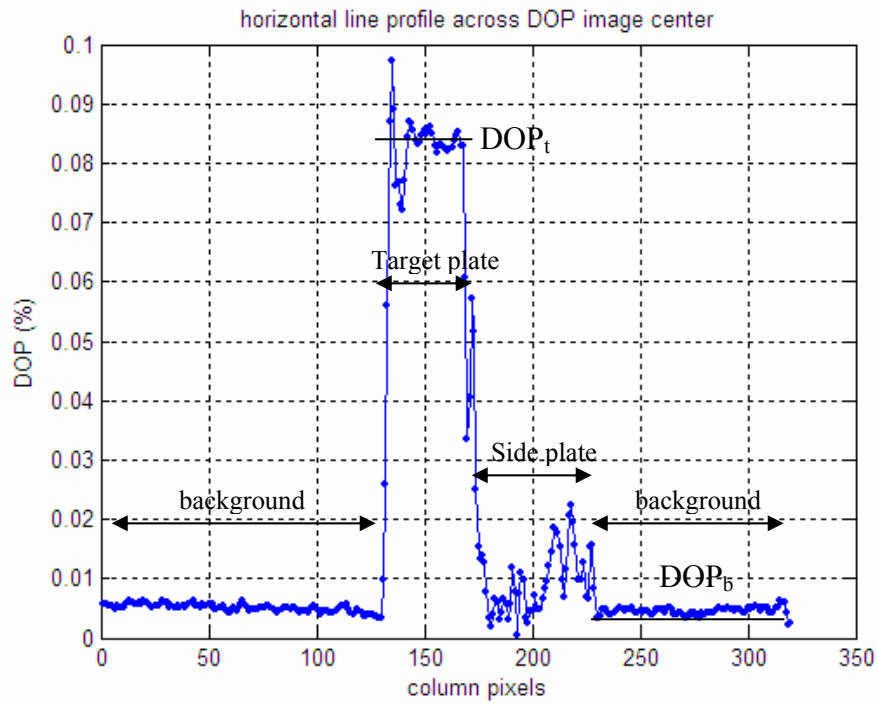
Figure 4.16: Degree of polarization profile along a horizontal line across the center of the image, with target plate at 70° viewing angle

54

4. Angle of Polarization

The angle of polarization (ψ) was defined in Equation (2.31).

$$\psi = \frac{1}{2}\tan^{-1}(\frac{S_2}{S_1})$$

(2.31)

The angle ranged from 0° to 180° and was computed based on the magnitude and sign of the Stokes parameters, S_1 and S_2, using the logic described in Figure 4.17. For un-polarized emission, both S_1 and S_2 were below the threshold value S_{thr}. The angle ψ was undefined and was set to 0°. S_{thr} was set equal to the maximum absolute value of the S_1 and S_2 parameters of an un-polarized background.
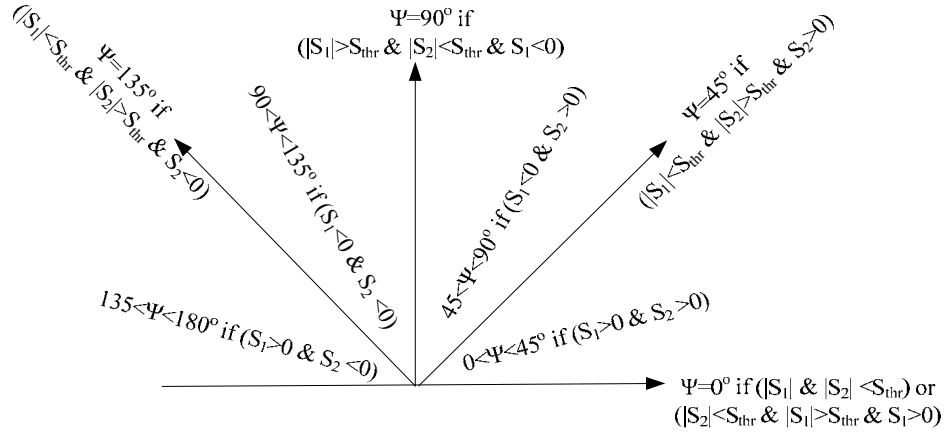
Figure 4.17:   Logic for assigning angle of polarization

Figure 4.18 shows the 3-D plot of the ψ image, with the target plate at 0° viewing angle. Figure 4.19 is the ψ profile along a horizontal line, across the image center. The target plate and background were un-polarized and have $\psi=0$. The spikes at the edges were due to noise in the Stokes images of S_1 and S_2, which was in turn caused by misaligned pixels between the irradiance images.

55
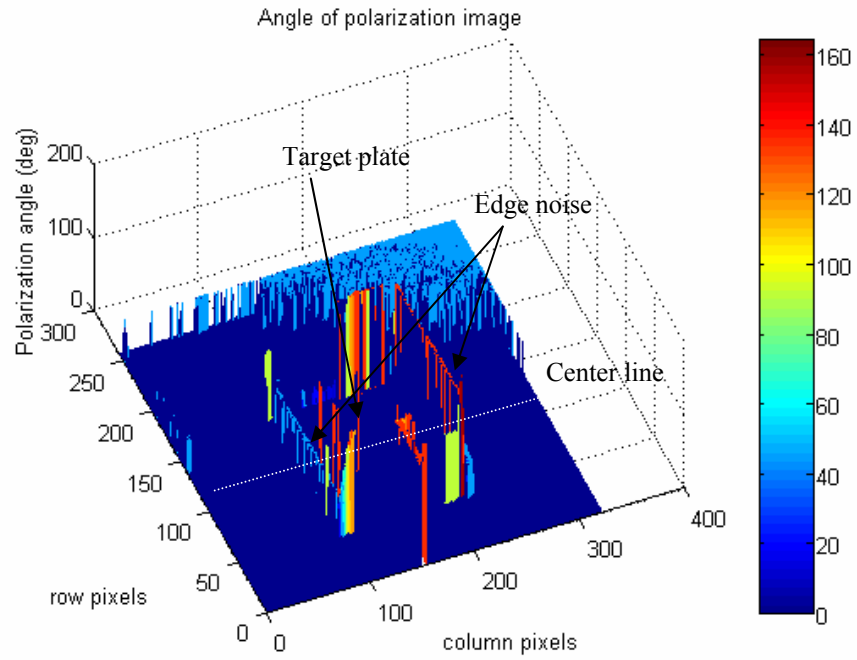
Figure 4.18:   Angle of polarization (ψ) image of target plate at 0º viewing angle
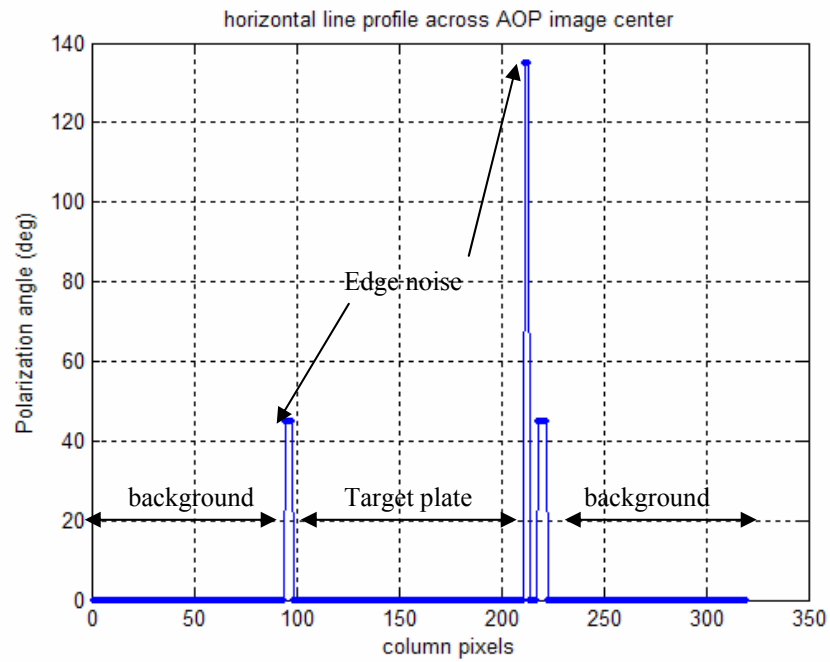
Figure 4.19:   Angle of polarization (ψ) profile along a horizontal line across the center
of the image, with target plate at 0º viewing angle

Figure 4.20 and 4.21 are the 3-D and line profile plot of the angle of polarization, for the target plate at 70° viewing angle. The polarization angle of the tilted plate was 150°, which is the result of a positive S_1 (horizontal linear polarized) and negative S_2 (135° linear polarized). In contrast, the side plate and background were largely not polarized, hence $\psi=0$.
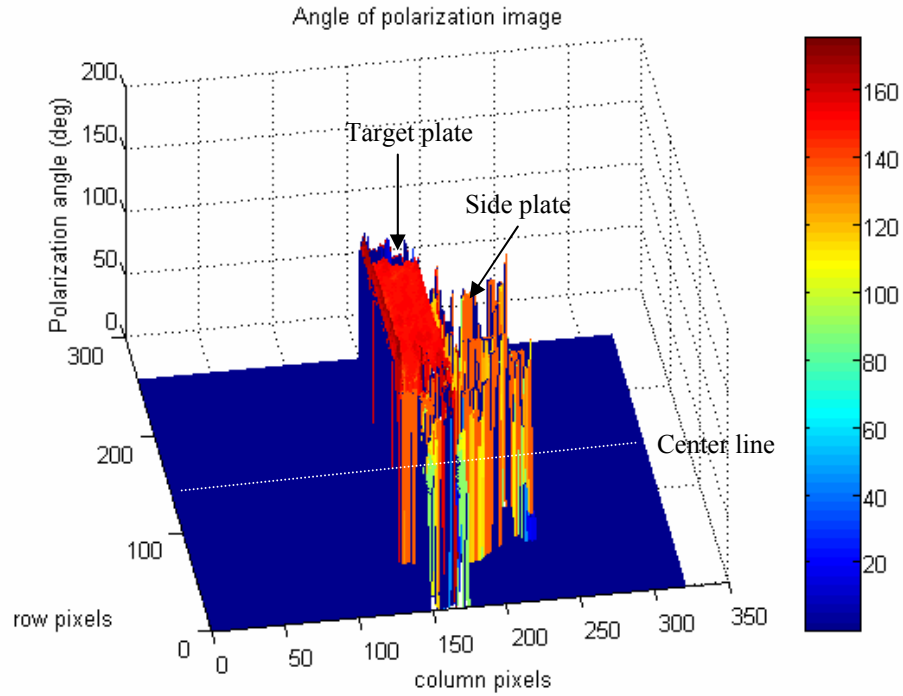
Figure 4.20:   Angle of polarization (ψ) image of target plate at 70° viewing angle
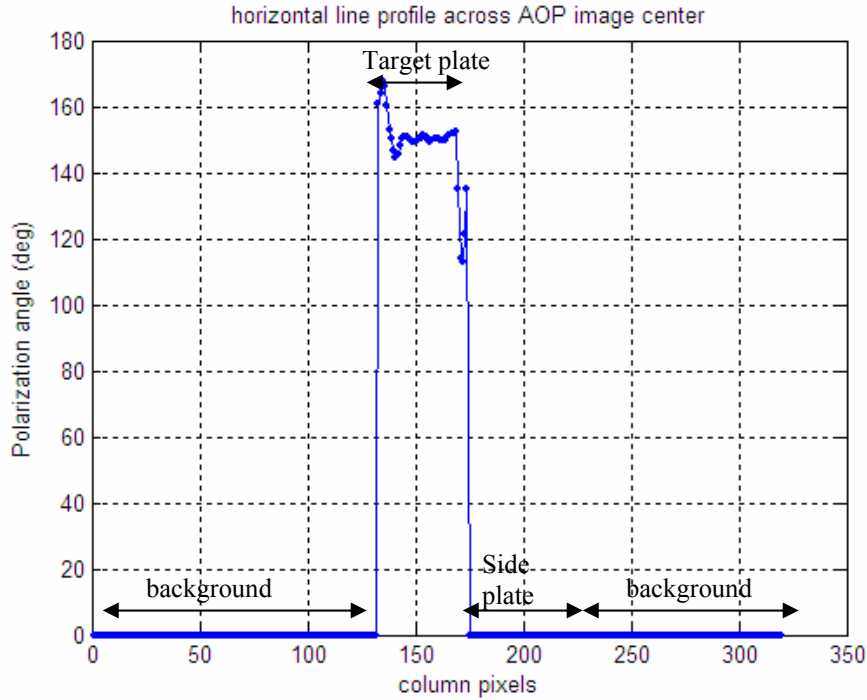
Figure 4.21: Angle of polarization (ψ) profile along a horizontal line across the center of the image, with target plate at 70° viewing angle

C.   EMISSION ANGLE DEPENDENCE

The intensity, degree of polarization (DOP) and angle of polarization (AOP) were determined for target plate at different viewing angles (0°, 20°, 40°, 60°, 70°, 80° and 85°). The mean and variance of each parameter were calculated for the target plate and background regions. The mean and variance were used as inputs to the region segmentation algorithms.

Figure 4.22 shows the plot of measured and theoretical intensity of the aluminum target plate as a function of viewing angle, and the measured intensity of the background. The background intensity was flat, as expected of blackbody at constant temperature. The measured intensity of the target plate increased with viewing angle. This trend is characteristic of emission from metal, and is opposite to the Lambertian (cos θ) decrease in intensity expected of a dielectric material.

58
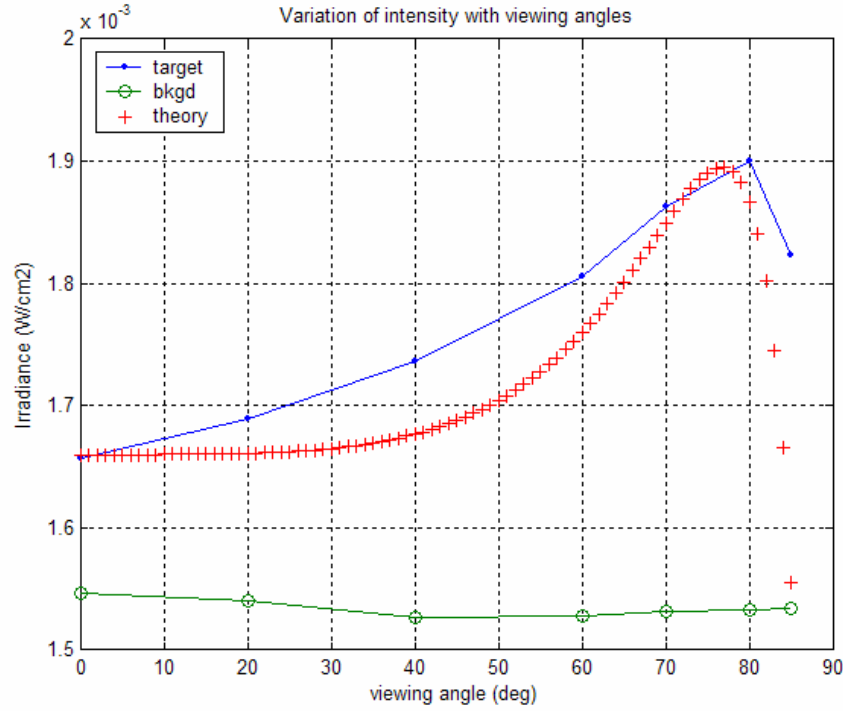
Figure 4.22:   Plots of measured and theoretical irradiance of aluminum target plate as a function of viewing angles, and measured intensity of background

From basic radiometry [4], the irradiance received by the detector element due to a non-blackbody at temperature (T) can be expressed as:

$$E(\lambda,T,\theta) = \tau\varepsilon(\lambda,\theta)M_{bb}(\lambda,T) = \tau\varepsilon(\lambda,\theta)L_{bb}(\lambda,T)\Omega \qquad (4.4)$$

where, τ = atmospheric transmission losses

$\varepsilon(\lambda,\theta)$ = emissivity of material

$L_{bb}(\lambda,T)$ = blackbody radiance in W/cm^2-sr

Ω = solid angle subtend by detector element at emitter

As plotted in Figure 2.7, the emissivity of aluminum increases with emission angle up to a peak value at around 80°. Thus, the increase in intensity can be attributed to an increase in emissivity with emission angles. The theoretical irradiance plot in Figure 4.22, shows the expected increase in irradiance with viewing angle for an aluminum plate

with complex refractive index, n_c=4.45-3.3i. The complex refractive index was selected to account for the roughness and oxidation state of the aluminum plate.

Figure 4.23 shows the plot of mean DOP of the target plate as a function of viewing angle, and DOP of the background region. The background has a relatively constant DOP of less than 1%. The DOP of the target plate at viewing angle less than 20° was less than 1%. DOP increased rapidly from 1% to 8.5%, when the viewing angle was increased from 20° to 80°. This calibrated curve relating DOP and viewing angles provides useful information for discriminating surface orientation in the target recognition process.
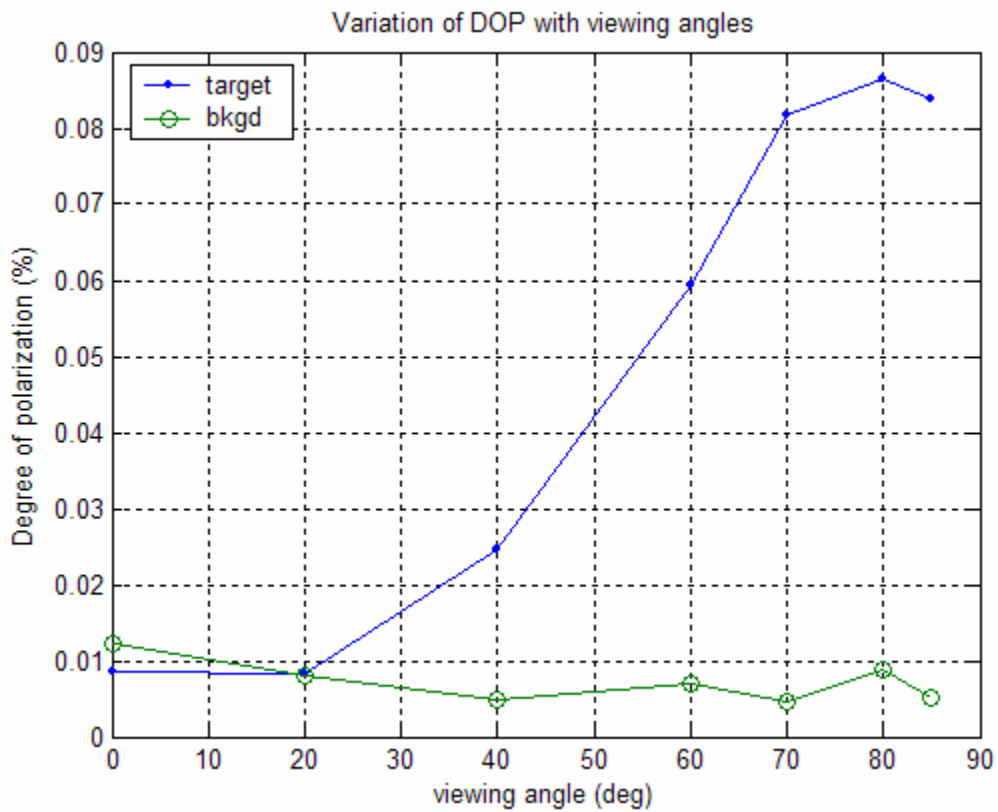
Figure 4.23:   Plot of mean degree of polarization of target plate as a function of viewing angles, and degree of polarization of the background region

Figure 2.7 shows the expected increase in DOP for aluminum, which has a maximum value of about 90% at near grazing angle. The lower DOP recorded in this work may be due to the rough metal surface and formation of a surface oxide layer, which behaves more like a dielectric film. As pointed out by Wolff et. al. [10], rough

60

surfaces and dielectric materials produce emission with lower DOP, when compared to smooth metal surfaces.

Figure 4.24 shows the plot of mean AOP of the target plate as a function of viewing angle, and AOP of the background region. The background has zero AOP as it was not polarized. The AOP for the target plate increased with viewing angle, and became constant at 150° for viewing angle greater than 60°.
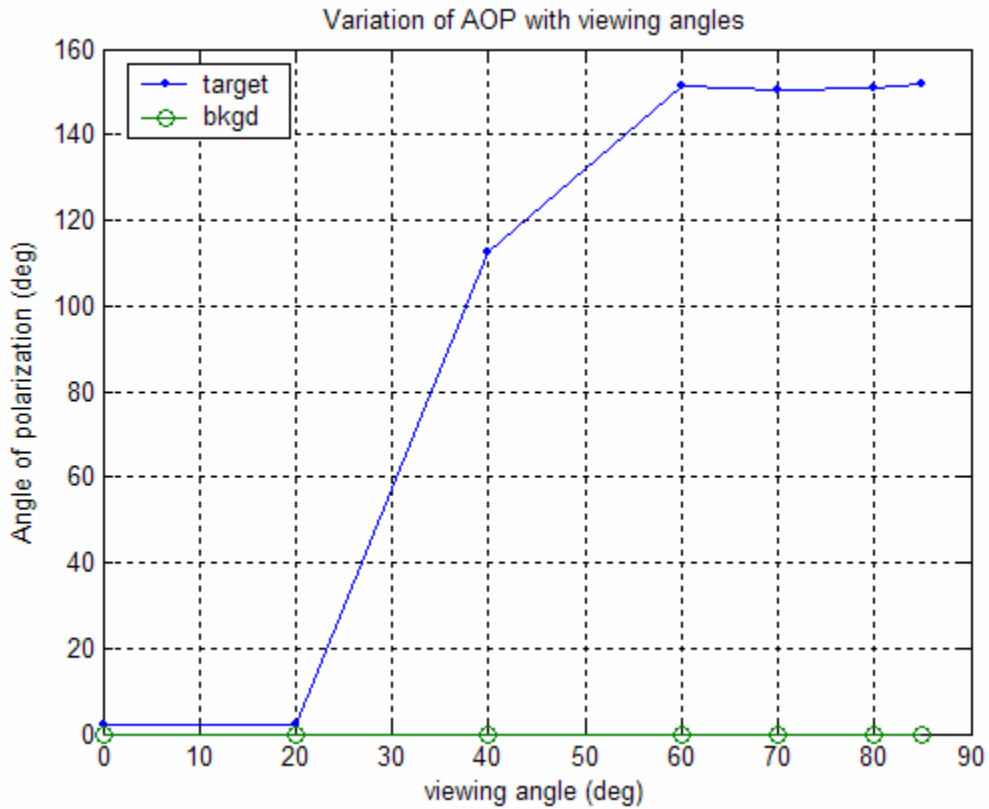
Figure 4.24:   Plot of mean Angle Of Polarization (AOP) of target plate as a function of viewing angle, and AOP for the background region

The target-background contrasts based on intensity and DOP, as defined in Equation (4.2) and (4.3), respectively, are plotted in Figure 4.25. The intensity contrast increased slightly from 5 to 10% with viewing angle. This was due to the slight increase in target plate's intensity with viewing angle as shown in Figure 4.22. In comparison, the contrast based on DOP increased with viewing angle from 0% at 20° to a maximum value of 90% at 70°. The higher target-background contrast provided by DOP at viewing angle

61

greater than 20° can potentially improve the probability of detection and reduce false alarms in the target detection process. The image processing results in Chapter V confirmed that polarization data can enhance the accuracy of the segmentation of a plate oriented at large angle from the sensor line of sight.
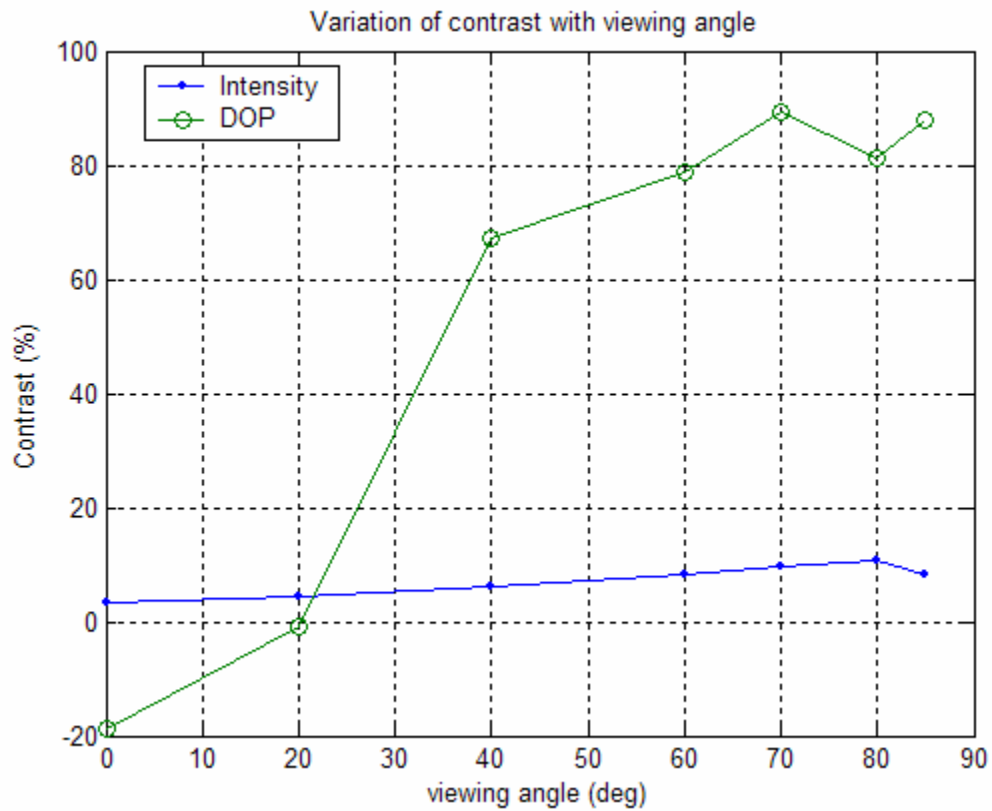
Figure 4.25: Target to background contrast based on intensity and degree of polarization

V. IMAGE PROCESSING

The objective of image processing is to segment the target plate from its background. The algorithms computed the texture-based, similarity metric by fusing information from image intensity, degree of polarization and polarization angle. Histogram threshold techniques were applied to obtain the Receiver Operating Characteristic (ROC) curves. A Constant False Alarm Rate (CFAR) threshold was chosen to segment the target from the background. Segmentation accuracy and false alarm rate were quantified.

A. IMAGE PROCESSING ALGORITHMS

The image processing algorithms were implemented in Matlab. The program listings are included in Appendix C. The programs convert the input digital images into irradiance images, from which the Stokes parameters are calculated. The intensity, degree of polarization and polarization angle images are then computed from the Stokes parameters.

1. Statistical Similarity Metric

Segmentation of the target from background was performed using the statistical similarity metric, Fisher distance:

$$F = \frac{(\mu_m - \mu_r)^2}{(\sigma^2_m + \sigma_r^2)} \tag{5.1}$$

The metric measures the difference between the mean value (μ_m) of the image pixel and that of the reference target pixel (μ_r), normalized with the sum of their variances (σ_m^2 and σ_r^2). The reference mean (μ_r) and variance (σ_r^2) were calculated from the target intensity (S_0), degree of polarization (DOP) and polarization angle (AOP) images as described in Chapter IV. The measured mean (μ_m) and variances (σ_m^2) were calculated over a local 3x3 pixel sliding window in the S_0, DOP and AOP images. A separate two dimensional Fisher distance matrix was calculated for the intensity, degree of polarization and

63

polarization angle image. Each element in the matrix represents the similarity of that pixel to the reference target pixel. A target pixel will have a smaller Fisher distance as compared to a background pixel.

The Fisher distance matrices corresponding to each parameter are fused together using Equation (2.32).

$$F = n_I \frac{(\mu_{I,m} - \mu_{I,r})^2}{(\sigma^2_{I,m} + \sigma^2_{I,r})} + n_P \frac{(\mu_{P,m} - \mu_{P,r})^2}{(\sigma^2_{P,m} + \sigma^2_{P,r})} + n_\psi \frac{(\mu_{\psi,m} - \mu_{\psi,r})^2}{(\sigma^2_{\psi,m} + \sigma^2_{\psi,r})} \quad (2.32)$$

where, n_I, n_P and n_ψ are the weights representing the contribution from the intensity, degree of polarization and polarization angle image, respectively. The data fusion schemes and the corresponding weights are shown in Table 5.1. The contribution from each data type was normalized to a value between 0-1.

Fusion schemes	n_I	n_P	n_ψ
S_0-only	1	0	0
DOP-only	0	1	0
AOP-only	0	1	0
S_0 and DOP	0.5	0.5	0
S_0, DOP and AOP	0.33	0.33	0.33

Table 5.1:   Weight assignments for different data fusion schemes

For each of the fusion schemes described in Table 5.1, a histogram of the Fisher distance was generated. An example of the histogram, for a target plate at 70° viewing angle, is shown in Figure 5.1. The Fisher distance (x-axis) was divided into discrete bin whose width was calculated as the ratio of the range and number of bins. The y-axis showed the number of pixels whose Fisher distance falls within each bin. The pixels with Fisher distance near to zero were likely to be target pixels, while the bulk of the other pixels farther to the right belonged to the background. The range and bin number were varied for each scheme to obtain sufficient resolution over the range of interest.
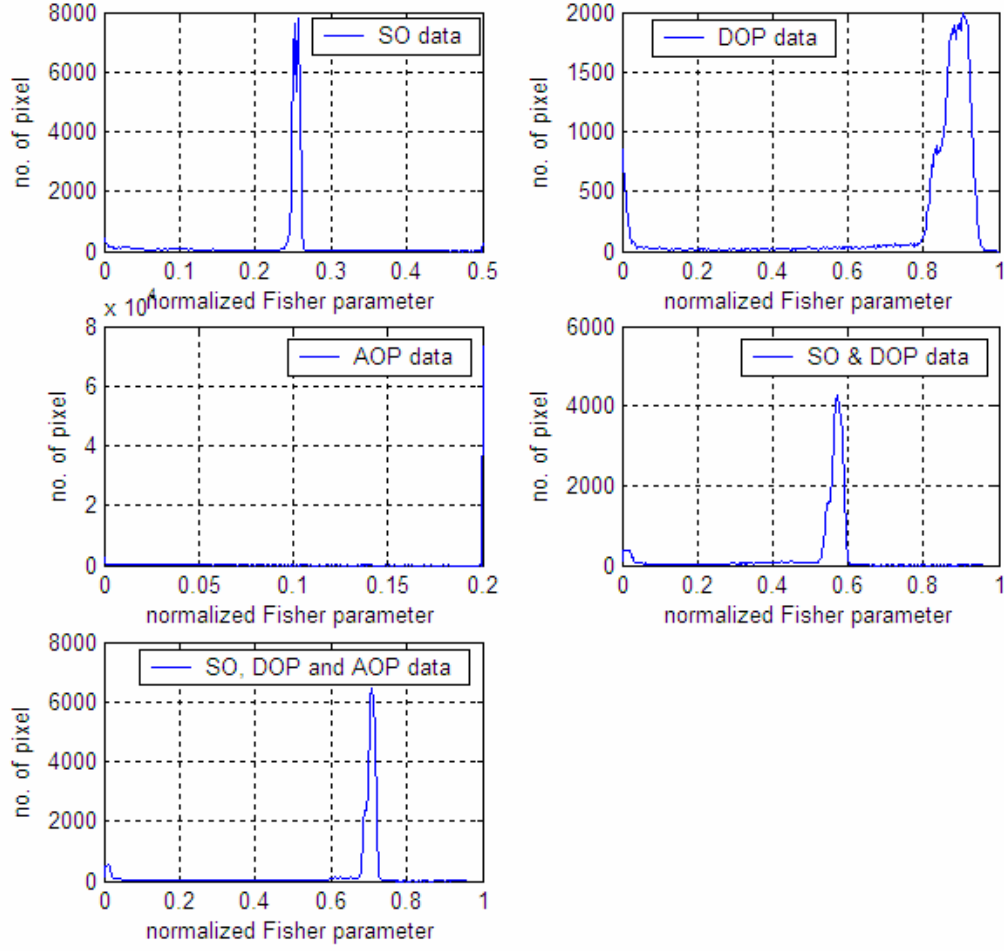
Figure 5.1:   Histogram of Fisher distance for different fusion schemes, for target plate at 70° viewing angle

2.   Receiver Operating Characteristic (ROC)

The Receiver Operating Characteristic (ROC) curves describe the performance of the segmentation process, in terms of segmentation accuracy (SA) against false alarm rate (FAR). The SA and FAR are defined in Equation (2.33) and (2.34), respectively.

$$SA = \frac{T \cap G}{T \cup G} \tag{2.33}$$

$$FAR = \frac{\overline{(T \cap G)}}{G} \tag{2.34}$$

65

In deriving the ROC curve, the range and number of bins in the histogram were adjusted to obtain sufficient data points on the curve. Data points on the curve were obtained by plotting the SA against the corresponding FAR, for varying threshold values within the range of the Fisher distance. For each threshold value, the binary output was designated as the segmented target area (T). The user can define the reference target area (G) by drawing a polygon to enclose the area of interest. The ROC curves for each of the fusion schemes were plotted. The better scheme will yield a ROC curve with higher SA for a given FAR.

For each of the fusion schemes, the threshold value of Fisher distance (F) that produced the same FAR (CFAR) was computed. The computed thresholds were applied on the Fisher distance image, to obtain the binary image of the segmented target. The corresponding SA and FAR were extrapolated from the ROC curve.

B.   REGION SEGMENTATION RESULTS

The objective was to compare the effectiveness of different fusion schemes in the segmentation of the target plate at different viewing angles, ranging from 0° to 80°. The ROC curves and the binary images for each case were derived.

1.   Target Plate at 0° Viewing Angle

Figure 5.2 shows the ROC curves produced by the different fusion schemes for 0° viewing angle. The intensity-only (S_0) data produced the best segmentation accuracy (SA), with low false alarm rate (FAR). The peak SA was 88% with corresponding FAR of 6%. In contrast, the degree of polarization-only (DOP) and polarization angle-only (AOP) data produced low SA of 20% and 10%, respectively. This is not surprising, as emission from plate at normal viewing angle was not polarized. The fusion of S_0, DOP and AOP did not yield better segmentation results.

Figure 5.2: Receiver Operating Characteristic curves produced by different fusion schemes for the case where the target plate was at 0° viewing angle

Figure 5.3 shows the segmentation results for the different fusion schemes with threshold values chosen based on a CFAR of 10%. The top left image is the reference target area (G). As expected, the intensity-only data yielded the best result. The square plate was clearly segmented from the background. The binary images produced by the DOP-only and AOP-only data did not include the target plate. The vertical edges were due to false polarization contributed by misalignment in the irradiance images.

Table 5.2 shows the threshold values used, SA, and FAR, produced by each fusion scheme for a CFAR of 10%. The SA was 86% for the intensity-only data, which was much higher than those produced by the polarized data and fused data.
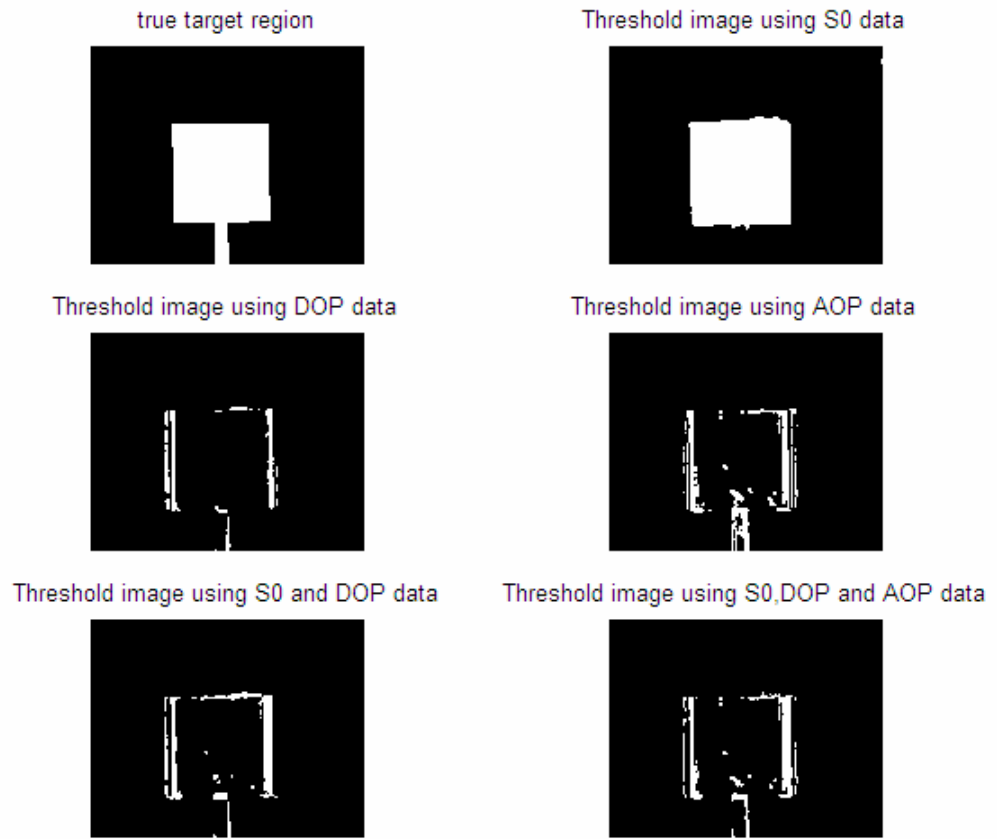
Figure 5.3: Segmented target regions produced by different fusion schemes for the case where the target plate was at 0° viewing angle

CFAR=10%			
Fusion schemes	Threshold values	SA (%)	FAR (%)
S_0-only	0.1913	86.3	9.9
DOP-only	0.0925	4.3	9.8
AOP-only	0.125	15.6	10
S_0 and DOP	0.1905	11.4	10
S_0, DOP and AOP	0.1826	12.3	9.9

Table 5.2: The threshold value used and resulting segmentation accuracy and false alarm rate for the case where the target plate was at 0° viewing angle

2. Target Plate at 20° Viewing Angle

Figure 5.4 shows the ROC curves produced by the different fusion schemes at 20° viewing angle. The intensity-only (S_0) data again produced the best results, with peak SA of 75% and corresponding FAR of 20%. The high FAR was due to the side plate in the segmented image, which was not in our defined region of interest. Other schemes yielded SA less than 20% for FAR below 40%. At higher FAR, the SA of the fused data approached that of the S_0 data.
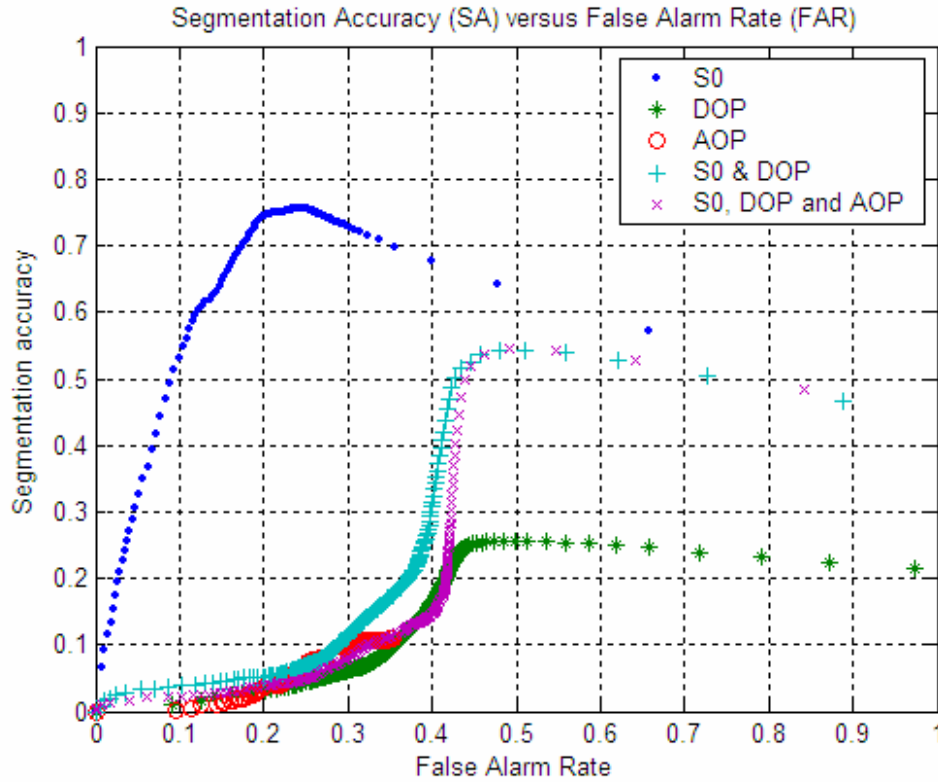
Figure 5.4: Receiver Operating Characteristic curves produced by different fusion schemes for the case where the target plate was at 20° viewing angle

Figure 5.5 shows the segmentation results for the different fusion schemes with threshold values chosen based on a CFAR of 20%. The top left image is the reference target area (G). As expected, the intensity-only data yielded the best result. The tilted target plate was clearly segmented from the background. In addition, the side plate was also extracted, which contributed to false alarms. It is interesting to note that the DOP, AOP and fused data produced good segmentation of the side plate. The side plate being mounted at right angle to the target plate was at 70° viewing angle. Emission at this angle was polarized.

Figure 5.5:   Segmented target regions produced by different fusion schemes for the case where the target plate was at 20° viewing angle

Table 5.3 shows the threshold values used, SA, and FAR, produced by each fusion scheme for a CFAR of 20%. The SA was 74% for the intensity-only data, which was much higher than those produced by the polarized data and fused data. The low SA produced by the polarized data can be attributed to the incorrect segmentation of the side plate.

CFAR=20%			
Fusion schemes	Threshold values	SA (%)	FAR (%)
S_0-only	0.0983	74.4	20
DOP-only	0.0233	3	19.3
AOP-only	0.0113	3.5	19.7
S_0 and DOP	0.0639	5.2	19.9
S_0, DOP and AOP	0.063	3.7	19.3

Table 5.3:   The threshold value used and resulting segmentation accuracy and false alarm rate for the case where the target plate was at 20° viewing angle

3. Target Plate at 40° Viewing Angle

Figure 5.6 shows the ROC curves produced by the different fusion schemes at 40° viewing angle. The intensity-only (S_0) data produced the best results, with peak SA of 75% and corresponding FAR of 18%. The high FAR was due to part of the side plate in the segmented image, which was not in our defined region of interest. Other schemes, except the AOP-only data, yielded SA less than 20% for FAR below 50%. At higher FAR, the SA of all the schemes approached the same value.
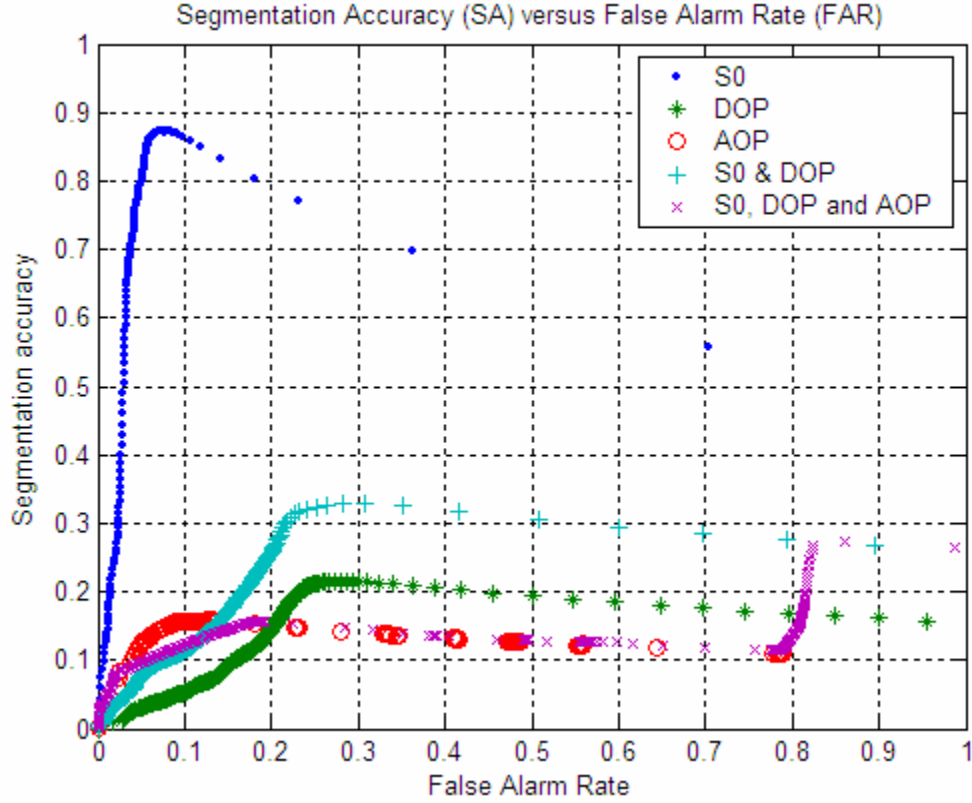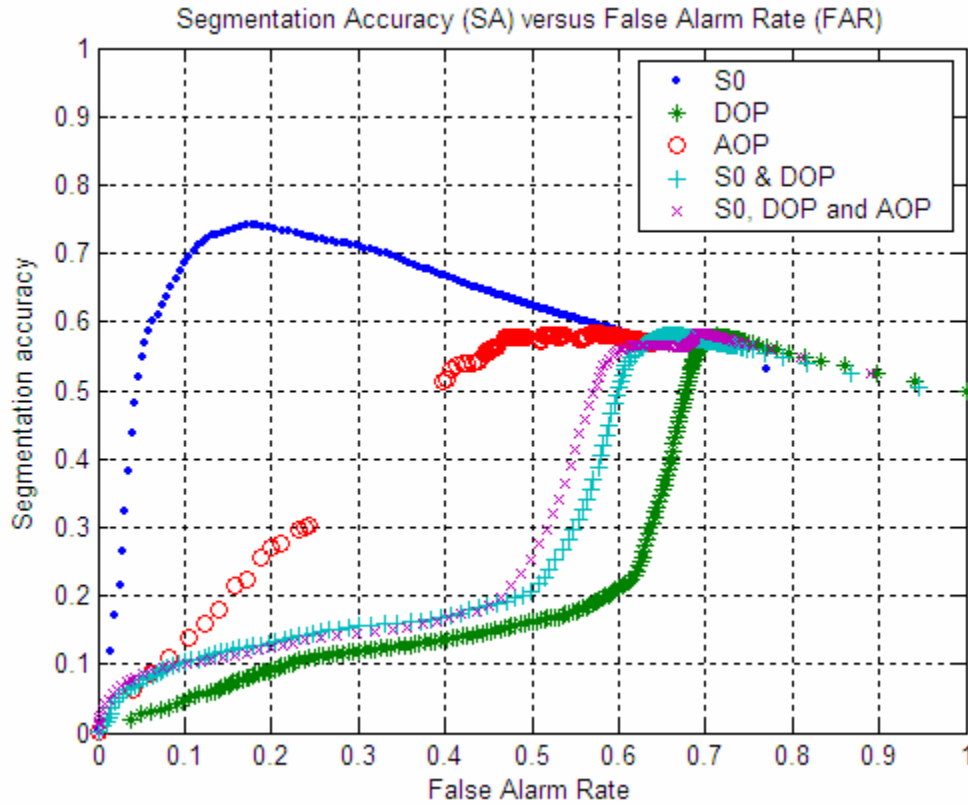

Figure 5.6:   Receiver Operating Characteristic curves produced by different fusion schemes for the case where the target plate was at 40° viewing angle

Figure 5.7 shows the segmentation results for different fusion schemes with threshold values chosen based on a CFAR of 20%. The top left image is the reference target area (G). As expected, the intensity-only data yielded the best result. The tilted target plate was clearly segmented from the background. In addition, part of the side plate was also extracted, which contributed to false alarms. The rest of the schemes did not produce any contiguous regions as emission from both the target plate (40° viewing angle) and side plate (50° viewing angle) were not significantly polarized.
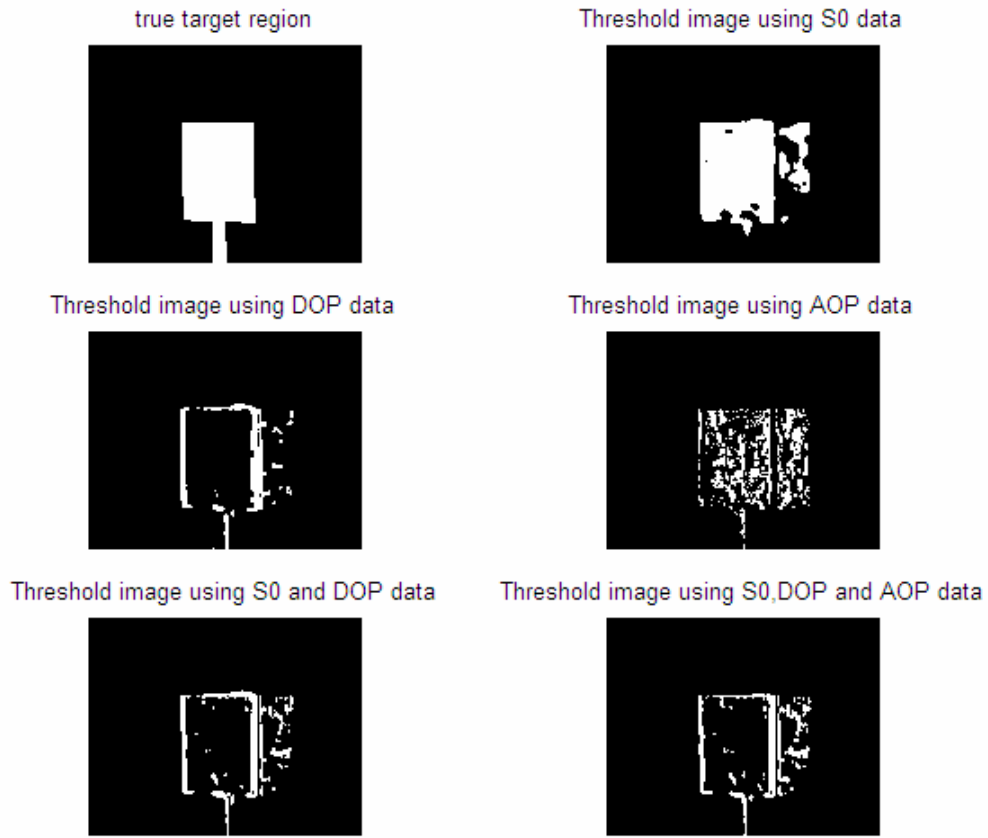
Figure 5.7:   Segmented target regions produced by different fusion schemes for the case where the target plate was at 40° viewing angle

Table 5.4 shows the threshold values used, SA, and FAR, produced by each fusion scheme for a CFAR of 20%. The SA was 74% for the intensity-only data, which was much higher than those produced by the polarized data and fused data.

CFAR=20%			
Fusion schemes	Threshold values	SA (%)	FAR (%)
S_0-only	0.06	73.9	19.7
DOP-only	0.1033	9.2	20
AOP-only	0.0067	27.1	19.8
S_0 and DOP	0.1109	13.1	19.6
S_0, DOP and AOP	0.0836	12.4	20

Table 5.4:   The threshold value used and resulting segmentation accuracy and false alarm rate for the case where the target plate was at 40° viewing angle

4.   Target Plate at 60° Viewing Angle

Figure 5.8 shows the ROC curves produced by the different fusion schemes at 60° viewing angle. The fusion of S_0, DOP and AOP produced the best result, with peak SA of 80% and corresponding FAR of 10%. This was due to good segmentation accuracy of both the DOP-only and AOP-only data. The peak SA for the intensity-only data was 75% at FAR of 10%, which was slightly lower than the other schemes.
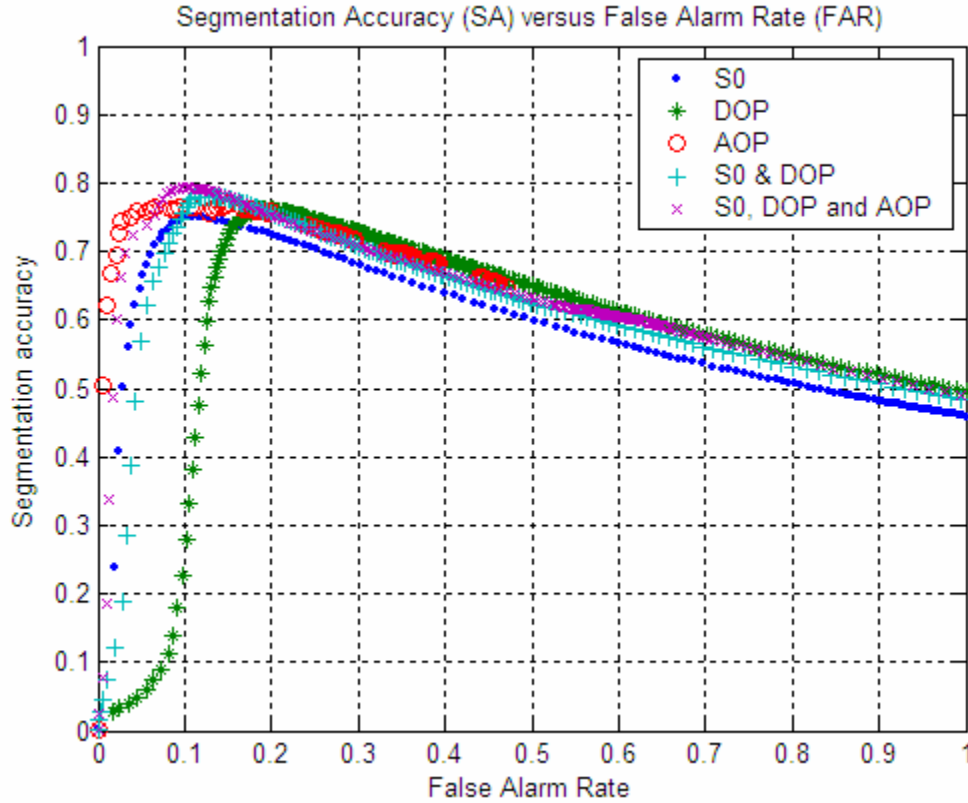
Figure 5.8:   Receiver Operating Characteristic curves produced by different fusion schemes for the case where the target plate was at 60° viewing angle

Figure 5.9 shows the segmentation results for the different fusion schemes with threshold values chosen based on a CFAR of 20%. The top left image is the reference target area (G). The fused data of S_0, DOP and AOP yielded the best result. The tilted target plate was clearly segmented from the background and the side plate was suppressed. The good segmentation results produced by the DOP and AOP data were due to the high degree of polarization and distinct angle of polarization of the emission from the target plate at 60° viewing angle. The emission from the side plate (30° viewing angle) was not polarized. In comparison, the image produced by the intensity-only data contained missing spots on the target plate and false detections on the side plate.
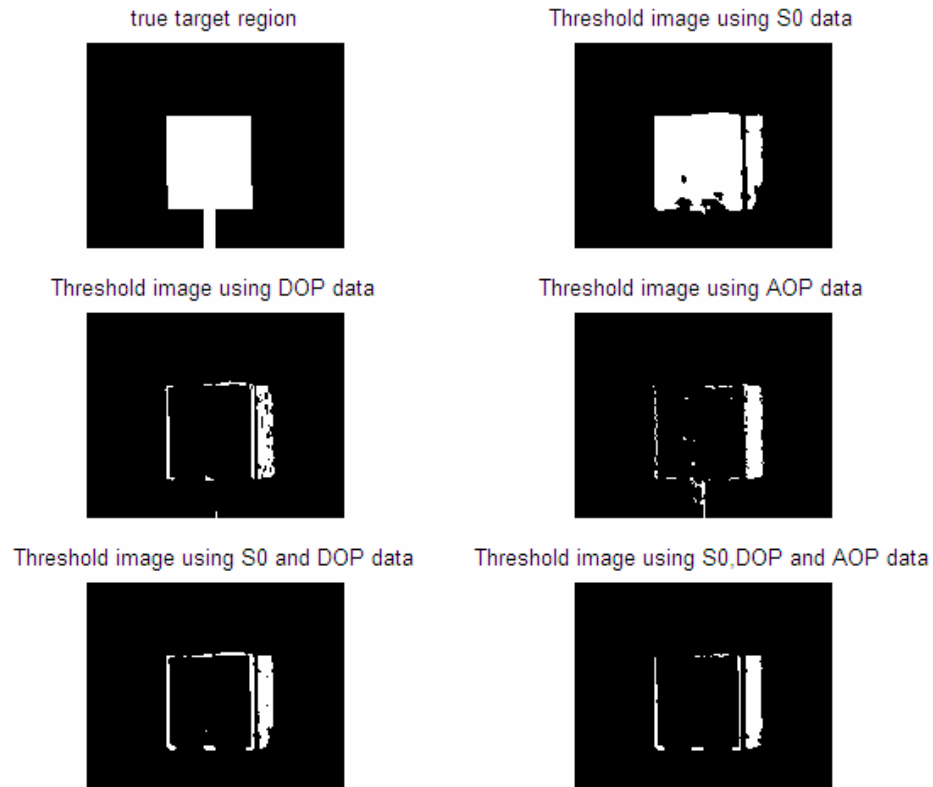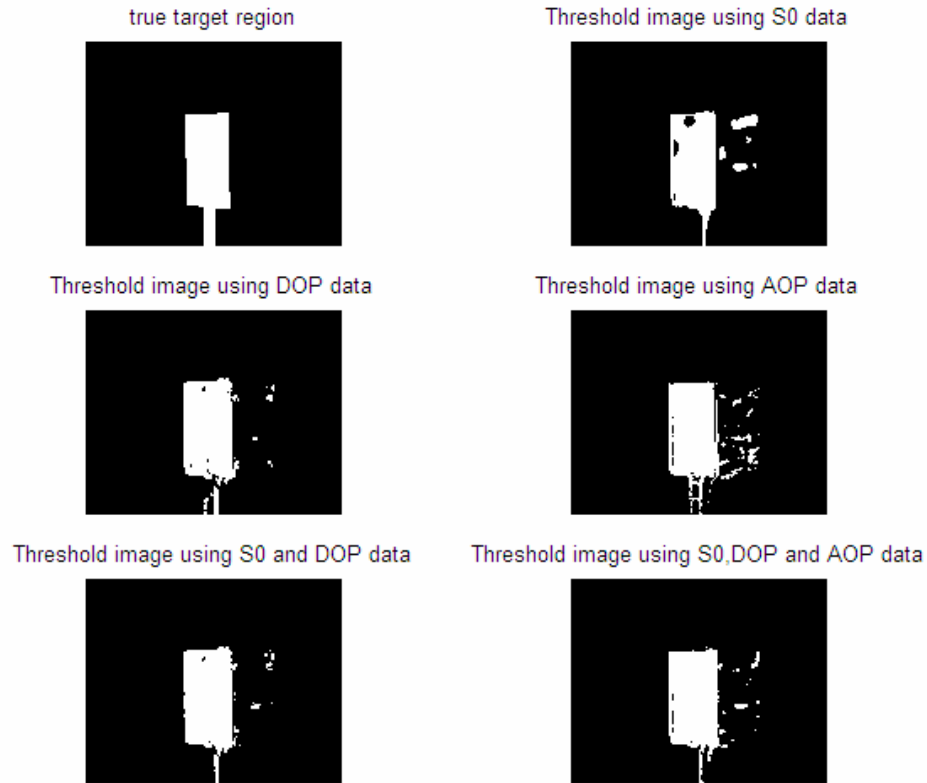

Figure 5.9:   Segmented target regions produced by different fusion schemes for the case where the target plate was at 60° viewing angle

Table 5.5 shows the threshold values used, SA and FAR produced by each fusion scheme for a CFAR of 20%. The SA for the polarized data and fused data was very similar at around 76%. This is slightly higher than the 73% SA produced by the intensity-only data. The enhancement in segmentation accuracy was 3%.

CFAR=20%			
Fusion schemes	Threshold values	SA (%)	FAR (%)
S_0-only	0.0517	72.6	19.6
DOP-only	0.1567	76.1	20
AOP-only	0.0233	75.7	19.9
S_0 and DOP	0.1494	75.6	19.9
S_0, DOP and AOP	0.1432	75.3	19.9

Table 5.5: The threshold value used and resulting segmentation accuracy and false alarm rate for the case where the target plate was at 60° viewing angle

5. **Target Plate at 70⁰ Viewing Angle**

Figure 5.10 show the ROC curves produced by the different fusion schemes at 70° viewing angle. Both the AOP-only data and the fusion of S_0, DOP and AOP, produced the best result, with peak SA of 80% and corresponding FAR of about 5%. Both the DOP-only data and fusion of S_0 and DOP, produced similar results, with peak SA of 75%, at FAR of 10%. The intensity-only data produced the worst result among the schemes, with peak SA of only 60%, at FAR of 30%.
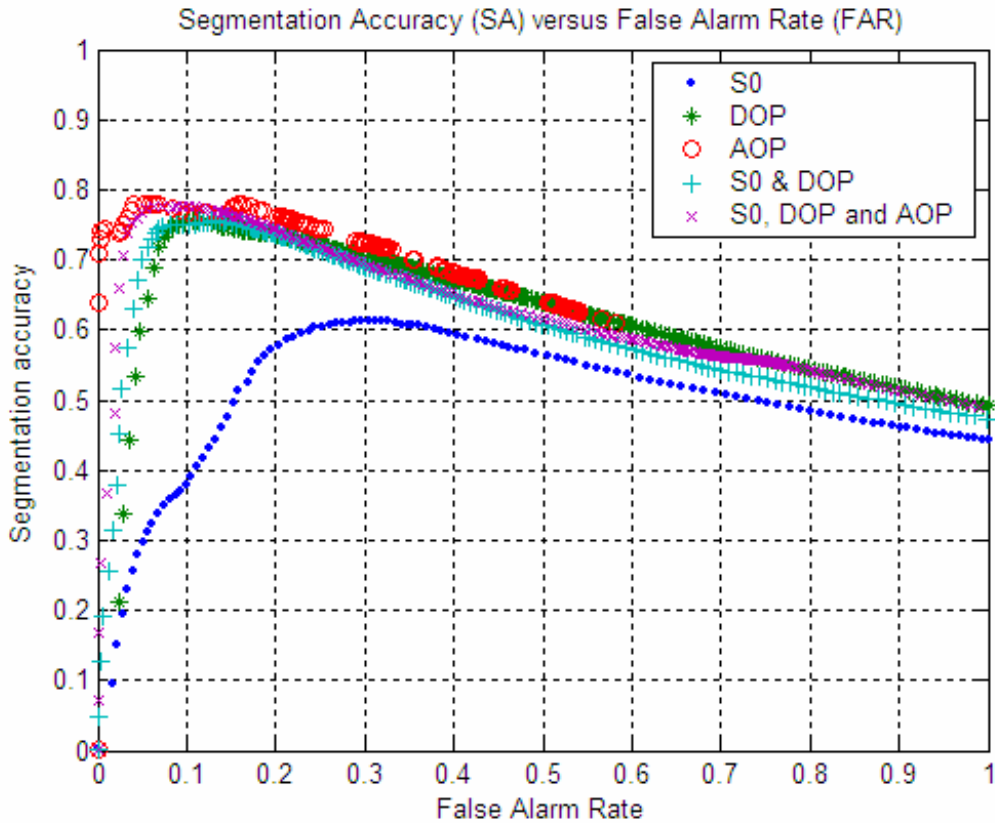
Figure 5.10:   Receiver Operating Characteristic curves produced by different fusion schemes for the case where the target plate was at 70° viewing angle

Figure 5.11 shows the segmentation results for the different fusion schemes with threshold values chosen based on a CFAR of 20%. The top left image is the reference target area (G). The polarized data and fused data yielded a good segmented image. The tilted target plate was clearly segmented from the background and the side plate was suppressed. The good segmentation results produced by the DOP and AOP data were due to the high degree of polarization and distinct angle of polarization of the emission from the target plate at 70° viewing angle. The side plate at 20° viewing angle was not polarized. The image produced by the intensity-only data contained missing parts on the target plate and false detections on the side plate.

Figure 5.11:   Segmented target regions produced by different fusion schemes for the case where the target plate was at 70° viewing angle

Table 5.5 shows the threshold values used, SA, and FAR, produced by each fusion scheme for CFAR of 20%. The fused data SA was 74%, compared to 57% for the intensity-only data. The enhancement in segmentation accuracy was 17%.

CFAR=20%			
Fusion schemes	Threshold values	SA (%)	FAR (%)
S_0-only	0.0362	57.3	19.5
DOP-only	0.1	73.7	19.8
AOP-only	0.0155	77.0	18.6
S_0 and DOP	0.1051	73.7	19.6
S_0, DOP and AOP	0.1008	74.4	19.8

Table 5.6:   The threshold value used and resulting segmentation accuracy and false alarm rate for the case where the target plate was at 70° viewing angle

6.   Target Plate at 80° Viewing Angle

Figure 5.12 shows the ROC curves produced by the different fusion schemes at 80° viewing angle. The AOP-only data gave the highest peak SA of about 75% at FAR of 12%. The slight discontinuity in the AOP curve, around FAR of 10%, may be due to the small sample size (small target plate area in the image) and sharp gradient in the AOP histogram. The fusion of S_0, DOP and AOP produced a peak SA of 70% and corresponding FAR of 10%. The intensity-only data produced the worst result among the schemes, with peak SA of only 35% for all FAR value greater than 40%.
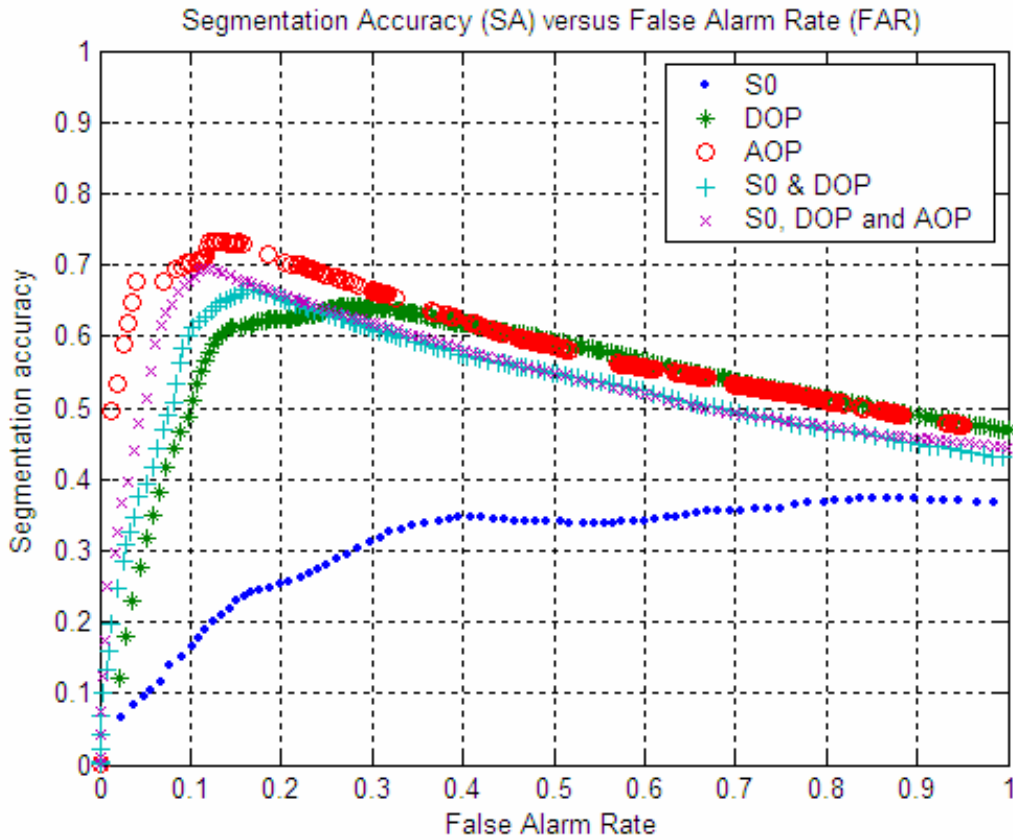
Figure 5.12:   Receiver Operating Characteristic curves produced by different fusion schemes for the case where the target plate was at 80° viewing angle

Figure 5.13 shows the segmentation results for the different fusion schemes with threshold values chosen based on a CFAR of 20%. The top left image is the reference target area (G). The polarized data and fused data yielded good segmented image. The tilted target plate was clearly segmented from the background and the side plate was suppressed. The good segmentation results produced by the DOP and AOP data were due to high degree of polarization and distinct angle of polarization of emission from the target plate at 80° viewing angle. The emission from the side plate (10° viewing angle) was not polarized. The intensity-only data failed to detect both the target and side plates.
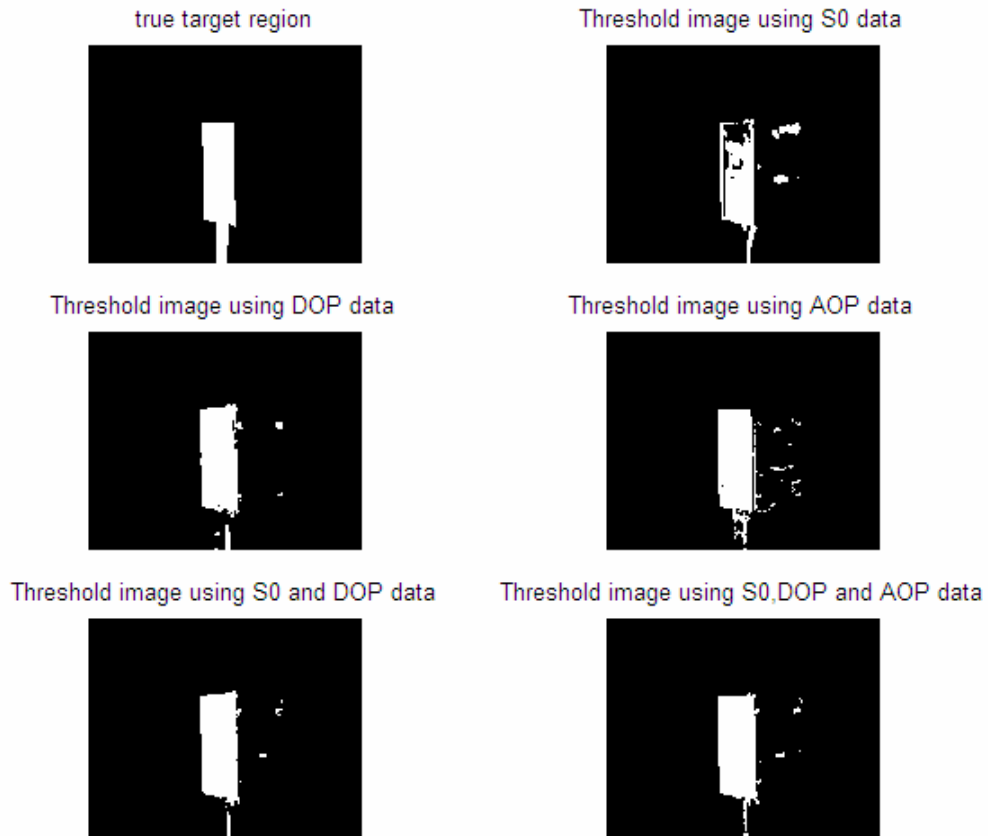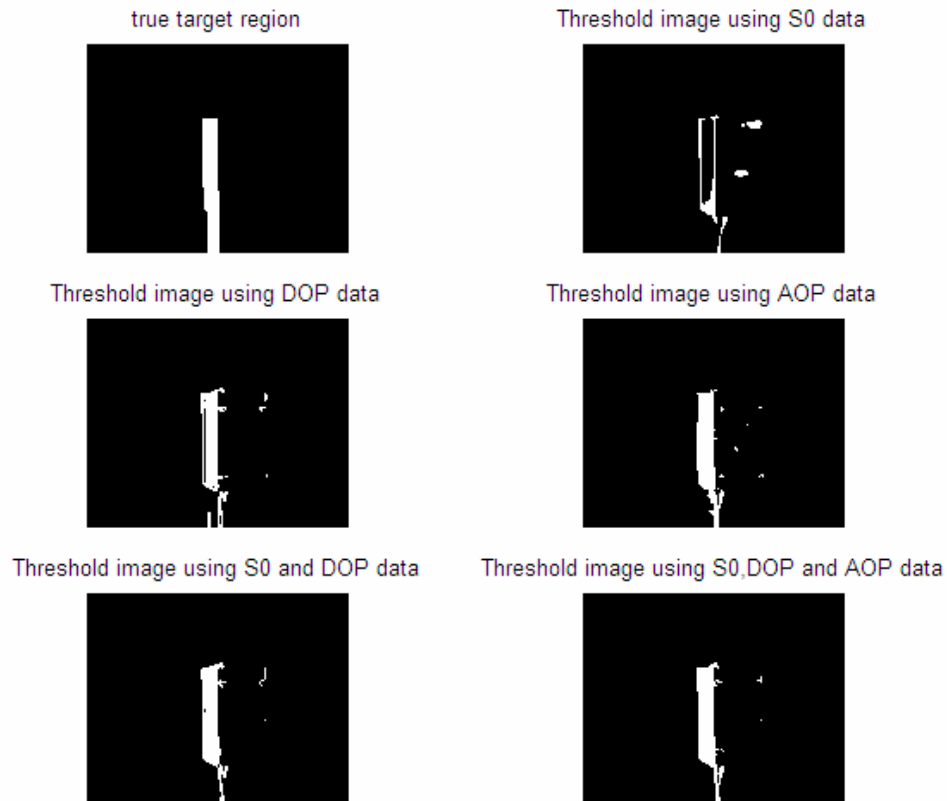

Figure 5.13:　Segmented target regions produced by different fusion schemes for the case where the target plate was at 80° viewing angle

82

Table 5.7 shows the threshold values used, SA, and FAR, produced by each fusion scheme, with a CFAR of 20%. The fused data's SA was 66%, compared to 25% for the intensity-only data. The enhancement in segmentation accuracy was 41%.

CFAR=20%			
Fusion schemes	Threshold values	SA (%)	FAR (%)
S_0-only	0.0211	25.2	19.9
DOP-only	0.0756	62.5	20.0
AOP-only	0.0147	71.5	18.5
S_0 and DOP	0.0891	65.3	20.0
S_0, DOP and AOP	0.0825	66.0	20.0

Table 5.7: The threshold value used and resulting segmentation accuracy and false alarm rate for the case where the target plate was at 80° viewing angle

From the above results, we conclude that intensity data produced good segmentation of the target plate at 0° to 40° viewing angle. For angles greater than 60°, both degree of polarization and polarization angle data yielded better results than the intensity data. As a result, the fusion of all three data provides better segmentation compared to intensity-only data. The enhancement in segmentation accuracy over the intensity data improved from 3% to 41%, when the viewing angle was increased from 60° to 80°.

THIS PAGE INTENTIONALLY LEFT BLANK

VI.   CONCLUSIONS AND RECOMMENDATIONS

A.   CONCLUSIONS

A polarimetric thermal imager, operating in the mid wave infrared (3-5 μm), was set up using the Merlin InSb camera with three internal wire grid polarizers. The polarizer transmission axes were aligned at 0°, 45° and 90° to the detector horizontal plane. Two point non-uniformity correction was performed to compensate for non uniformity in detector response and to replace bad pixels. Radiometric calibration was applied to compensate for spatial and transmittance differences in the polarized channels. The scene consisted of a heated aluminum plate in front of a large area blackbody as background. The viewing angle, defined as the angle between surface normal and camera line of sight, was varied by rotating the plate about its vertical axis.

The signal intensity transfer function showed that the measured digital levels were linearly related to the irradiance values, within the temperature range of interest. Using the linear relationship, the measured digital images were converted to irradiance maps. The polarizers have very similar transmission characteristics. The average in-band (3-5 μm) transmittance was calculated as the ratio of the irradiance measured with and without polarizer and was found to be 30%.

Stokes parameters were computed from the irradiance images collected at different polarization angles. The intensity, degree of polarization and angle of polarization images were derived from the Stokes parameters. Emission from the target plate at normal viewing angle was not polarized. Target plate at 70° viewing angle produced emission with 8.5% degree of polarization and polarization angle of 150°.

When the viewing angle of the target plate was increased from 0° to 80°, the intensity increased slightly due to higher emissivity of metal at wide emission angles. Degree of polarization at viewing angle less than 20° was less than 1%. DOP increased rapidly from 1% to 8.5%, when the viewing angle was increased from 20° to 80°. The angle of polarization (AOP) increased with viewing angle, and became constant at 150° for viewing angle greater than 60°. The calibrated curve relating the degree of

polarization to viewing angle provides useful information for discriminating target surface orientation. Target and background contrast based on intensity increased slightly from 5 to 10% with viewing angle. The contrast based on DOP increased with viewing angle from 0% at 20° to a maximum value of 90% at 70°. The higher target-background contrast provided by DOP at angle greater than 20° can potentially improve the probability of detection and reduce false alarms in the target detection process.

Image processing algorithms for segmenting the target plate from background were developed in Matlab. The statistical similarity metric, Fisher distance, was computed for different fusion schemes; namely; a) intensity-only, b) degree of polarization-only (DOP), c) polarization angle-only (AOP), d) intensity and DOP and e) intensity, DOP and AOP. Their performance was quantified using the Receiver Operating Characteristic curves, which plot segmentation accuracy against false alarm rate. A Constant False Alarm Rate (CFAR) threshold was applied to each fusion scheme to obtain the segmented binary images.

The intensity-only data produced good segmentation of the plate at 0° to 40° viewing angles. For angles greater than 60°, both degree of polarization and polarization angle data yielded better results than the intensity-data. As a result, the fusion of all three data provides better segmentation compared to intensity-only data. The enhancement in segmentation accuracy over the intensity data, improved from 3% to 41%, as the viewing angle was increased from 60 to 80°.

This project confirmed the thermal emission from a metal plate at oblique viewing angle is partially polarized, with higher component in the horizontal plane of emission. The degree of polarization increases with viewing angle. The relationship between the degree of polarization and viewing angle can be used to determine the orientation of target surfaces and hence aid in target recognition. The high contrast offered by the polarization signature can enhance the detection of small targets in highly cluttered background. Polarization characteristics can also be used to discriminate man-made objects, such as tanks and trucks, from randomly polarized backgrounds such as foliage. Fusion of polarization and intensity data provides a more robust target segmentation process, capable of high segmentation accuracy and low false alarm rate.

B. RECOMMENDATIONS

The energy collected by a thermal camera from a scene comprises both reflected and emitted radiation. Both components are partially polarized. For infrared wavelengths, where cold sky is the main contributor to the reflective component, surface emission tends to dominate the signature and the state of polarization. Thus, the focus of this research is on polarization of thermal emission and its application for target detection. Reflection components were not included in the experiment.

However, it is of interest to investigate how reflected radiation will affect the final polarization states of radiation received by the sensor. For this experiment, both the camera and target plate should be moved from the laboratory to the rooftop of Spanagel Hall. The camera should be mounted on a pan and tilt unit to facilitate pointing at the target plate, with sky as the background. The same data collection process should be repeated for the plate at different viewing angles. The data should be processed to derive the Stokes parameters, degree of polarization and polarization angles. Image processing techniques should be developed to segment the target plate from the sky background. The performance of intensity-only, polarization data only or a fusion of both, should be compared using the Receiver Operating Characteristic curves.

THIS PAGE INTENTIONALLY LEFT BLANK

APPENDIX A

Specifications of Merlin InSb laboratory camera
(http://www.indigosystems.com/product/merlin_specs.html dated 11 Oct 2004)

The following specification for the Merlin InSb Laboratory Camera was downloaded from the homepage of the Indigo Systems Corporation

Merlin MWIR	
Detector Type	InSb
Spectral Range	1 - 5.4 µm (3 - 5 µm set by cold filter)
Detector Size	30 x 30 µm
Array Format	320 x 256
Integration Time	5 µs - 16.5 ms
Camera f/#	2.3
Cooling Type	Liquid Nitrogen
NEdT [NEI]	< 25 mK (< 18 mK typical)
Analog Video	NTSC @ 30 Hz (PAL @ 25 Hz optional); S-Video
Digital Video	60, 30*, 15* Hz (50 Hz PAL), 12-bit corrected/uncorrected (*Reduced frame rate option disables analog video. This option not available for Merlin Uncooled.)
Remote Control	Button Panel & RS-232
Size	5.5 "H x 5.0 "W x 9.8 "L
Weight	9 lbs
Standard Temp Measurement	0 - 350 $^{\circ}$C
Extended Temp Measurement	300 - 2,000 $^{\circ}$C
Temp Accuracy	2 $^{\circ}$C or 2%

THIS PAGE INTENTIONALLY LEFT BLANK

APPENDIX B

Specification of SPECAC wire grid polarizer

The transmission plots are shown in Figure B-1.

E_h: Optical power transmitted by the polarizer with its grid line horizontal

E_v: Optical power transmitted by the polarizer with its grid line vertical

E_x: Optical power transmitted by a pair of polarizers with grids crossed

E_0: Optical power received without polarizer

The transmission coefficient (K_1):

$$K_1 = \frac{E_h + E_v}{E_0}$$

The % transmission of unwanted radation (K2)

$$K_2 = \frac{E_x}{E_h + E_v}$$

From transmission plot in Figure B-1, at wavelength λ=5um,

$$K_1 = 0.47 + 0.43 = 0.9$$

$$K_2 = 0.4$$

The degree of polarization (DOP) and extinction ratio (μ) were computed as:

$$DOP = \frac{K_1 - K_2}{K_1 + K_2}$$

$$\mu = \frac{K_1}{K_2}$$
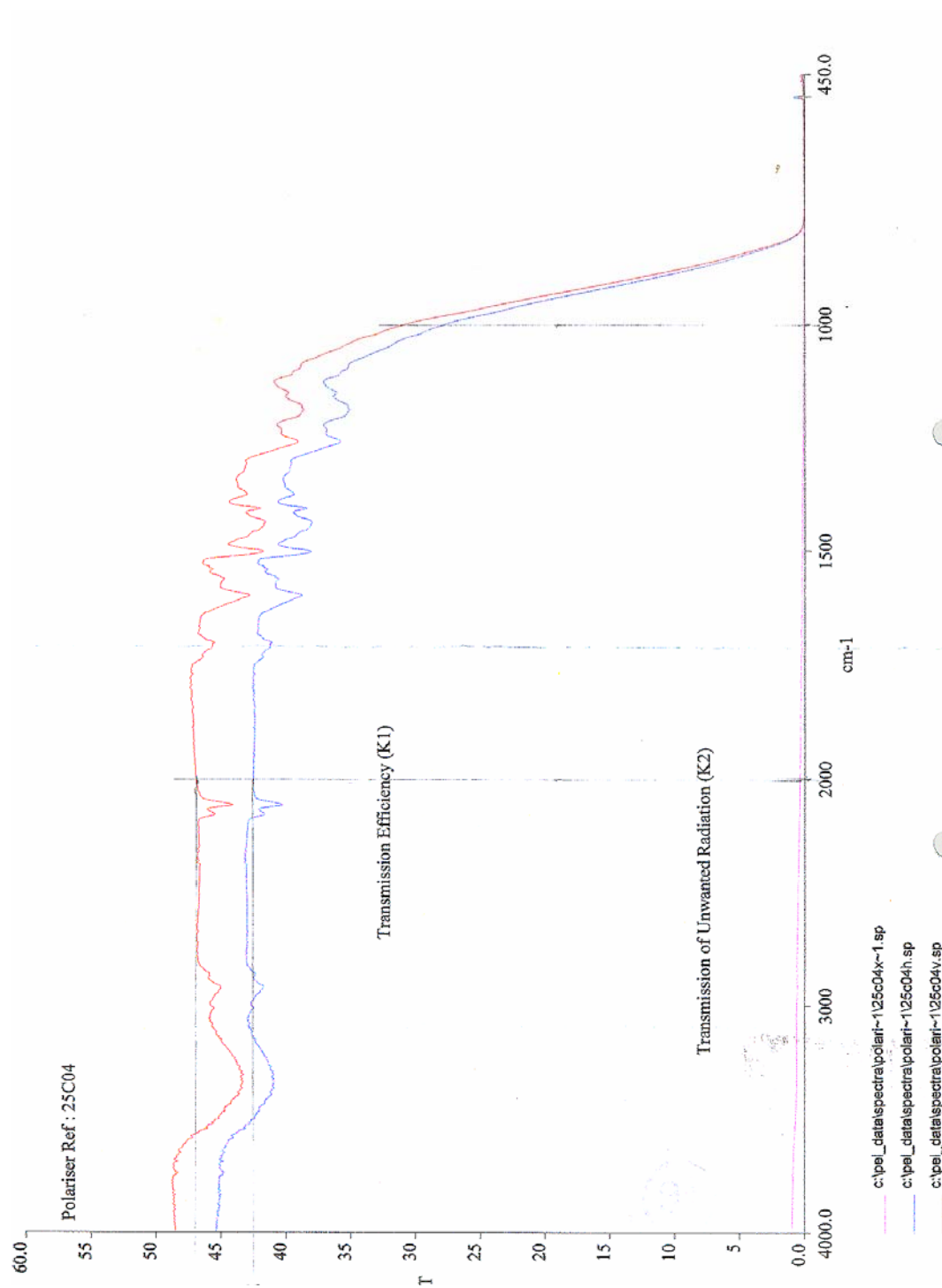
Figure B-1:   Transmission plot of polarizer (provided by SPECAC)

APPENDIX C

Image processing Matlab program listing

```
%texture based segmentation with ROC plots
addpath('c:\fookleong\thesis\dec13\tgt50_bb35')
addpath('c:\fookleong\thesis\dec13\bb25')
addpath('c:\fookleong\thesis\dec13\bb40')

clear; clear all;
load D13_tgt50_bb35_stat;
load AOPthr;
load D13_truereg_bb35_A80;
Me25C=5.4484E-4;% W/cm2
Me40C=9.2225E-4;% W/cm2

A=double(imread('tgt80_pol0','tiff'));
B=double(imread('tgt80_pol45','tiff'));
C=double(imread('tgt80_pol90','tiff'));
[irow icol]=size(A);

Abb25=double(imread('pol0_bb25','tiff'));
Bbb25=double(imread('pol45_bb25','tiff'));
Cbb25=double(imread('pol90_bb25','tiff'));

Abb40=double(imread('pol0_bb40','tiff'));
Bbb40=double(imread('pol45_bb40','tiff'));
Cbb40=double(imread('pol90_bb40','tiff'));

L0=Me25C+((Me40C-Me25C)*((A-Abb25)./(Abb40-Abb25)));
L45=Me25C+((Me40C-Me25C)*((B-Bbb25)./(Bbb40-Bbb25)));
L90=Me25C+((Me40C-Me25C)*((C-Cbb25)./(Cbb40-Cbb25)));

wsize=3;
L0m = colfilt(L0,[wsize wsize],'sliding',@mean);
L45m = colfilt(L45,[wsize wsize],'sliding',@mean);
L90m = colfilt(L90,[wsize wsize],'sliding',@mean);
low=(wsize+1)/2;hrow=irow-low+1;hcol=icol-low+1;
L0(low:hrow,low:hcol)=L0m(low:hrow,low:hcol);
L45(low:hrow,low:hcol)=L45m(low:hrow,low:hcol);
L90(low:hrow,low:hcol)=L90m(low:hrow,low:hcol);

S0=L0+L90;
S1=L0-L90;
S2=2*L45-S0;
DP0=S1./S0;
DP45=S2./S0;
P=sqrt(S1.^2+S2.^2)./S0;

for i=1:256
    for j=1:320
```

```matlab
        %both 0 and 45 pol are small=> unpolarised
        if (abs(DP0(i,j))<=AOPthr) && (abs(DP45(i,j))<=AOPthr)
            phi(i,j)=0;
        %S1 small, but S2 can be positive or negative
        elseif abs(DP0(i,j))<=AOPthr
            if S2(i,j)>0
                phi(i,j)=45;
            else
                phi(i,j)=135;
            end
        %S2 small, but S1 can be positive or negative
        elseif abs(DP45(i,j))<=AOPthr
            if S1(i,j)>0
                phi(i,j)=0;
            else
                phi(i,j)=90;
            end
        %S1 and S2 are small
        %if (S1(i,j)==0)|(S2(i,j)==0)
        %    phi(i,j)=0;
        elseif (S1(i,j)<0 && S2(i,j)>0)
            phi(i,j)=(180-abs(atan(S2(i,j)/S1(i,j)))*(180/pi))/2;
        elseif (S1(i,j)<0 && S2(i,j)<0)
            phi(i,j)=(180+abs(atan(S2(i,j)/S1(i,j)))*(180/pi))/2;
        elseif (S1(i,j)>0 && S2(i,j)<0)
            phi(i,j)=(360-abs(atan(S2(i,j)/S1(i,j))*(180/pi)))/2;
        else
            phi(i,j)=abs(atan(S2(i,j)/S1(i,j)))*(180/pi)/2;
        end
    end
end

%intensity
Imeanmap=S0;
map = colfilt(S0,[wsize wsize],'sliding',@mean);
Imeanmap(low:hrow,low:hcol)=map(low:hrow,low:hcol);

Ivarmap=colfilt(S0,[wsize wsize],'sliding',@var);
Ivarmap(low:hrow,1)=Ivarmap(low:hrow,2);
Ivarmap(low:hrow,icol)=Ivarmap(low:hrow,icol-1);
Ivarmap(1,:)=Ivarmap(2,:);
Ivarmap(irow,:)=Ivarmap(irow-1,:);

%DOP
Pmeanmap=P;
map = colfilt(P,[wsize wsize],'sliding',@mean);
Pmeanmap(low:hrow,low:hcol)=map(low:hrow,low:hcol);

Pvarmap=colfilt(P,[wsize wsize],'sliding',@var);
Pvarmap(low:hrow,1)=Pvarmap(low:hrow,2);
Pvarmap(low:hrow,icol)=Pvarmap(low:hrow,icol-1);
Pvarmap(1,:)=Pvarmap(2,:);
Pvarmap(irow,:)=Pvarmap(irow-1,:);

%phi
```

```
phimeanmap=phi;
map = colfilt(phi,[wsize wsize],'sliding',@mean);
phimeanmap(low:hrow,low:hcol)=map(low:hrow,low:hcol);

phivarmap=colfilt(phi,[wsize wsize],'sliding',@var);
phivarmap(low:hrow,1)=phivarmap(low:hrow,2);
phivarmap(low:hrow,icol)=phivarmap(low:hrow,icol-1);
phivarmap(1,:)=phivarmap(2,:);
phivarmap(irow,:)=phivarmap(irow-1,:);

histstep=450;
%take average of target statistics
imean=mean(S0tm(1:6));
ivar=sum(S0tstd(1:6).^2)/6;
Fisher1=((Imeanmap-imean).^2)./(Ivarmap+ivar);

Pmean=mean(DOLPtm(4:6));
Pvar=sum(DOLPtstd(4:6).^2)/3;
Fisher2=((Pmeanmap-Pmean).^2)./(Pvarmap+Pvar);

Amean=mean(AOPtm(4:6));
Avar=sum(AOPtstd(4:6).^2)/3;
Fisher3=((phimeanmap-Amean).^2)./(phivarmap+Avar);

range1=max(max(Fisher1))-min(min(Fisher1));
range2=max(max(Fisher2))-min(min(Fisher2));
range3=max(max(Fisher3))-min(min(Fisher3));

iw=1;
pw=0;
phiw=0;
Fishera=iw*((Fisher1-min(min(Fisher1)))/range1)+pw*((Fisher2-
min(min(Fisher2)))/range2)+phiw*((Fisher3-min(min(Fisher3)))/range3);

Fmin=min(min(Fishera));
Fmax=max(max(Fishera))/2;
Fint=(Fmax-Fmin)/histstep;
inthistx=Fmin:Fint:Fmax;
histy=reshape(Fishera,1,256*320);
[N,X]=hist(histy,inthistx);
figure(1);
subplot(3,2,1);plot(X,N)
xlabel('normalized Fisher parameter');
ylabel('no. of pixel');
legend('SO data');
grid on;

iw=0;
pw=1;
phiw=0;
Fisherb=iw*((Fisher1-min(min(Fisher1)))/range1)+pw*((Fisher2-
min(min(Fisher2)))/range2)+phiw*((Fisher3-min(min(Fisher3)))/range3);

Fmin=min(min(Fisherb));
Fmax=max(max(Fisherb));
```

```
Fint=(Fmax-Fmin)/histstep;
Phistx=Fmin:Fint:Fmax;
histy=reshape(Fisherb,1,256*320);
[N,X]=hist(histy,Phistx);
figure(1);subplot(3,2,2);plot(X,N);
xlabel('normalized Fisher parameter');
ylabel('no. of pixel');
legend('DOP data');
grid on;

iw=0;
pw=0;
phiw=1;
Fisherc=iw*((Fisher1-min(min(Fisher1)))/range1)+pw*((Fisher2-
min(min(Fisher2)))/range2)+phiw*((Fisher3-min(min(Fisher3)))/range3);

Fmin=min(min(Fisherc));
Fmax=max(max(Fisherc))/5;
Fint=(Fmax-Fmin)/histstep;
phihistx=Fmin:Fint:Fmax;
histy=reshape(Fisherc,1,256*320);
[N,X]=hist(histy,phihistx);
figure(1);subplot(3,2,3);plot(X,N);
xlabel('normalized Fisher parameter');
ylabel('no. of pixel');
legend('AOP data');
grid on;

iw=0.5;
pw=0.5;
phiw=0;
Fisherd=iw*((Fisher1-min(min(Fisher1)))/range1)+pw*((Fisher2-
min(min(Fisher2)))/range2)+phiw*((Fisher3-min(min(Fisher3)))/range3);

Fmin=min(min(Fisherd));
Fmax=max(max(Fisherd));
Fint=(Fmax-Fmin)/histstep;
F2histx=Fmin:Fint:Fmax;
histy=reshape(Fisherd,1,256*320);
[N,X]=hist(histy,F2histx);
figure(1);subplot(3,2,4);plot(X,N);
xlabel('normalized Fisher parameter');
ylabel('no. of pixel');
legend('SO & DOP data');
grid on;

iw=0.33;
pw=0.33;
phiw=0.33;
Fishere=iw*((Fisher1-min(min(Fisher1)))/range1)+pw*((Fisher2-
min(min(Fisher2)))/range2)+phiw*((Fisher3-min(min(Fisher3)))/range3);

Fmin=min(min(Fishere));
Fmax=max(max(Fishere));
Fint=(Fmax-Fmin)/histstep;
```

```
F3histx=Fmin:Fint:Fmax;
histy=reshape(Fishere,1,256*320);
[N,X]=hist(histy,F3histx);
figure(1);subplot(3,2,5);plot(X,N);
xlabel('normalized Fisher parameter');
ylabel('no. of pixel');
legend('SO, DOP and AOP data');
grid on;

[I,J]=find(pregmap);
notrue=length(I);

stepno=length(inthistx);
for cnt=1:stepno
    %intensity ROC
    intbmap=Fishera<=inthistx(cnt);
    overlap=intbmap & pregmap;
    [I,J]=find(overlap);
    nocorrect=length(I);

    false=intbmap-overlap;
    [I,J]=find(false);
    nofalse=length(I);

    union=intbmap|pregmap;
    [I,J]=find(union);
    nounion=length(I);

    IFAR(cnt)=nofalse/notrue;
    ISA(cnt)=nocorrect/nounion;

    %DOP ROC
    Pbmap=Fisherb<=Phistx(cnt);
    overlap=Pbmap & pregmap;
    [I,J]=find(overlap);
    nocorrect=length(I);

    false=Pbmap-overlap;
    [I,J]=find(false);
    nofalse=length(I);

    union=Pbmap|pregmap;
    [I,J]=find(union);
    nounion=length(I);

    PFAR(cnt)=nofalse/notrue;
    PSA(cnt)=nocorrect/nounion;

    %AOP ROC
    phibmap=Fisherc<=phihistx(cnt);
    overlap=phibmap&pregmap;
    [I,J]=find(overlap);
    nocorrect=length(I);

    false=phibmap-overlap;
```

```
[I,J]=find(false);
nofalse=length(I);

union=phibmap|pregmap;
[I,J]=find(union);
nounion=length(I);

phiFAR(cnt)=nofalse/notrue;
phiSA(cnt)=nocorrect/nounion;

%fused int and P
F2bmap=Fisherd<=F2histx(cnt);
overlap=F2bmap&pregmap;
[I,J]=find(overlap);
nocorrect=length(I);

false=F2bmap-overlap;
[I,J]=find(false);
nofalse=length(I);

union=F2bmap|pregmap;
[I,J]=find(union);
nounion=length(I);

F2FAR(cnt)=nofalse/notrue;
F2SA(cnt)=nocorrect/nounion;

%fused int and P and phi
F3bmap=Fishere<=F3histx(cnt);

overlap=F3bmap&pregmap;
[I,J]=find(overlap);
nocorrect=length(I);

false=F3bmap-overlap;
[I,J]=find(false);
nofalse=length(I);

union=F3bmap|pregmap;
[I,J]=find(union);
nounion=length(I);

F3FAR(cnt)=nofalse/notrue;
F3SA(cnt)=nocorrect/nounion;

%figure(1);subplot(3,2,1);imshow(pregmap);
%subplot(3,2,2);imshow(intbmap);
%subplot(3,2,3);imshow(Pbmap);
%subplot(3,2,4);imshow(phibmap);
%subplot(3,2,5);imshow(F2bmap);
%subplot(3,2,6);imshow(F3bmap);

if (IFAR(cnt)>1)&(PFAR(cnt)>1)&(phiFAR(cnt)>1)&(F2FAR(cnt)>1)&(F3FAR(cnt)>1)
break;
end
```

```
end%

figure(2);plot(IFAR,ISA,'.',PFAR,PSA,'*',phiFAR,phiSA,'o',F2FAR,F2SA,'+',F3FAR,F3SA,'x');
axis([0 1 0 1]);
title('Segmentation Accuracy (SA) versus False Alarm Rate (FAR)');
xlabel('False Alarm Rate');
ylabel('Segmentation accuracy');
legend('S0','DOP','AOP','S0 & DOP','S0, DOP and AOP');
grid on;

%constant false alarm CFAR threshold
constantFAR=0.2;
%intensity threshold
thri=max(find(IFAR<=constantFAR));
Ithrdata=[inthistx(thri) ISA(thri) IFAR(thri)]

%P threshold image
thri=max(find(PFAR<=constantFAR));
Pthrdata=[Phistx(thri) PSA(thri) PFAR(thri)]

%phi threshold image
thri=max(find(phiFAR<=constantFAR));
phithrdata=[phihistx(thri) phiSA(thri) phiFAR(thri)]

%F2 threshold
thri=max(find(F2FAR<=constantFAR));
F2thrdata=[F2histx(thri) F2SA(thri) F2FAR(thri)]

%F3 threshold
thri=max(find(F3FAR<=constantFAR));
F3thrdata=[F3histx(thri) F3SA(thri) F3FAR(thri)]

figure(3);
subplot(3,2,1);imshow(pregmap);
title('true target region');
subplot(3,2,2);imshow(Fishera<Ithrdata(1,1));
title('Threshold image using S0 data');
subplot(3,2,3);imshow(Fisherb<Pthrdata(1,1));
title('Threshold image using DOP data');
subplot(3,2,4);imshow(Fisherc<phithrdata(1,1));
title('Threshold image using AOP data');
subplot(3,2,5);imshow(Fisherd<F2thrdata(1,1));
title('Threshold image using S0 and DOP data');
subplot(3,2,6);imshow(Fishere<F3thrdata(1,1));
title('Threshold image using S0,DOP and AOP data');
```

THIS PAGE INTENTIONALLY LEFT BLANK

LIST OF REFERENCES

1.   Lloyd, J. M., *Thermal Imaging Systems,* Plenum Press, New York, 3rd printing, 1982.

2.   Collett, E., *Polarized Light Fundamentals and Applications*, Marcel Dekker Inc., New York, 1993

3.   Guenther, R.D., *Modern Optics*, John Wiley & Sons, New York, 1990.

4.   Born, M., Wolf, E., *Principles of optics*, Cambridge University Press, 7th edition, 2002.

5.   Ordal, M. H. et. al., "Optical properties of the metals Al, Co, Cu, Au, Pt, As, Ti and W in the infrared and far infrared", *Applied Optics*, Vol. 22, No. 7, April 1983.

6.   Arago, F., *Ann. Chem et. Phys.*, 2(27):89, 1824

7.   Millikan, R. A., *Physic Rev.*, 3(81):177, 1895

8.   Sandus, O., "A review of emission polarization", *Applied Optics*, Vol. 4, No. 12, Dec. 1965.

9.   Siegel, R., Howell, J.R., *Thermal Radiation Heat Transfer*, 2nd edition, Hemisphere Publishing Corp., 1981.

10.   Wolff, L.B., Lundberg, A., Tang, R.J., "Thermal emission polarization", *SPIE Proceedings*, Vol. 3754, 1999.

11.   Solomon, J.E., "Polarization imaging", *Applied Optics*, Vol. 20, No. 9, May 1981.

12.   Howe, J.D., "Two-color infrared full-Stokes imaging polarimeter development", *IEEE Aerospace conference proceeding*, Vol. 4, Mar. 1999.

13.   Chun, S. L., Fleming, D. L., Harvey, W. A., Torok, E. J., "Polarization sensitive infrared sensor for target discrimination", *SPIE Proceeding*, Vol. 3121, 1997.

14. Rogne, T.J., Smith, F.G., Rice, J.E., "Passive target detection using polarized components of infrared signatures", *SPIE Proceedings*, Vol. 1317, 1990.

15. Cooper, A.W., Crittenden, E.C., "Mid and far infrared measurements of sun glint from the sea surface", *Optics of the Air-Sea Interface: Theory and Measurement, SPIE Proceeding*, Vol. 1749, 1992.

16. Rogne, T.J., Gliechman, K.W., Maxwell, J.R., "Mid-Wave infrared imaging polarimeter: instrument development and background measurements", Environmental Research Institute of Michigan, Report No. 253870-2-F, Ann Arbor, Michigan, 1995.

17. Matthew, P.F., "Spectral polarization signatures of materials in the LWIR", *SPIE Proceedings*, Vol. 4133, 2000.

18. Howe, J.D., Miller, M.A., Blumer, R.V., "Polarization sensing for target acquisition and mine detection", *SPIE Proceedings*, Vol. 4133, 2000.

19. Sadjadi, F.A. , Chun, S. L., "New experiments in the use of infrared polarization in the detection of small target", *SPIE Proceeding*, Vol. 4379, 2001.

20. Sadjadi, F.A., Chun, S. L., "Passive polarimetric IR target classification", *IEEE Transaction on Aerospace and Electronics Systems*, Vol. 37, No. 2, April 2001.

21. Merlin InSb Laboratory Camera User's Guide, version 120, 414-0010-10, Indigo Systems Corporation.

22. IRVista 2.5.1 User's Manual, 321-0028-10, Indigo Systems Corporation.

23. Cremer, F., Jong W.D., Schutte K., "Infrared polarization measurements and modeling applied to surface laid anti-personnel landmines", *Optical Engineering*, Vol. 41, No. 5, May 2002.

INITIAL DISTRIBUTION LIST

1.   Defense Technical Information Center
     Ft. Belvoir, Virginia

2.   Dudley Knox Library
     Naval Postgraduate School
     Monterey, California

3.   Professor Dan C. Boger, Code SM/Bo
     Department of Information Systems
     Naval Postgraduate School
     Monterey, California

4.   Professor Alfred W. Cooper, Code PH/Cr
     Department of Physics
     Naval Postgraduate School
     Monterey, California

5.   Professor Gamani Karunasiri, Code PH/Kg
     Department of Physics
     Naval Postgraduate School
     Monterey, California

6.   Mr. Ho Wei Ling
     Electronics Research Laboratory
     DSO National Laboratories
     Republic of Singapore

7.   Mr. Loo Fook Leong
     Electronics Research Laboratory
     DSO National Laboratories
     Republic of Singapore